2005

STM and Computational Investigations of Nanostructured Layered Transition Metal Chalcogenides

Changki Kim
Seton Hall University

STM and Computational Investigations of Nanostructured Layered Transition Metal Chalcogenides

Dissertation presented
by

Changki Kim

to

The Department of Chemistry and Biochemistry
in partial fulfillment of the requirements
for the degree of
Doctor of Philosophy

Seton Hall University
South Orange, New Jersey
May, 2005

We certify that we have read this thesis and that in our opinion it is adequate in scientific scope and qualify as a dissertation for the degree on Doctor of Philosophy.

Approved

Dr. Stephen P. Kelty
In charge of Major Work

Dr. Alex Fadeev
Member of Dissertation Committee

Dr. Wyatt R. Murphy, Jr.
Member of Dissertation Committee

Dr. Nicholas H. Snow
Approved for the Department of Chemistry and Biochemistry
Chemistry and Biochemistry Chairman

Abstract

Presented in this thesis are the results of an extensive investigation of the catalytically active sites of layered transition metal chalcogenide (LTMC) nanoclusters which are generally used as hydrodesulfurization (HDS) catalysts. It is well known that the active sites in these materials are localized at the layer edge, encompassing both the structural geometry and electronic properties of the edge sites. The edge localized atomistic properties of LTMCs were investigated by performing experimental scanning tunneling microscopy (STM) and interpreting these results using Density Functional (DF) and Extended Hückel Tight Binding (EHTB) calculations.

STM studies of nanoparticles of semiconducting MoS_2, ReS_2, WS_2, and metallic $NbSe_2$ were preformed in order to probe the local details of the edge electronic structure. STM results indicate that three low Miller index edge terminations exist in trigonal prismatic LTMCs, namely $[11\bar{2}0]$, $[10\bar{1}0]$, and $[11\bar{2}0]$. Each of these edge terminations exhibited some variation local electronic structures.

STM data provides a topography map of the local electronic state density which is a convolution of the geometry and local density of states. In order to properly interpret the STM data, computational tools must be used to discern to effects of geometry and local density of states. These computational studies included calculating the band structure and optimizing the geometry of ribbon models of the studied materials. From the optimized structures, simulated STM images were produced and compared with experimental data. From a comparison of the simulated STM images of the proposed models with the Experimental data, it was found that the possible layer edge termination

structure was limited.

From these studies, it is possible to further expand on the details of adsorption or sulfur containing substrates on the layer edge. As part of this project, the outcomes of the geometric and electronic structure were used to investigate the possible mechanisms of adsorption on the layer edge that would lead to carbon-sulfur bond dissociation. The probe substrate used in computer simulations of absorption was thiophene. It was found that adsorption of thiophene on the proposed layer edges did destabilize the thiophene ring and weaken the carbon-sulfur bond.

The outcomes of the project offer a more fundamental understanding of the properties of LTMCs, particularly the active site on the layer edge. Further studies based on these findings will help elucidate the mechanism of HDS on LTMCs and promote development of more advanced HDS catalysts.

Acknowledgement

My research has been taken terribly longer than six and half years to complete with the help and support, so I take delight in the appreciation for people whom have helped me.

First, I would like to thank my advisor, Dr. Steve Kelty for his constructive suggestions and plentiful discussion as well as flexible and deliberate guidance and scientific insight. Moreover, I appreciate his hard work on revising my manuscript.

I thank Dr. Hansnip, for his generous discussion of Density Functional Theory (DFT). When I had a hard time understanding the computational work and its theory, he taught me from general to deep insights. I also thank Dr. Ren who built the EHTB packages and for providing an updated package for free.

I thank my father, brother, sister, sister in law, and relatives for their love and encouragement, without whom I am unlikely to have become a scientist and would never have enjoyed so many opportunities. Finally, I have to thank my wife, Youngmi for her extremely strong help keeping me happy and endurance.

Dedication

To my family and wife
For much understanding

List of Figures

List of Tables

Table of Contents

I. Introduction

1. Layered Transition Metal Chalcogenides (LTMCs) in technology

Layered Transition Metal Chalcogenides (LTMCs) are well known catalysts in the petroleum and chemical industries.[1,2] Transition metal chalcogenides (TMC) including the cubic pyrite type have unique active phases that are sulfur-tolerant during hydrogenation and hydrodesulfurization (HDS).[3,4] The catalytic activity of TMCs varies by several orders of magnitude over the d-electron block in the periodic table. The most economically feasible sulfur-tolerant catalysts are based on LTMCs promoted with Ni and Co and supported on alumina, silica or TiO_2. While the highest catalytic activity is found in RuS_2 and OsS_2, [1,5,6] the extreme high cost of RuS_2 prohibits its use as cost-effective catalysts and less costly MoS_2 including current prices of RuS_2 or OsS_2 vs. MoS_2, ReS_2 is currently used for hydrotreating.

A fundamental understanding of the active phase of the catalyst leading to enhanced performance is of crucial importance in the optimization of the catalyst. It is also of fundamental interest to determine the nature and properties of these materials that dominate by the catalyst-adsorbate interactions. The cubic pyrite TMC polymorphs (RuS_2, OsS_2) exhibit surfaces with broken dangling bonds and chemical reconstruction. Prior studies of the RuS_2 surface have shown that an oxygen atom is bound to sulfur but that the surface Ru atoms have bulk-like valence states.[7] In contrast to cubic TMCs, LTMCs exhibit an anisotropic composition. The basal plane of LTMCs is far less reactive than the layer edge due to the basal sulfur layer being coordinately saturated and chemically inert. By obtaining a more fundamental understanding of the chemical and electronic structure of the active site at the layer edge in these technologically important materials, one could rationally

design advanced materials with improved catalytic activity using less costly materials.

2. Properties of LTMCs

2.1. Structural Properties

The 2nd and 3rd row transition metals, group IVb, Vb, VIb, and VIIb can form layered structures by coupling with one of the chalcogens; S, Se, or Te.[8,9] The structures are shown in Fig 1. Within a single layer, the metal atoms are covalently coordinated with six S atoms either in octahedral, trigonal prismatic, or a distorted symmetry. The layer is formed by face-sharing octahedrons or edge-sharing trigonal prisms to form a planar S-M-S sandwich. The bulk crystal structure is formed by stacking these S-M-S sandwiches via van der Waals interactions.

In trigonal prismatic crystal types, the layers are either arranged in two (2H) or three (3R) repeat layers per unit cell (Fig 2). For example, 2H MoS_2 has an AbA-BaB stacking sequence while 2H NbS_2 crystallizes in an AbA-CbC sequence. The 3R MoS_2 polymorph has AbA BcB CaC stacking.[10] The variation in atomic registry with stacking sequence along the stacking direction leads to a number of polytype structures. For example, ReS_2 is a distorted 2H-polytype LTMC having a distorted octahedral structure (Fig 3) resulting in the modification of spacing group from $P6_3/mmc$ to triclinic $P\bar{1}$.[11] This structural distortion leads to a diamond pattern by forming Re-Re bonds.[12,13] The structural parameters of LTMCs with their electrical conductivities are summarized in Table I.

2.2. Electronic Properties

LTMCs exhibit the wide range of electronic properties. These result from the combination of the geometric crystal structures and splitting of the metal d-orbital

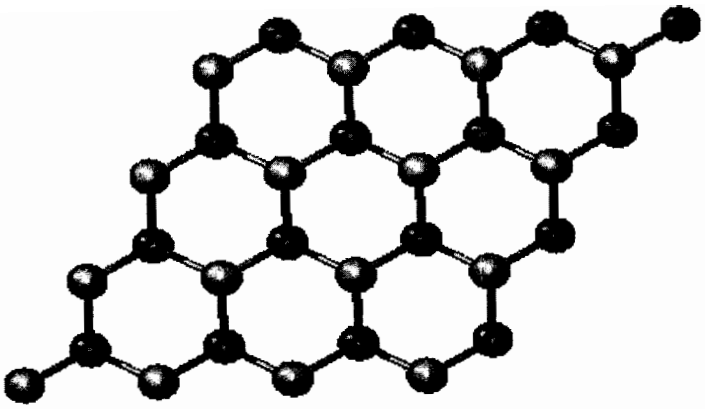

(a)

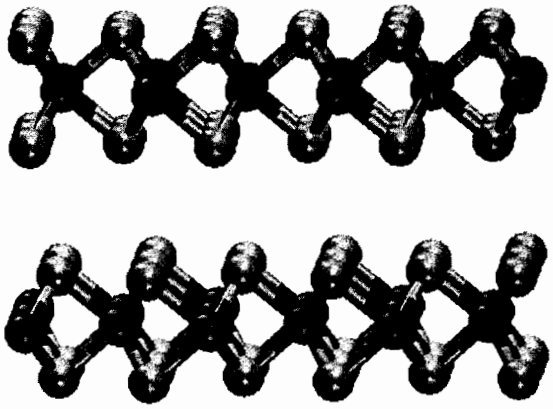

(b)

Fig. 1. Schematic of the crystal structure of trigonal prismatic LTMCs. (a) Top view and (b) side view of trigonal prismatic LTMCs. The light and the dark balls represent transition metal and chalcogen, respectively.

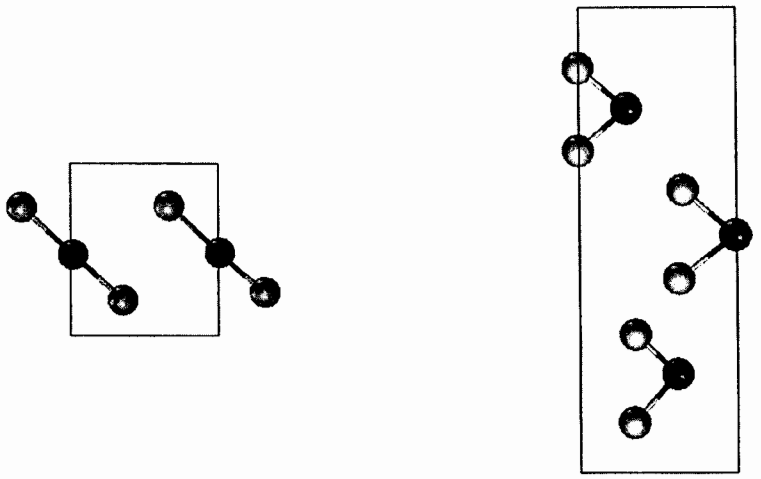

(a)

(b)

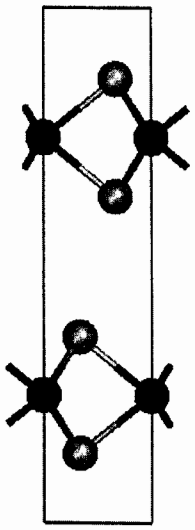

(c)

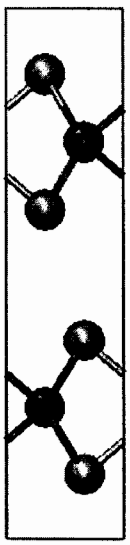

(d)

Fig. 2. Schematic of poly-types of TMCs. The light ball represents chalcogen and the dark ball represents transition metal. (a) 1 T-TMC, (b) 3R-TMC, (c) 2H-MoS_2 type LTMC, and (d) 2H-NbS_2 type LTMC.

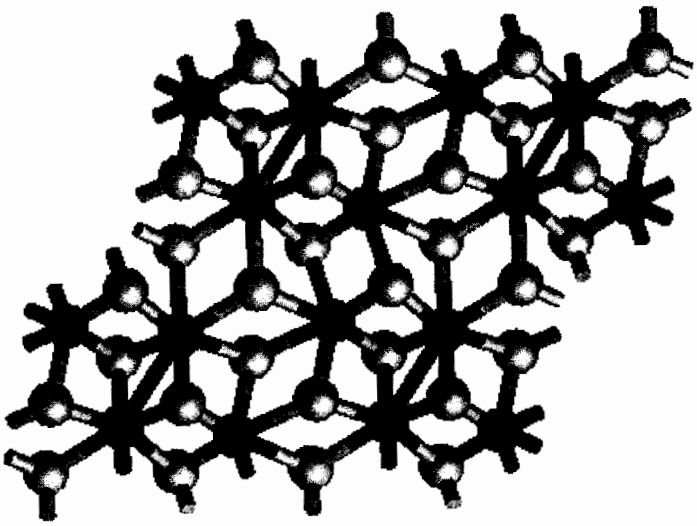

(a)

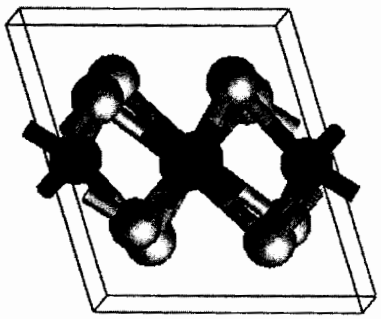

(b)

Fig. 3. (a) Top view of ReS_2 surface and (b) unit cell that contains 4 S atoms and 2 Re atoms. The light ball and the dark ball represent S and Re atoms, respectively.

Table I Structural LTMC Properties

Compound	Space Group	a (Å)	b (Å)	c (Å)	Conductivity	Band gap (eV)
NbS_2	P63/*mmc*	3.310	3.310	11.890	metallic	0.00
$NbSe_2$	P63/*mmc*	3.450	3.450	12.540	metallic	0.00
TaS_2	P63/mmc	3.310	3.310	12.100	metallic	0.00
$TaSe_2$	P63/mmc	3.346	3.346	12.696	metallic	0.00
MoS_2	P63/*mmc*	3.160	3.160	12.294	Semiconductor	1.30
$MoSe_2$	P63/*mmc*	3.288	3.288	12.920	Semiconductor	1.60
WS_2	P63/*mmc*	3.150	3.150	12.260	Semiconductor	1.45
ReS_2	P $\bar{1}$	6.417	6.377	12.779	Semiconductor	1.33

hybridization.[8,9] The degree of hybridization between chalcogen p orbitals and the metal d orbitals results from the symmetry of the electronic band split. The electronic structures of octahedral LTMCs are divided into two orbital groups, t_{2g} ($d_{x^2-y^2}$, d_{z^2}, and d_{xy},) and e_g (d_{yz},and d_{xz}). In trigonal prismatic LTMCs, the d_{z^2} orbital in the t_{2g} group is split causing a shift to low energy states since the d_{z^2} orbitals are weakly hybridized with the p orbital of chalcogen.

The electronic properties depend on the number electrons in the valence band. For example, NbS_2 has one electron in the valence band and is metallic in character while MoS_2 has a completely filled valence band and is semiconducing. ReS_2 has one d-electron in the top of the valence band is semiconducting. In the t_{2g} orbital, the $d_{x^2-y^2}$ and d_{xy} orbitals are aligned parallel to the basal plane while the d_{z^2} orbital is oriented perpendicular to this plane. The $d_{x^2-y^2}$ and d_{xy} orbitals more strongly interact with the S p_x and p_y orbitals than do the metal d_{z^2} orbital, and so the S p_x and p_y orbitals contribute more to metal-sulfur bonding.

2.3. Catalytic Properties

The most common use of LTMCs results from their high degree of sulfur tolerance in hydrogenation catalysis. In fact, these materials have been in wide-spread use for the replacement of sulfur with hydrogen using the hydrodesulfurization (HDS) process in oil feed stocks for more than 75 years. The main emphasis of HDS catalysis has long been in the removal of sulfur during "up-stream" processing of crude oil so that other "down-stream" processing requiring more traditional, sulfur-intolerant catalysts (e.g., Pt, Pd) can be used for other advanced processing reactions.[14,15]

In the past 30-40 years, the removal of sulfur from oil has also been targeted as

a goal for greater environmental performance. In more traditional catalysts, such as base metals (e.g., Pt, Pd) or metal oxides, sulfur acts to poison the catalyst surface. Poisoning degrades the catalyst by deactivation since the strongly adsorbed sulfur, left behind during the HDS process, hinders subsequent adsorption of reactants. HDS catalysis based on single crystal, Pd[16], Pt [16,17] and Rh[18] has been studied. These materials are found to also be structurally sensitive in addition to being susceptible to sulfur poisoning.[19] Metal oxides have been found to be more susceptible than base metals to poisoning by sulfur containing compounds.[20,21] The surface structures are complex due to defects such as step edges, kinks, and adatoms. The presence of these surface defects hinders the catalytic activity due to the defect state's tendency to reduce coordination of the reactant to the bulk surface. In contrast, LTMC based catalysts are well known for their sulfur tolerance and do not appears to exhibit defects that would hinder activity.

The catalytic properties are strongly related to the edge surface structures of LTMCs.[22-24] However, the complexity of the chemical composition and geometry on the active surface has complicated investigation as to the catalytic mechanism on the atomic level.

Chianelli, et al., have proposed that the catalytic activity of TMCs is determined by having the right balance of metal-chalcogen bond strength and the character of the electron states at the top of valence band.[22-24] The bond strength should be high so as to maintain the structural integrity of surface but not to strong so as make it inert. In addition, the higher the metal character in the valence band, the better the catalyst. The proposed study was based on the systematic HDS conversion of dibenzothiophene under typical catalytic operating conditions (about

400°C) using bulk TMCs. The crucial factors appeared to be optimized in RuS_2, which has the highest activity. This study was supported by the calculation method of 'cohesive energy' which is based on the atomization energy and the cohesive bond strength of the material.[25,26] The cohesive energy was calculated by subtracting the heat of formation of the compound from the heat of sublimation. The metal-chalcogen bond strength was represented as the cohesive energy per unit cell per number of metal-sulfur bonds.

3. Surface and Edge Characterization of LTMCs

Many aspects of the basal and active edge planes of LTMCs have been the subject of intense studies using a variety of bulk and surface sensitive techniques, including Auger Electron Spectroscopy (AES),[27] X-ray Photoelectron Spectroscopy (XPS),[28-30] X-ray Diffraction (XRD),[31-33] Transmission Electron Microscopy (TEM)[34,35] and Extended X-ray Absorption Fine Structure (EXAFS).[36] These techniques have provided a firm understanding of the bulk electronic, structural, and chemical properties of LTMCs. These methods are well-suited to investigating bulk material properties but because of low spatial resolution (AES, XPS, and EXAFS) or because they are diffraction techniques that require repeating patterns over several nanometers (XRD, TEM), they are not particularly well-suited to investigating defects.

It is expected that the active site on LTMC catalysts would be highly defective thus limiting the practicality of the above mentioned techniques for investigating atomistic details. The recent development of Scanning Tunneling Microscopy (STM) [37-40] has allowed investigation at atomic resolution in direct space. Thus, the problems of low resolution and the requirement of non-defective materials have

been overcome. STM was used extensively for the investigation of LTMCs in this project as well as in other research.

Materials characterization of solid-state materials reveals the local density of states (LDOS) of the top-most surface (see methods description section). Thus, STM data provides a map of the variation in electronic state density over the surface. Most of the STM studies of LTMCs have focused on the basal plane and variations of the LDOS under various conditions, such as the formation of Charge Density Waves (CDW), [41-43]and the presence of substitutional defects in the metallic or chalcogenide layer.[44]

Kivuitu and Kelty have used STM to study the edge-localized properties of MoS_2 nanoparticles adsorbed on graphite substrates.[45] This first investigation of the layer edge properties at the atomic level revealed that a long-range superstructure dominated the layer edge LDOS topography at the layer edge. More recently, STM has been used to investigate small MoS_2 nanoclusters on Au (111) prepared and imaged under ultra high vacuum (UHV).[46] Helveg et al. studied a MoS_2 nanocluster which was prepared by evaporating Mo in a H_2S environment followed by annealing at 400 ° C for 15 min. The Au (111) substrate surface exhibits the 22 x $\sqrt{3}$ reconstruction known as "herring-bone" structure which is the uni-axial contraction along the Au (110) forming as the double ridges shown in Fig 5.[47] The MoS_2 clusters were oriented onto the herring-bone elbow of the Au (111) surface. In this investigation, MoS_2 nanoclusters were found to be triangle shaped with a side length of about 30Å. The authors argued that the edges consisted of a sulfided Mo edge. The schematic morphology and edge configuration of the STM image is shown in Fig. 4a. In addition, STM data suggested that the LDOS near the edge was

redistributed relative to bulk LDOS such that a new high electron density state was dispersed at the outer-most atomic edge. This group concluded that this new electron state was metallic as indicated from electronic band structure calculations.

It has long been known that the activity of LTMCs toward HDS catalysis is significantly improved if the LTMC is treated with either Co, Ni or Fe. Various models have been proposed to explain the nature of the promotional effect from Ni and Co such as the "pseudo-intercalation" model, in which Co or Ni intercalates between MoS_2 layers[48] near the edge, and the "synergistic" model[49,50] in which the enhanced activity is derived from the presence of both MoS_2 and $Co(Ni)S_x$ moieties.

On the basis of the general conclusion that the catalytically active sites are localized at the coordinatively unsaturated edge, Topsøe, et al., have proposed that the catalytic activity of Co or Ni promoted MoS_2 catalysts is associated with anionic vacancy sites located at the edge[5,49,50] to form a Co (Ni)-Mo-S structure. This promoted structure has been imaged by STM under ultra high vacuum conditions.[51] The cluster was formed by evaporative deposition of submonolayers of both Mo and Co onto the Au (111) substrate followed by annealing at 400 °C for 25 min under H_2S atmosphere. The coverage on the Au (111) substrate was estimated to be 10% for Mo and 4% for Co, which are similar to the ratio of these metals in industrial MoS_2-based HDS catalysts. STM images of Co-promoted MoS_2 clusters exhibited hexagonal-shaped clusters (in contrast to trigonal-shaped native MoS_2 clusters). The hexagonal shape allows for alternate types of edges such as sulfided Mo and S planes (Fig 4 b). The authors argued that the Co atoms were situated in the sulfur plane, instead of the Mo plane. Moreover, the Topsøe group examined the hexagonal morphology of the cluster by controlling the ratio of H_2S to H_2. The

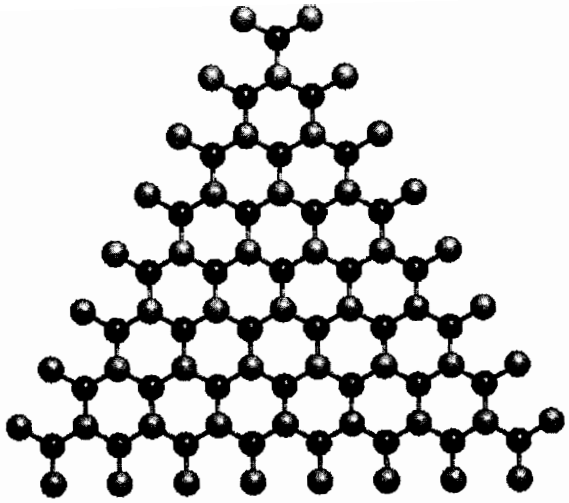

(a)

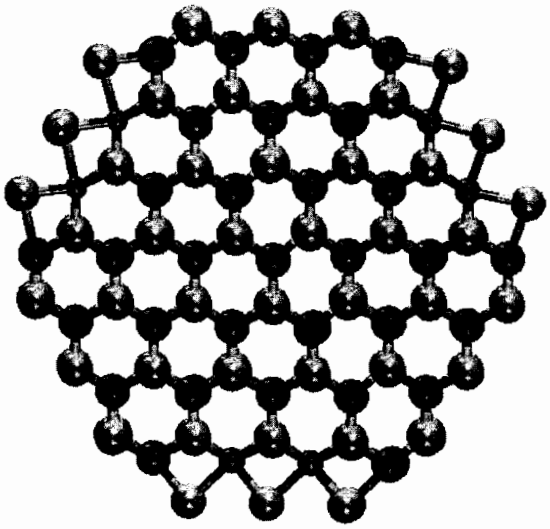

(b)

Fig. 4. (a) Schematic morphology and edge configurations of STM images of MoS_2 on Au (111) taken by Helveg et al.[46] and (b) schematic view of STM image of Co-MoS_2 taken by Lauritsen et. al. [51] Co is decorated on the sulfur edge indicating the smallest dark ball.

termination of the Mo edge is decorated by a sulfur monomer whereas sulfur edge planes are completely coordinated by sulfur atoms. This observation was interpreted in terms of morphological and structural changes being crucial in controlling the industrial catalytic activity.

These experimental STM studies were an excellent approach to understanding the unknown nature of the active sites during the HDS reaction and were theoretically interpreted by Density Functional Theoretical (DFT) modeling. Although this study is notable in that it is perhaps the first attempt to investigate the local details of promoted MoS_2, the promotional effect is not currently believed to involve a single S-Mo-S trilayer. Rather, the Co, Ni, or Fe is believed to contribute electrons to the MoS_2 layers while the guest metal lies either in the van der Waals layer or at the edge.[52,53] Moreover, the influence of the substrate on the nanocluster has been less recognized. It is not clear if the new state was affected by the S-Au interaction between the MoS_2 adsorbate and the substrate. It is well known that Au forms strong bonds with sulfur moieties such as organic thiols. [54-58]

The gold crystallizes in the face centered cubic (fcc) structure and the lattice along the (111) direction is formed as a hexagonal close-packed (hcp) type.[47] The top layer of Au (111) is contracted laterally and formed as $22x\sqrt{3}$ (herring-bone) superstructure to relieve the stress from the coordination distortion of the fcc surface.[59] The stress relief pattern extends toward one of the fcc directions.[60] The array of superstructures is formed by rotating the hcp pattern with respect to the fcc surface by 120°. The nanocluster formation of transition metals (Co, Fe, and Ni) on Au (111) by the evaporation method was studied by using STM. [61,62] For example, the Ni islands are located on the elbows of the herringbone. The island structures

vary with the substrate reconstruction. It was found that the islands tend to reconstruct as a function of increasing annealing temperatures. The islands were diffused laterally and the herringbone pattern was disordered at typical HDS temperatures (Fig. 5). The structurally different pattern points on the herring-bone elbow may influence the exchange between adatoms of Ni and Au atoms near such points. Such interactions between transition metals and Au (111) substrate herringbone pattern may markedly influence the MoS_2 cluster formation by causing a Au adatom-edge atom interaction as a function of annealing temperature. Deposited Mo atoms that are adsorbed on the elbow of herringbone of Au may diffuse since the electron affinities of Mo atom (0.75 eV) [63] are lower than of Ni (1.62 eV).[64] The Mo atom induces a weakening of the bond strength between the Au atom by electronic hybridization between Mo and Au interfaces,[65] so an adatom of Au at the elbow may be exchanged with Mo atoms.

The formation of MoS_2 by the evaporation method was challenged by Rodriguez et al. since the nature of the Mo-Au interaction was not clear.[57,66] This group prepared MoS_2 nanoclusters on Au (111) using $Mo(CO)_6$ and S_2 precursors in a ultrahigh vacuum (UHV) chamber. $Mo(CO)_6$ was deposited onto the Au (111) surface and decomposed to CO and $Mo_x (CO)_y$ aggregation while continuously monitoring with photo emission spectra. The presence of CO- Mo prevents the penetration of Mo metal atoms into the bulk Au and so a Mo-CO monolayer on the Au surface is formed. The nanoparticle adsorbed on the Au surface was then placed in an S_2 atmosphere where MoSx is formed with the subsequent removing CO molecules from $Mo_x(CO)_y$ aggregation. They found that the presence of CO increases the formation of Mo nanocluster preventing Au-Mo intermixing and

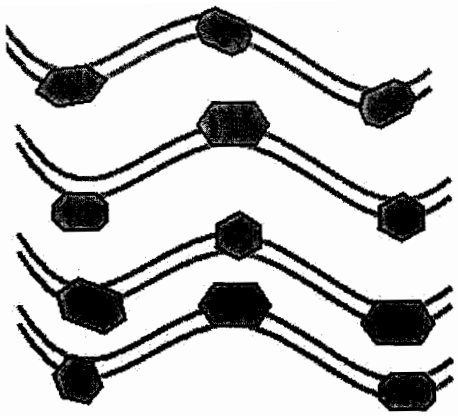

(a)

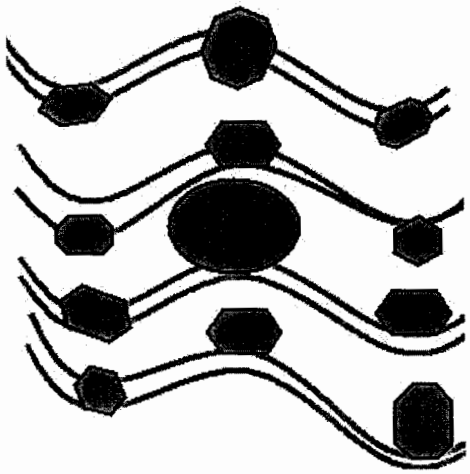

(b)

Fig. 5. (a) Schematic STM images of 0.15 monolayer Ni deposited on Au (111) at room temperature and (b) of 0.15 monolayer Ni deposited on Au (111) after annealing at 450 K.[62]

enhances the MoSx nanocluster formation.

4. Nanostructured LTMCs Properties

Ultimately, the mechanism of adsorption of reactants on the catalyst surface is important. In order to establish the mechanism, it is crucial to have a fundamental understanding of chemical, geometrical, and electronic properties of the active phase of catalyst in advance. The catalytic properties are dominated by the properties of the edge. It has been established that the basal planes of LTMCs are inert to the physisorption and chemisorption of thiopene.[67-69] The physical and chemical properties of the edge are different from the bulk properties largely due to the variation in coordination and oxidation state of the edge sites compared to that of the bulk.[24,70,71]

The ratio of reactive edge plane to inert basal plane increases with decreasing cluster size, so a viable approach to investigating the edge is to prepare nanostructured clusters, which are in effect "all edge". Nanostructured clusters are intermediate in size between molecular and bulk materials and exhibit unique, size-tunable optical and electronic properties.[72-75] For example, it is well known that confinement of the electronic wavefunction in a small regime leads to a redistribution of the electronic structures with consequent change in the conductivity and optical absorption. A major component of this project is to prepare nanostructured LTMC particles and investigate their edge localized properties. This method allows the edge properties to be investigated while avoiding many of the experimental difficulties associated with directly probing the layer edge of bulk materials. These difficulties include simply finding an edge to investigate which are exceedingly infrequent found in bulk materials. Moreover, industrial catalysis

applications rarely use bulk materials as catalysts and so this approach of using small particles is more consistent with typical industrial applications.

5. Simulation Studies of LTMCs

As with most or all experimental investigations, one is often confronted with a problem in which experimental results can not be unambiguously interpreted without complementary computational techniques. Such considerations arise in connection with edge localized chemical and electronic properties of LTMCs as well. In particular, the structural configuration at the edge cannot be clearly defined by STM or other surface sensitive techniques alone. However, many computer simulation approaches have been employed to provide a deeper insight into the structural features of active sites of LTMC catalysts.

In early theoretical studies, variation in HDS activity was interpreted in terms of varying electron density at the top of the valence band for LTMCs using the SCF-Xα method by the Chianelli and coworkers.[2] Further studies of the adsorption site of theophene on the MoS_2 surface using the Extended Huckel Tight Binding (EHTB) [76] and Molecular Orbital (MO) methods [77] have also been used. These methods are insufficient to predict the edge structures since geometry optimization is difficult for surfaces and edges using these techniques (computational demand), but the Density Functional (DF) method has proven to be quite feasible for understanding the nature of the edge including geometrical optimization of the edge structure.

. In typical LTMCs, formation of edge planes results from cleavage of metal-sulfur bonds (Fig. 6 a). For example, MoS2 may be cleaved along several different planes. Cleavage which results in formation of the active sites can be achieved by either

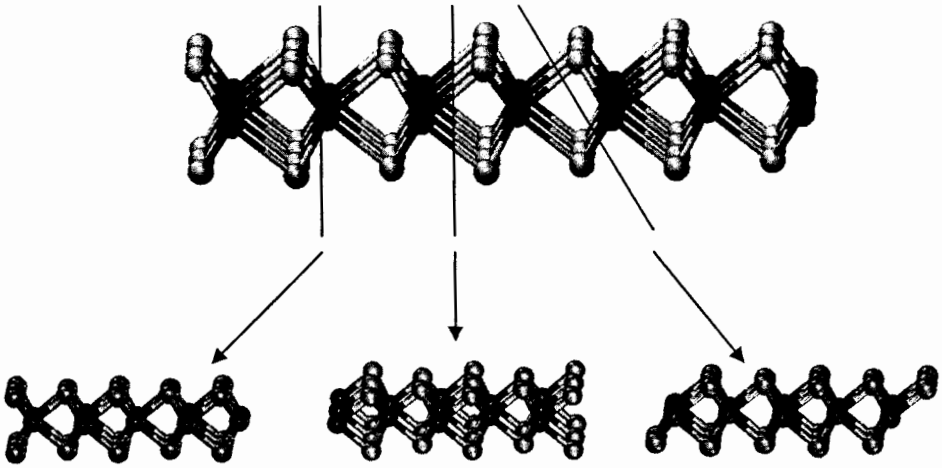

(a)

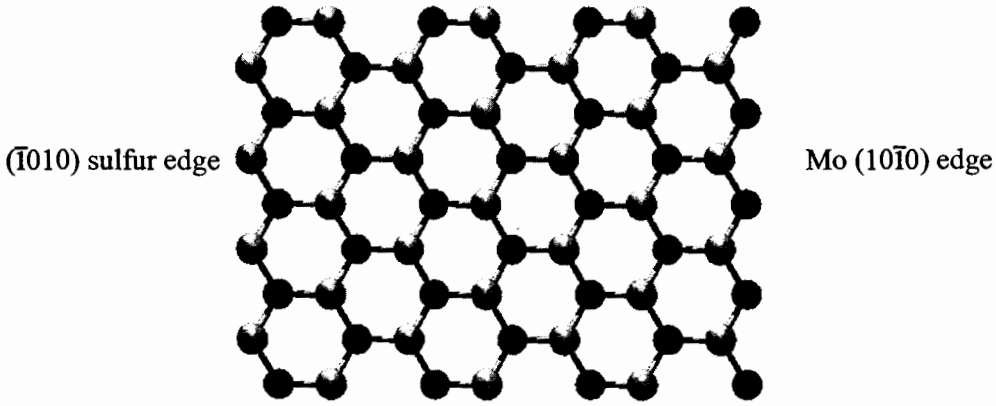

(b)

Fig. 6. (a) Representations of creation of edges cutting planes and (b) of edges: the Mo [10$\bar{1}$0] edge and the ($\bar{1}$010) sulfur edge.

homo- or heterolytically. Recent modeling studies have shown that the stability of the edge structure of LTMCs depends on the chemistry of the resulting edge.[49,67,78-82] Many of these studies were focused on MoS_2 due to the unavailability of the edge structural properties of other LTMCs.

In the bulk MoS_2 crystal structure, Mo atoms are coordinatively bound to six sulfur atoms while each S atom is coordinatively bound to 3 Mo atoms shown in Fig 1 a. A distinction is made between the two sides of the cleavage edge: the $[10\bar{1}0]$ edge terminates in Mo atoms and the $[\bar{1}010]$ edge terminates in sulfur atoms (Fig.6). For each type of termination, there can be two, one or zero terminating sulfur atoms.

The first DF calculation of stable MoS_2 edges was carried out by Byskov et al.[82] Each as-cleaved Mo edge on the Mo_4S_8 ribbon model was terminated with sulfide states by attaching 2 sulfur atoms (Fig 7). Removing half of the sulfur atoms from a completely coordinated Mo edge required 0.15 eV per removed sulfur atom.[83] Further removal of sulfur from the half filled edge was energetically unfavorable by a further 0.6 eV per the removed sulfur atom. They reported that the most energetically favorable edge coverage was that with one sulfur per Mo atom. Moreover, Raybaud et al. used a larger model structure ($Mo_{24}S_{48}$) in another study of edge stabalization (Fig 8).[52] In this study, the enthalpy of sulfur-vacancy formation was calculated by successively adding one sulfur atom up to full coverage on as-cleaved Mo edges. The sulfur-vacancy formation was found to be an exothermic process from half to zero coverage and required 6 eV. In contrast, the removal of sulfur atoms for full to half coverage was an endothermic process and required less than 1 eV. The sulfur-vacancy formations on the sulfur edge were found to be an endothermic and required 1.80 eV from full to half coverage and

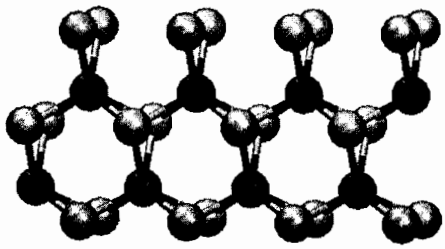

(a)

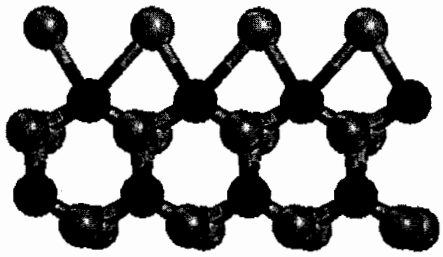

(b)

Fig.7. Representation of 2unit cell Mo_4S_8 model structure. (a) Two sulfur substituted on the one Mo atom of Mo_4S_8 and (b) the most stable edge configuration after the optimization.

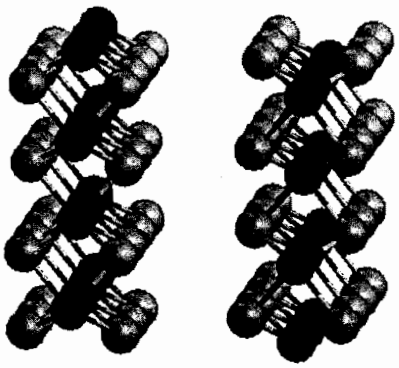

(a)

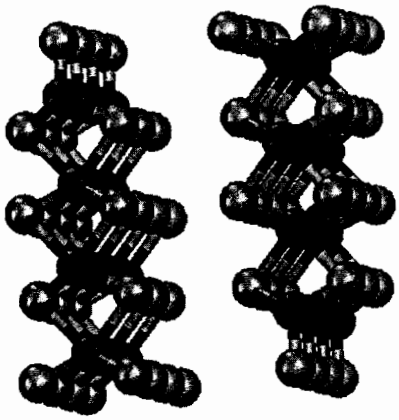

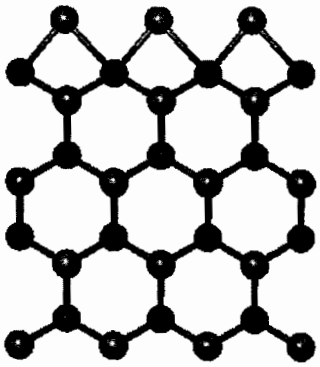

(b) (c)

Fig. 8. Representation of $Mo_{24}S_{48}$ model structure. (a) The model structure without the substitution of sulfur. (b) Side view of and top view of most stable edge configuration after optimization.

9.50 eV from half to zero coverage. These studies revealed that the half sulfur-covered Mo edge and full-sulfur-covered sulfur edge are the most stable configurations.

Raybaud and many other researchers[3,32,84] proposed that the H_2/H_2S gas ratio in HDS catalytic conditions controls the formation of sulfur-vacancies on edges. This finding is consistent with the hypothesis that under HDS working conditions, H_2 adsorbs dissociatively on both the metal and sulfur edges which then react with sulfur atoms to generate a coordinatively unsaturated active sites.[85-88] Within this hypothesis, the sulfur coverage and structural configurations of the edge are determined by the $[H_2S]/[H_2][-S]$ equilibrium. The enthalpy of the structural configuration is expressed as a function of sulfur coverage.

$$MoS_2 + H_2 \Leftrightarrow H_2S + MoS_{2-\delta} \quad (1)$$

where δ represents a sulfur vacancy formed in the reaction The enthalpy of H_2S formation is

$$\Delta E = E(H_2S) + E(MoS_2) - E(H_2) - E(MoS_{2-\delta}) \quad (2)$$

The edge configuration was found to vary with respect to H_2/ H_2S. They found that the most energetically favorable surface is on the Mo edge with half sulfur-coverage in which sulfur atoms are located out of registry with sulfur coordination in bulk MoS_2 which has 6 fold Mo coordination with sulfur. These authors stated that stable edges do not consist of full sulfur vacancy under working HDS conditions. Byskov et al. reported that the dissociation of hydrogen on the full-covered edge lead to the vacancy formation by the exothermic process.[83] In contrast, Raybaud et al showed that the H_2 molecule adsorption on the full-covered edge is the endothermic process and is the meta-stable. Cristol et al. showed that the

vacancy formation on the half-covered Mo edge by heterolytic dissociation is less endothermic; the formation of Mo-H and S-H is more exothermic than the two S- H formations.[86]

The further study of the vacancy formations on the half sulfur covered Mo edge and the low sulfur coordinated sulfur edge were done by kinetics.[89] The heterolytic dissociation of H_2 molecule is more kinetically favorable than the homolytic dissociation. The activation energies of the homolytic dissociations for formations of the one SH_2 and 2 S-H are 1.47 and 1.63 eV. The activation energy of the heterolytic dissociation is 0.97 eV. The rate determining step is the formation of a Mo-H and S-H. After the H atom displaces from the Mo atom to the sulfur atom forming H_2S-Mo, the dissociation of H_2S from the Mo edge requires 0.52 eV. The further removal of sulfur atoms, following the formation of the first sulfur vacancy, is kinetically unfavorable due to the fact that the rate determining step is the H_2S dissociation. The H_2S dissociation has an activation energy of 1.8 eV. From this study, the low vacancy formation occurs at the Mo edge. On the sulfur edge, the removal of one sulfur atom has a higher activation energy of 1.8eV, so the formation of a vacancy on the sulfur edge is unfavorable.

6. Adsorption Studies of Sulfur containing molecules on LTMCs

Theoretical studies suggested that the sulfided metal edge surfaces are the most stable under catalytic conditions; however the initial adsorption sites and the interaction between the sulfur containing substrate and the catalyst surface are not clearly defined at present. The degree of sulfidization at the catalysts surface influences the adsorption of the substrate on the catalyst surface since the number of the adsorption sites are reduced at high sulfidization due to steric hindrance on the

edge plane. Therefore, systematic theoretical-studies of initial binding states of substrates, specially thiophene on both pristine and sulfided catalysts are critical to obtain a better understanding of the initial stages of the HDS catalytic mechanism.

Zonnevylle et al., investigated the adsorption of thiophene on the Mo edge of MoS_2 using the Extended Huckel Tight Binding (EHTB) method.[76] They reported 3 possible thiophene binding coordinations termed η^1, η^2 and η^5. In the η^1 and η^5 coordinations, the thiophene molecular plane is placed perpendicular to (so that only the sulfur atom is coordinated) and parallel to (so that all five atoms in the thiophene ring) the Mo edge surface, respectively. In addition, both S-C_α bonds can also interact with the Mo atoms and this adsorption geometry is called η^2. The thiophene/MoS_2 system is shown in Fig. 9. The adsorption energy of thiophene on the MoS_2 edge surface was calculated according to:

$$E_{adsorption} = E_{thiophene-MoS_2} - E_{thiophene} - E_{MoS_2} \quad (3)$$

The authors suggested that in the η^5 coordination the thiopene ring is bridged between two Mo atoms, and is more energetically favorable than the η^1 and the η^2 coordinations, in which the thiopene ring is located on top of the Mo atoms. A more accurate adsorption geometry was calculated by Raybaud el al.[78] They calculated thiophene adsorption on a bare Mo edge surface of a two-trilayered slab model using the DF method. The most stable coordination was found to be the bridged η^5 coordination (Fig 10 a). In this coordination, the adsorption energy of thiophene is 2.00 eV. In contrast, the least stable coordination is top-on η^1 coordination with 0.94 eV.

Orita et al. calculated the thiophene adsorption on a small MoS_2 cluster.[90] The calculation was simplified by reducing the $Mo_{27}S_{54}$ hexagonal cluster to a $Mo_{16}S_{32}$

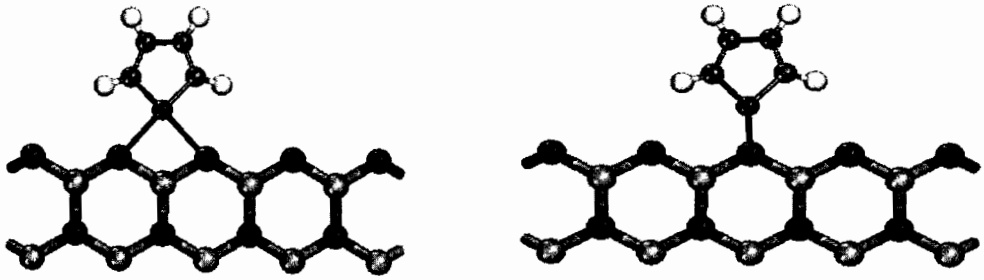

η^1

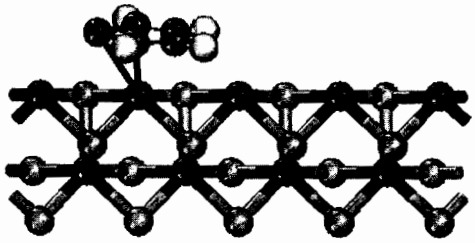

η^2

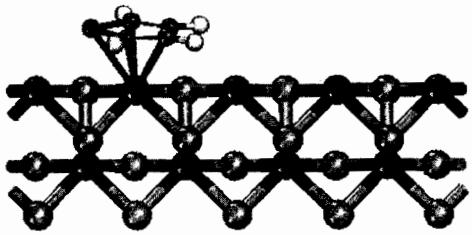

η^5

Fig. 9. Representatiion of thiophene adsorption configurations on the coordinatively unsaturated Mo edge surface.

cluster (Fig 10 b). The authors argued that this smaller cluster should have similar edge properties to the hexagonal model structure since both clusters are stoichiometric and electroneutral. For this system, it was found that the most stable coordination is the rotated η^2-S, C. η^2-S, C is formed by rotating from the bridged η^5 coordination, which is similar to the one reported by Raybaud et al., to a position in which the sulfur atom in the thiophene is slightly away from the Mo atom. This rotation weakenes the C-S bond strength thus leading to C-S bond dissociation. The adsorption energy for this model is 2.72 eV which is higher than that reported by Raybaud et al.

It is difficult to interpret whether this rotated coordination is more stable or not because the simulation parameters and model structures are different, but these results indicate that the parallel and bridged adsorption geometries of thiophene are more stable. It is assumed that under theoretical HDS conditions, that the metal edge is sulfided and hydrogenated and that the subsequent formation of a vacancy site requires high energy to remove sulfur. The number of such vacancies and coordinatively unsaturated Mo configurations are currently debated due to the difficulty in identifying where and how the S-H groups form.

Cristol et al. calculated the adsorption energies of dibenzothiophene (DBT) and its derivatives with respect to the formation of vacancy sites on the half-sulfur covered edge.[91] The three possible active sites are formed at the catalytic conditions shown in Fig 11. The first and second active sites are on the Mo edge and a third one is on the sulfur edge. The energy for the one sulfur vacancy formation is 1.3 eV on the half-sulfur covered edge. The successive removal of sulfur atom from the first site from which a sulfur atom was removed is 2.1 eV. Moreover, the removal

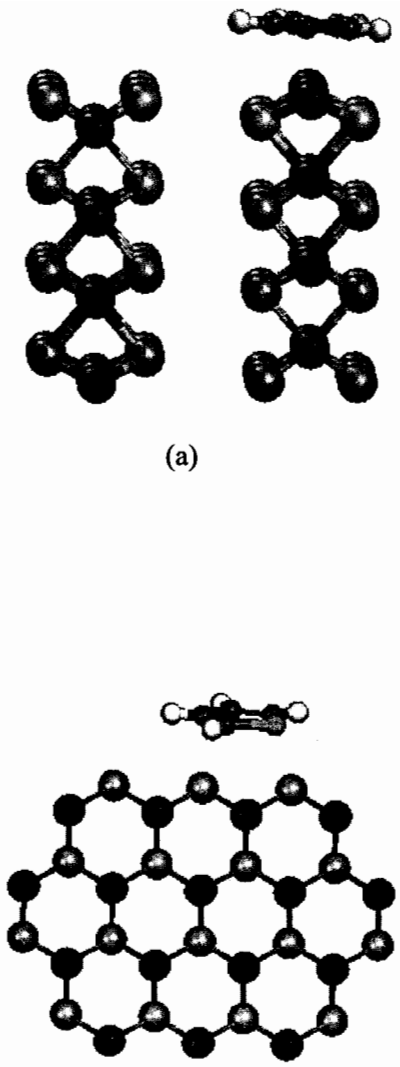

Fig. 10. Two different types of model structures for thiophene adsorption. (a) slab and (b) cluster structures.

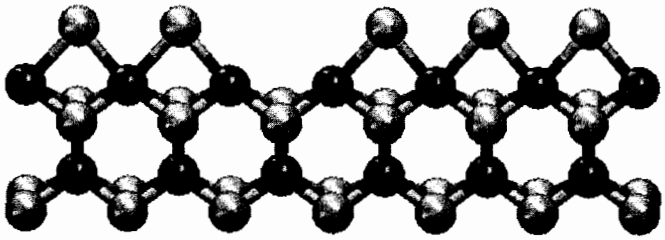

(a)

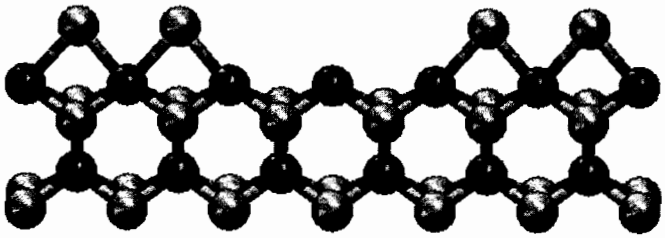

(b)

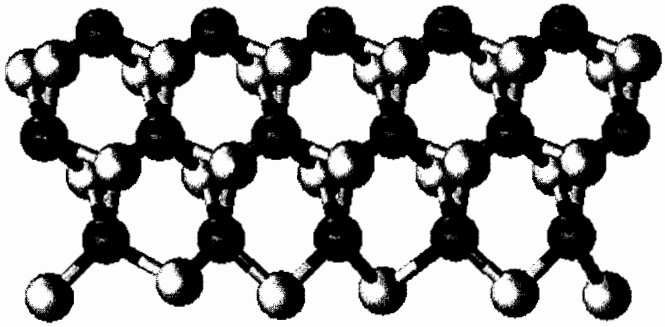

(c)

Fig. 11. The representation of active site formations: (a) one and (b) two sulfur vacancy formations on Mo edge and (c) sulfur vacancy formation on sulfur edge.

energy of sulfur atom for third site on the sulfur edge is 2.9 eV. The sulfur vacancy formation more than two requires the high energy, so the 3-fold sulfur-vacant Mo edge is not easily formed under HDS conditions. Cristol et al. stated that the adsorption geometric configurations of DBT and its derivatives on MoS_2 are all on-top perpendicular to the edge direction. It is the contrast to the adsorption studies of thiophene on the bare Mo edge which the thiophene ring with the on-top adsorption is less activated than the parallel-bridged adsorption. It is shown that the sulfur coverage and the vacancy formation control the catalytic mechanism of sulfur-containing molecules adsorbed on the active sites. Therefore, the interaction between adsorbate on the bare site and either the sulfur atom or the hydrated sulfur atom on the sulfur covered Mo sites is considered.

Lobos et al. studied the electronic configuration of the adsorbate-sulfided-edge interaction on the Mo edge of Mo_5S_{18} (Fig 12) using the CNDO / UHF (complete neglect of differential overlap / unrestricted Hartree-Fock) method.[92] One corner edge site of the cluster was sulfided while the other had a bound S-H group. Thiophene was adsorbed on bare Mo sites. The HOMO was found to be localized on the sulfur atoms at the edge indicating that the electron-donating site to the thiophene which S-C bond is weakened, whereas LUMO is located on the bare metal atoms at the edge indicating the electron accepting sites.

7. Project Approach and Outline

The aim of this research is to characterize the novel electronic and crystal structure at the edge and near edge of LTMCs. The experimental investigation of edges was performed using Scanning Tunneling Microscopy (STM). The nature of how these nanoparticles terminate at edge and the variation of edge structural and

electronic properties from bulk are established. To properly distinguish the material characteristics which are responsible for the image data features, it is crucial to include modeling studies. The electronic and structural properties are interpreted by comparing experimental with simulated STM images. Simulated STM images were calculated using the Extended Huckel Tight Binding (EHTB) method applied to either bulk termination ribbons or geometrically optimized ribbon structures obtained using Density Functional (DF) calculations. The second portion of the project is to repeat the above experimental and computational studies on LTMC edges which have been chemically treated with thiols.

This section reviewed the experimental and theoretical studies reported in the past of bulk and nanostructured LTMCs that are used as a basis for this study. Section II gives a theoretical overview of the STM, DFT, and EHTB methods. Section III, first describes the experimental STM studies that probe the catalytically active surface. Also section III demonstrates the model structures of edge configurations and set up parameters for the band dispersion, density of state (DOS), and the adsorption energy calculations. In section IV, we discuss the interpretation of the STM results of nanoclusters and a comparison with simulated STM images and the calculated electronic and atomic structures. The conclusions are provided in section V.

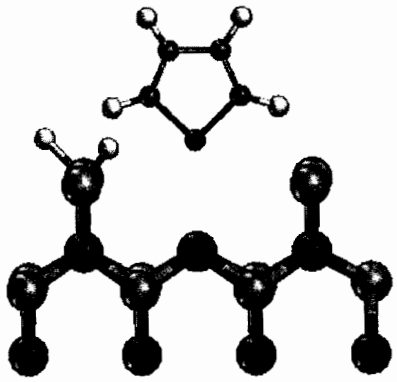

Fig. 12. Adsorption structure of thiophene on the sulfided Mo edge.

II. STM Theory and Computational Algorithms

The fundamental understanding of catalytic reactivity and properties requires a detailed view of local states on LTMC defect surfaces. Catalytic reactivity and properties are dominated by such states; consequently, atomic scale investigations are needed to probe the atomic and electronic structures at the defect states. There are many surface sensitive techniques available which can contribute to a better understanding of these important properties. These techniques can be divided into either reciprocal- or direct-space techniques. In general, the reciprocal-space techniques (such as electron or X-ray diffraction) offer atomic scale resolution information but only for periodic (defect-free) materials with coherence lengths on the order of 10 nm or more. Conversely, direct space techniques (such as Auger electron or X-Ray photoelectron spectroscopy/microscopy) offer the capability of studying defects as well as periodic systems albeit at considerably lower resolution than diffraction techniques (ca. 10 nm). Scanning Tunneling Microscopy (STM) and related proximal probe techniques are direct space techniques, but since their resolution is not Bragg limited they offer an unparalleled ability to probe the local defect structure at the atomic scale.

Like any experimental technique, STM data requires careful interpretation which can only properly be done with complementary techniques including computational chemistry. In recent years, significant developments in computational chemistry have provided a means of complementing STM with modeling and simulation based on well-validated algorithms. Consequently, it is now possible to interpret STM images thus providing information on the electronic and atomic structure. Therefore, the

combination of experimental STM and theoretical computation is capable of improving the understanding the detailed knowledge of edge properties to explain the catalytic reactivity and properties.

A. STM Theoretical concepts and operation

Scanning Tunneling Microscopy (STM) was introduced by Gerd Binning and Heinrich Rohrer at the IBM Research Institute at Zurich in the early 1980s.[93, 94] In 1986, they were awarded the Nobel Prize in Physics for the invention of the instrument. This achievement represents the first instrument capable of imaging the surface of metallic and semiconducting materials at atomic resolution in direct space. STM has been used to probe the physical and chemical properties of a wide variety of materials and has led to a far more fundamental understanding of the surface properties of these materials than was available from more traditional surface sensitive techniques.[95-97] STM, which is sensitive to the atomic level electron configuration is a direct-space technique and so is well-suited for investigating the electronic and structural details of surface defects and edges of nanoclusters.[45, 50]

1. Electron Tunneling and STM

STM exploits a quantum mechanical phenomenon, in which electrons are able to penetrate the classically forbidden potential barrier between conductors.[98] Within the framework of Quantum Mechanics, Bloch showed that solutions to the Schrodinger equation with a periodic potential are in the form

$$\Psi(r) = e^{ik \cdot r} U_k(r) \qquad \text{(II-1)}$$

in which $U_k(r)$ is a function having the full symmetry of the crystal and is dependent on

the inverse wavevector k.[99] The wavevector k is represented by

$$k = \frac{2\pi}{nV} \tag{II-2}$$

where n is a quantum number for the three dimensional state and V. is the volume of the unit cell repeat unit. In the classically forbidden region external to the crystal, the wavefunction probability does not abruptly become zero but decays exponentially into the vacuum region outside of the material. This decay of this wavefunction as a function of distance x from the crystal edge is

$$\Psi(x) \propto e^{-ik\cdot x} \tag{II-3}$$

If another material exists nearby, with a decaying wavefunction in the vacuum region, the two wavefunctions can overlap and quantum mechanical tunneling may occur. The only requirements for tunneling are that 1) the two materials are sufficiently close so that the amount of eigenvector overlap is significant and 2) that the energy eigenvalue of the two wavefunctions also match. The net result of tunneling is that an electron may translate from one material to the other iso-energetically, without having to overcome the potential for an ionization process. Within the one-dimensional electron tunneling approximation,[100] the rate of electron transfer (current) between the two materials s and t is:

$$I_{tunn} \propto V_{bias}\left|\Psi_t(r)\right\|\Psi_s(r)\left|e^{-d\sqrt{2m\Phi/\eta^2}}\right. \tag{II-4}$$

where m is the electron mass, V_{bias} is the difference in energy of the highest filled electronic states (Fermi level), $\Psi_t(r)$ and $\Psi_t(r)$ are the overlapping wavevectors, Φ is the

average workfunction, and d is the separation between the two materials. In this expression, the terms to the right of V_{bias} represent the conductance (inverse resistance) of the tunneling junction within the framework the familiar Ohm's Law, I = V/R. While the one-dimensional tunnel junction contains all the important points needed to explain the tunneling process, it is not sufficient to describe the use of a tunneling junction as a microscope. They treated the tip as the hydrogen-like wavefunction to overcome the dimensional problem. In an STM, one of the materials is a sharp metallic tip and the exponential decay of a wavevector originating from the tip must be described in three-dimensions. A successful way to do this is to treat the tip wavevector as spherically symmetric, i.e. as a hydrogenic s-orbital.[100, 101] The magnitude of the tip s-wave exponential decays radially and the 3D tunnel junction may be represented as a sum over azimuthal angle, each of which contributes to the total current between tip and sample. It has been shown that by treating the tip wavefunction as a constant, any variation in tunneling current between the tip and sample is due to variations in the Local Density of States (LDOS) of the sample. [101]

$$I_{tun} \propto V_{bias}\rho(r)e^{-d\sqrt{2m\Phi/\eta^2}} \qquad \text{(II-5)}$$

where ρ(r) is the LDOS at the point r above the sample surface. A detailed description of this theory is presented in section B-1.4.

In Fig 13 is shown a cross-section of a STM tunnel junction. When no bias voltage is applied, the tip and sample Fermi levels are aligned and no net tunneling current occurs since the likelihood of a tunneling event to the right is the same as that for tunneling to the left (Fig. 13a). Otherwise, when a bias voltage is applied between the sample and

tip, the potential energy of the electrons in the sample are raised with respect to the tip (Fig. 13b) and a net tunneling current from the sample to the tip is measured.

In the case of an oppositely biased tunnel junction, current occurs from the tip to the sample. If the sample is a semiconductor, tunneling may occur from the top of the valence band of the sample or into the bottom of the sample conduction band.

The tunneling current depends on four parameters: bias voltage, sample-tip separation, the sample LDOS, and the relative workfunction. The bias voltage determines the energy level of the sample that is to be probed and is set by the user. The relative work function is determined by the nature of the tip and sample materials and is a constant in a given experiment. The tip-sample separation and LDOS are mutually independent variables in the experiment which must be determined by an independent method if proper image interpretation is to be made. In essence, the measured tunneling current depends on both the tip-sample separation which is determined by the local geometry of the sample surface, and also on the LDOS which is determined by the electronic properties of the sample surface. Without an independent means to discern the relative contribution of local geometry and electronic structure to the tunneling current, data interpretation is not possible unless inappropriate assumptions are made. As part of this project, simulations of STM image data were performed using computational methods in order to permit proper interpretation of the image data.

2. STM Components and Instrumentation [94, 102-104]

STM instrumentation has been commercially available since the late 1980's.

Common to these instruments are several key components including: a sample positioner (scanner), a current measurement device sensitive to sub-nA current levels, and a feedback loop circuit to permit precise control of the tip-sample separation during image collection. The STM components are described in Fig.14. To initiate a STM experiment, the tip must be position close to the sample surface, which is accomplished by a coarse approach mechanical stepping motor. To bring the tip to within tunneling distance, the tip is translated toward the sample by means of a piezoelectronic z-axis drive. In the instrument used for this work, a Park Scientific Instruments model CP, the piezoelectronic scanner is the tube-scanner type, commonly found in most modern STM instruments. The piezotube bends and expands in response to an applied bias voltage from the controller. The x and y lateral movements are accomplished by applying a voltage radially across the diameter of the tube. The z-axis (height) movement is accomplished by applying a voltage along the length of the tube. In general, the x, y, and z movements are not completely orthogonal and independent in piezotube scanners; however they do offer superior response characteristics in comparison to other scanner designs such as tripod types. In the instrument used the tip remains stationary in the laboratory frame and the sample is moved vertically and laterally by the piezoelectric tube scanner.

During scanning, the sample is rastered under the stationary tip and the tunneling current is measured as a function of lateral position in order to maintain an appropriate tip-sample separation and prevent the tip from crashing into the sample surface. The measured instantaneous tunneling current is compared to a predetermined current

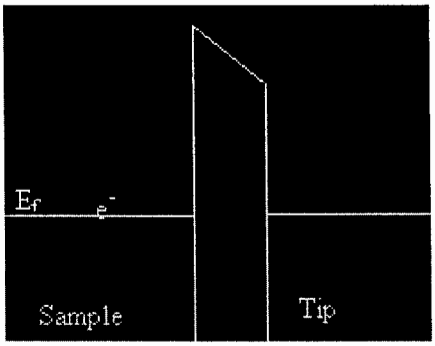

(a)

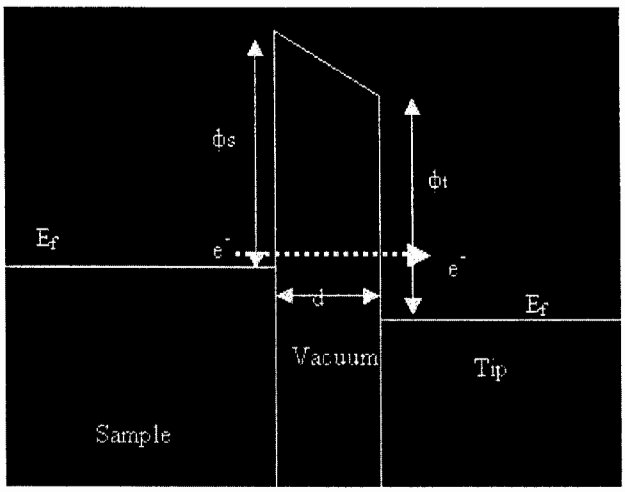

(b)

Fig. 13. Electron tunneling between sample and tip: (a) without bias voltage applied and (b) with bias voltage applied. Φs and Φ_t are sample and tip workfunctions respectively, E_f is Fermi level, and d is sample-tip separation.

setpoint. Any difference (positive or negative) between the setpoint and instantaneous current is used to place a voltage, via a feedback loop, on the piezotube z-axis to move the tip up or down as appropriate. A response gain on the feedback loop can be user adjusted in order to maintain stable imaging conditions. Thus, by increasing the gain, the tip is made to follow the contour of the sample geometry/LDOS such that the image data represents a contour of constant current density. Conversely, at low gain, the tip is adjusted up or down over an average of a large number of current samplings. Images collected under conditions of low feedback gain represent contours of current density variation at a constant height above the surface. These two types of image collection are termed "constant current" and "constant height".

Since STM probes the sample surface at a short distance of 1-10Å from the sample surface, STM is highly sensitive to the influence of vibrational noise. In general, vibrational noise sources may be classified into acoustic and mechanical. Mechanical vibrations include the building vibration and local equipment noise such as mechanical pumps. In order to abate these mechanical noise sources, the instrument is placed on a vibration isolation table which floats on air-charged pistons. A side view of the vibration isolation table is shown in Fig. 15. The room that the instrument occupies is fitted with sound proofing in order to help eliminate acoustic noise.

In STM studies, a sharp tip is required having a maximum radius of curvature of 1 nm. In most cases, such tips can be prepared routinely by simply cutting a metal wire at a sharp angle. Stresses in the metal result in the formation of asperities on the cut end of the wire. These asperities can be used as the STM tip. The tips that were used in this

study were cut from Pt/Ir (80/ 20%) alloy wire. Tips prepared by cutting wire were compared with tips prepared using an electrochemical etching method.[105] Atomically resolved STM images could be collected using both methods. Since STM images obtained by using the etching method were not significantly improved over the more simple cutting method, even though etched tips exhibit sharp apexes and smooth surfaces.

B. Computational Algorithms

1. STM Image Simulations and Electronic Structure Calculations

1.1. Crystal Orbitals [106-108]

A crystal is an array of atoms or group of atoms with a periodic repeating pattern. The unit cell represents the smallest repeat pattern containing a minimal number of atoms that is representative of the material. The crystal structure is obtained by translating the unit cell in three dimensions. The unit cell can be represented in direct space by a set of translational vectors. The position of atoms within the unit cell are presented by the translational vector R,

$$R = ma + nb + pc \tag{II-6}$$

where a, b, and c are components of a vector representing the unit cell axes and m, n, and p are integers. In addition, the crystal can be conveniently represented in reciprocal space by a set of reciprocal lattice vectors K:

$$K = xa^* + yb^* + zc^* \tag{II-7}$$

where a^*, b^*, and c^* are the lattice constants of the reciprocal lattice and x, y, and z are integers. The relationship between direct and reciprocal space lattice vectors is:

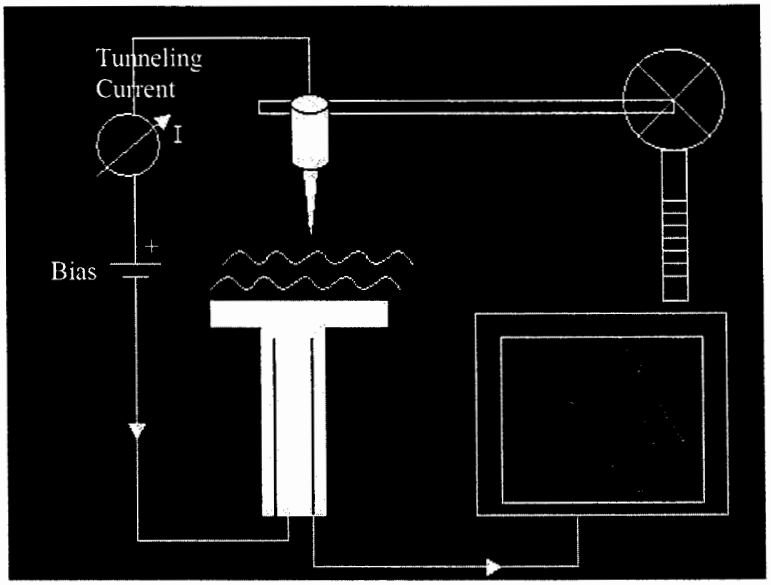

Fig. 14. Schematic of STM components. The sample against a stationary tip is moved by a piezoelectric tube. Feedback is used to maintain the probe-sample distance at a constant current or distance. By following a raster pattern, the signal as a function of tip-sample separation forms an image of the probe surface interaction.

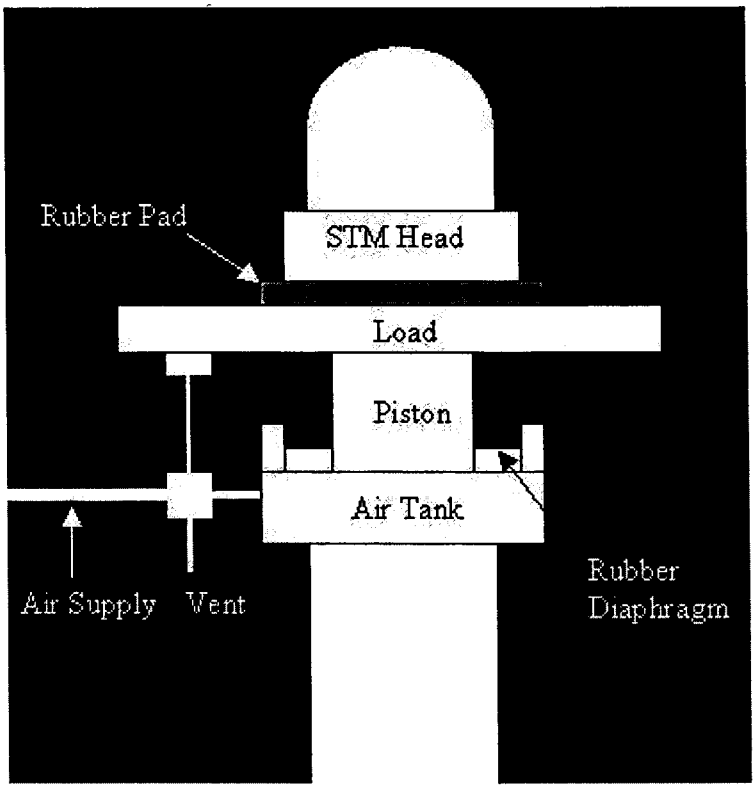

Fig. 15. Schematic of STM instrument set-up with vibration isolation table.

$$a^* = \frac{b \times c}{a \cdot b \times c} \qquad b^* = \frac{c \times a}{a \cdot b \times c} \qquad c^* = \frac{a \times b}{a \cdot b \times c} \tag{II-8}$$

The periodic wavefunction for a crystal orbital can be represented as:

$$\phi(K) = e^{iK \cdot R} U(R) \tag{II-9}$$

in which U(R) is a function with the full periodicity of the crystal (completely analogous to the description above for overlapping wavevectors). In order to treat multi-electronic orbital systems, an approximation is used in which the crystal orbitals are expanded as a linear combination of atomic orbitals.

$$\Psi_i(K) = \sum_u c_{ui}(K) \phi_u(K) \tag{II-10}$$

where the c_{ui} are expansion coefficients of the Bloch functions $\phi(k)$ that must be optimized to produce the resultant wavevector Ψ_i.

The crystal orbitals Ψ_i and energy eigenvalues are obtained from solution of the Schrödinger equation

$$H\Psi_i(K) = E_i \Psi_i(K) \tag{II-11}$$

by solving the variational integral:

$$E_i = \frac{\langle \Psi_i(K) | \hat{H} | \Psi_j(K) \rangle}{\langle \Psi_i(K) | \Psi_j(K) \rangle} \tag{II-12}$$

The Dirac bracket notation has been used here in which:

$$\langle U | \hat{A} | V \rangle \equiv \int U^* \cdot \hat{A} V \text{ and } \langle U | V \rangle \equiv \int U^* \cdot V \tag{II-13}$$

By substituting eq. II-10 into eq. II-12 we obtain:

$$E_i = \frac{\sum_u \sum_v c_u c_v \langle \phi_u(K) | \hat{H} | \phi_v(K) \rangle}{\sum_u \sum_v c_u c_v \langle \phi_u(K) | \phi_v(K) \rangle} \tag{II-14}$$

Eq. II-14 is simplified by introducing the notation,

$$\hat{H}_{uv}(K) \equiv \left\langle \phi_u \middle| \hat{H} \middle| \phi_v \right\rangle \tag{II-15}$$

$$\hat{S}_{uv}(K) \equiv \langle \phi_u | \phi_v \rangle \tag{II-16}$$

$$E_i = \frac{\sum_u \sum_v c_u c_v \hat{H}_{uv}(K)}{\sum_u \sum_v c_u c_v \hat{S}_{uv}(K)} \tag{II-17}$$

The energy is minimized with respect to coefficients c_{uv}

$$\frac{\partial E_i}{\partial c_{uv}} = \frac{\partial}{\partial c_{uv}} \left(\frac{\sum_u \sum_v c_u c_v \hat{H}_{uv}(K)}{\sum_u \sum_v c_u c_v \hat{S}_{uv}(K)} \right) \tag{II-18}$$

which produces a set of n eigenvalue equations (for an n-electron system) of the type:

$$\sum_{u=1}^{n} \left(\hat{H}_{uv} - E_i \hat{S}_{uv} \right) c_u = 0 \quad \text{where } v = 1 \ldots n \tag{II-19}$$

each providing an energy eigenvalue corresponding to an electronic state defined by a set of c_u. The n energies of crystal orbitals are obtained by solving the secular determinant.

$$\begin{vmatrix} \hat{H}_{11}(K) - E_i \hat{S}_{11}(K) & \hat{H}_{12}(K) - E_i \hat{S}_{12}(K) & \cdots & \hat{H}_{1n} - E_i \hat{S}_{1n}(K) \\ \hat{H}_{21}(K) - E_i \hat{S}_{21}(K) & \hat{H}_{22}(K) - E_i \hat{S}_{22}(K) & \cdots & \hat{H}_{1n} - E_e \hat{S}_{2n}(K) \\ \vdots & \vdots & \cdots & \vdots \\ \hat{H}_{n1}(K) - E_i \hat{S}_{n1}(K) & \hat{H}_{n2}(K) - E_i \hat{S}_{n2}(K) & \cdots & \hat{H}_{nn}(K) - E_i \hat{S}_{nn}(K) \end{vmatrix} = 0 \tag{II-20}$$

The solution of the determinant (II-20) is facilitated by the use of appropriate approximations for the diagonal and off-diagonal integral elements. The integral $\hat{S}_{uv}(K)$ is called the overlap integral and represents the extent of overlap of crystal orbitals u and v. Obviously, every orbital completely overlaps with itself and so all of the diagonal overlap integrals $\hat{S}_{uv}(K) = \hat{S}_{11}(K) = \hat{S}_{22}(K) = \hat{S}_{nn}(K) = 1$. Moreover, the diagonal $\hat{H}_{uv}(K)$ elements (for u = v) are called the Coulomb integrals and can be approximated by the ionization potential (IP) of the orbital. Finally, the off-diagonal elements are treated using substitutions for the overlap $\hat{S}_{uv}(K)$ and resonance (or "hopping") integrals $\hat{H}_{uv}(K)$ for which u $\neq$ v taken from *ab initio* or other self-consistent methods.

1.2. Extended Hückel Tight Binding (EHTB) Method

The Huckel molecular orbital method provides molecular orbital structure for conjugated carbon pi-systems. The EHTB method, developed by Hoffman [109] uses the same semi-empirical methodology applied to the electronic structures of organic and inorganic molecules as well as solids. The EHTB method uses ϕ basis functions derived from hydrogen-like Slater Type Orbitals (STOs) and separating valence electrons from the core electrons. In the EHTB method, valence orbitals are treated explicitly while the core electrons only act to shield the nuclear charge to form an effective nuclear charge on the valence electrons. The STOs are defined as follows

$$\phi_u(r,\theta,\varphi) \propto r^{n-1} e^{(-\xi r)} Y(\theta,\varphi) \qquad \text{(II-21)}$$

where n is the principle quantum number, ζ is an adjustable orbital exponent, and $Y(\theta.\phi)$ is the spherical harmonic. The STOs are appoximate atomic orbitals exposed to an effective nuclear charge. In addition, the STOs can be improved by the substitution of one more additional orbital exponents

$$\phi_u(r,\theta,\varphi) \propto (c_1 r^{n-1} e^{(-\xi.r)} + c_2 r^{n-1} e^{(-\xi.r)}) Y(\theta,\varphi) \qquad \text{(II-22)}$$

The valence electron Hamiltonians are defined as the sum of the effective hydrogen-like Hamiltonians

$$H = \sum_u H^{eff}(i) \qquad \text{(II-23)}$$

Crystal orbitals are, in turn, expressed as a linear combination of effective atomic orbitals. The energies of the crystal orbitals are calculated by the matrix equation, eq. II-20. The off-diagonal H_{uv} elements are approximated by the use of Wolfsberg-Helmholz expression as

$$H_{uv}^{eff} = \frac{1}{2} K (H_{uu}^{eff} + H_{vv}^{eff}) S_{rs} \qquad \text{(II-24)}$$

where K is a constant (typically 1.75), H_{uu}, H_{vv} are the coulomb integrals, and S_{uv} is the overlap integral as described above.

1.3. Band Dispersion and Density of States (DOS) [110, 111]

The reciprocal lattice (eq. II-7) that define the periodicity of a crystal correspond to the all direct space properties of the crystal. The concept of the reciprocal lattice contributes to an appreciable reduction in simulation size. Therefore, it is adequate to

study the properties of a crystal within the framework of the reciprocal lattice since all of the materials properties may be derived from it. In particular, the energy of the electronic states is found to vary over the reciprocal space lattice. The primary reciprocal lattice that refers to the largest repeat distance in direct space (the smallest repeat period in reciprocal space) is referred to as the First Brillouin Zone (FBZ). In other words, the FBZ is to reciprocal space what the unit cell is in direct space. In contrast to molecular systems, in which the electronic state energies are discrete, crystal orbital energies can vary over the FBZ. The variation in electronic state energy as a function of the wavevector (location in the FBZ) results in energy bands. Periodic boundary conditions at the BZ edges force the wavevector to split and intersect the BZ edge at right angles. For example, Fig. 16a shows the E vs. k band diagram for a free electron. In this case the electronic energy is $E = \hbar^2k^2/2m$ which simply shows a quadratic dependence on energy with wavevector. When the electron is subject to the periodic potential of the crystal, the electron scatters from the BZ edge since at and near the point at which the electronic wavelength matches that of the crystal frequency. This effect can be seen in Fig 16b which shows the formation of a forbidden energy region labeled ΔE. If the material has a sufficient number of electrons to completely fill the band below the gap, the material will be semiconducting or insulating depending on the energy width of the gap. Otherwise, if the material has a partially filled band, it will be metallic such that electrons may translate from one lattice point to another so long as the new location is an unoccupied one. In semiconductors, the only way an electron may translate is for it to obtain sufficient energy to be promoted into the bottom of the

upper empty band. In semiconductors, the lower filled band is called the valence band while the upper empty band is called the conduction band. The electronic band structure dispersion curves are normally plotted along high-symmetry directions in the FBZ. In addition, high symmetry locations in the FBZ are given labels. For example, Γ is the center point, k=(0,0,0). The reciprocal unit cell for a hexagonal crystal is shown in Fig. 17 with symmetry labels.

For each band in the dispersion curve the density of electronic states N(E) (DOS) can be plotted using:

$$N(E) = \frac{dE}{dk} \tag{II-25}$$

The DOS for the system represents the probability of a k state lying within an energy range for the entire crystal. In contrast, the partial density of states (PDOS, Q(e)) represents the relative contribution of specific atomic orbitals to the DOS. Clearly, the sum over all PDOS must equal the total DOS and the relative weighting of each contributing atomic orbital to the PDOS is defined as the weighted gross population summed over atomic orbitals χ_u

$$Q_A(e) = \sum_{x_u} q_u(e) \tag{II-26}$$

where

$$q_u(e) = \sum_i g_i(e) q_u(e_i) \tag{II-27}$$

is the gross population of an atomic orbital x_u for each doubly occupied atomic orbital state and $q_u(e)$ is the weighted gross DOS of the x_u.

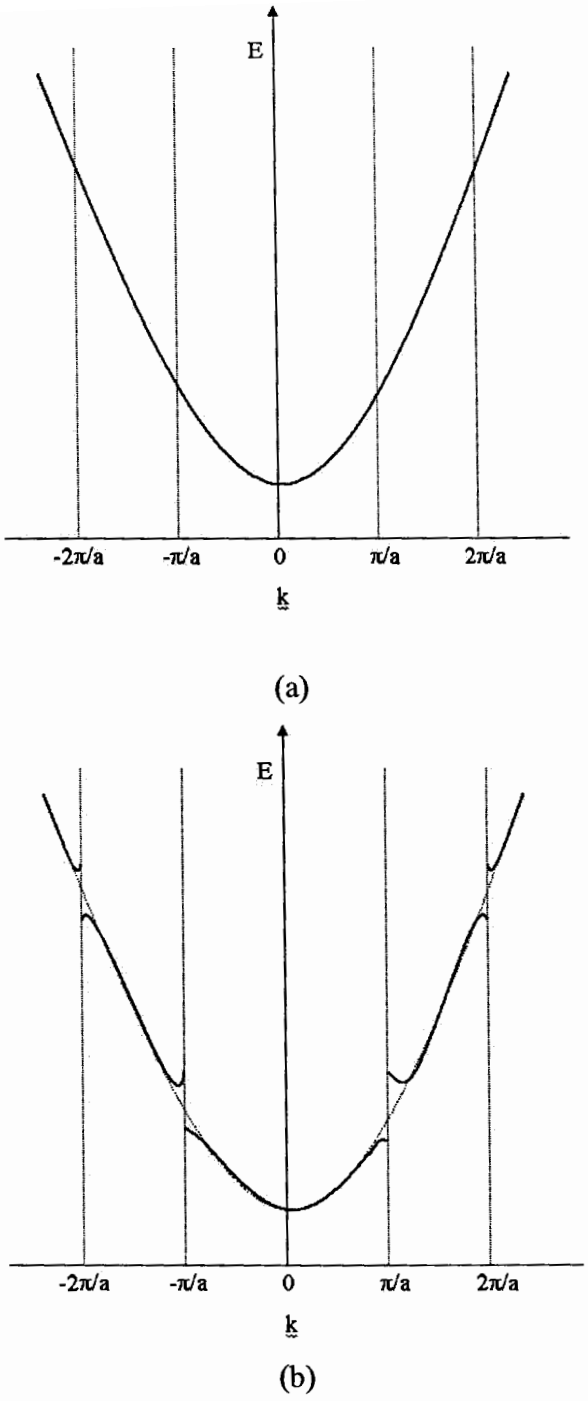

Fig. 16. Energy vs k band diagram of (a) a free electron and (b) a nearly-free electron.

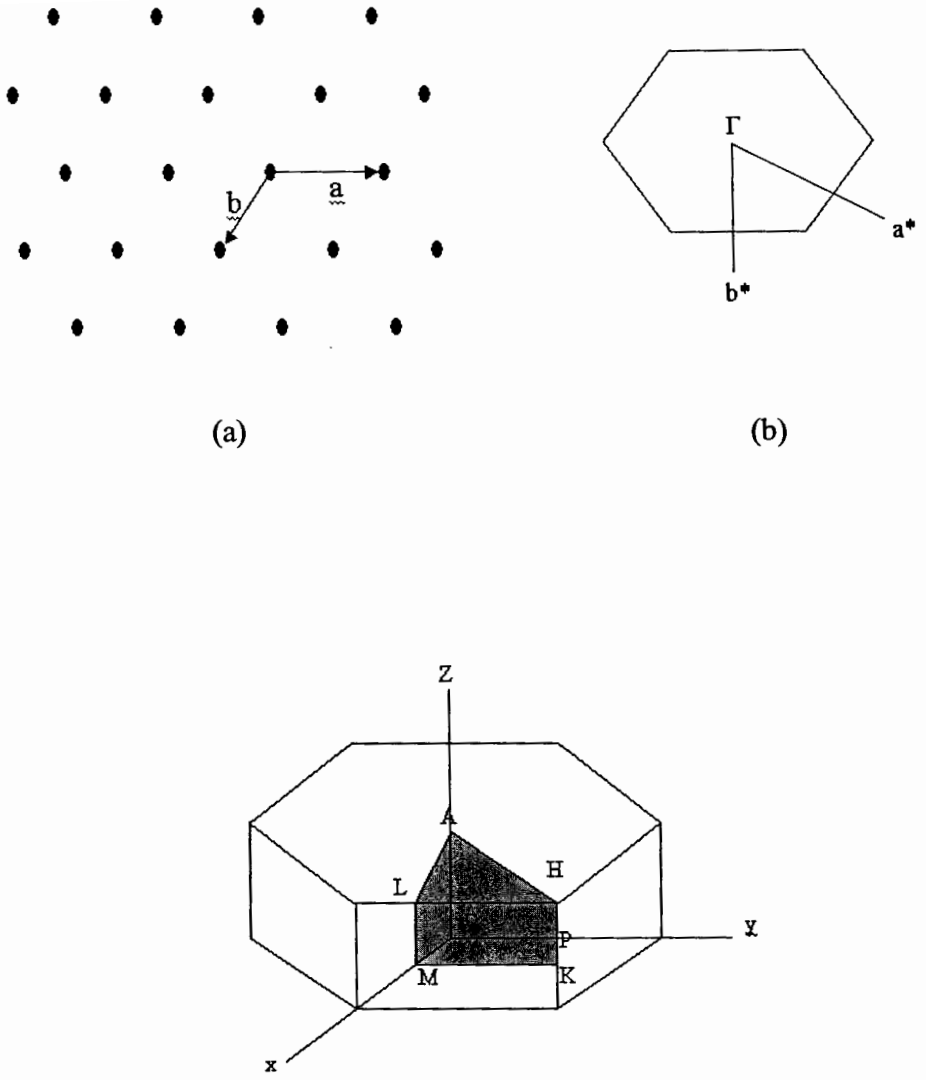

Fig.17. (a) direct lattice in real space and reciprocal lattice in reciprocal space for two dimensional hcp structure. Reciprocal vectors, a* and b* are perpendicular to direct vectors, a and b respectively. (c) reciprocal space of hcp structure with symmetry a lebel.

1.4. STM Image Simulation[108]

Tersoff-Hamann theory[98] provides a theoretical approach to STM image interpretation. STM images are calculated using a 3-step process; after the crystal orbitals Ψ_i and their orbital energies are calculated for surface-projected k-points, the energy levels are selected near the Fermi level, representing the V_{bias} of the measurement. For semiconducting materials, the energy range selected below the Fermi level refer to electron density at the top of the valence band while the energy range selected above the Fermi level refers to the bottom of the conduction band. For metallic samples, the electron density near the Fermi level is plotted. Finally, the DOS for the selected energy range is calculated with respect to the vertical tip position. To calculate the STM images, Tersoff-Hamann treated surface and tip as two separate metal systems with constant separation and approximated the tip as a hydrogen-like S-wavefunction. $\rho(r_o, E)$ is the local density of states at the tip position represented as

$$\rho(r_o, E) = \sum_i |\Psi_i|^2 \delta(E_i - E_f) \qquad \text{(II-28)}$$

where Ψ_i, E_i, and E_f are crystal surface orbital, its orbital energy, and Fermi energy, respectively. The tunneling current is expressed as

$$I_{tun} \propto \int_{E_f}^{E_f+eV} dE \sum_i |\Psi_i|^2 \delta(E_i - E_f) \qquad \text{(II-29)}$$

This theoretical treatment approximates the I_{tun} in STM images as proportional to the local DOS (LDOS) of sample surface localized at the tip position. Thus, this theory indicates that STM images be interpreted as (x-y) maps of the LDOS of the sample surface at a particular height from the surface (z).

2. Density Functional Theory (DFT)

2.1. DFT

The EHTB method provides details of the electronic structures based on a fixed geometric structure and can be used to generate simulated STM images based on that structure, but is not suited to geometry optimizations. In contrast DFT, particularly when implemented in the CASTEP code, [112-114] can be used to relax the structure of bulk solids and surfaces which can then be used for image simulation via the EHTB method. In this project, DFT was used to predict the edge structures of the probe materials by optimizing the crystal structures and provide a determination of the physical properties with respect to the optimized structures.

DFT, developed by Hohenberg and Kohn [115] and by Kohn and Sham,[116] is based on the theorem that the ground-state total energy of a system is a functional of electron density of the system. The functional is expressed in terms of

$$E_0 = E_0[\rho_0] \qquad \text{(II-30)}$$

where square brackets indicate a functional. Hohenberg and Kohn[115] proved that the electronic properties, the electronic states, and the ground-state total energy of system in the external potential are completely determined by electron density (ρ_o). The theorem tells us that the minimum total energy is equivalent to the true ground-state energy. However, the exact functional based on the electron density is not known since the determination of the external potential, which represents the interaction between the electrons and nuclei is not clear. Kohn and Sham[117, 118] improved DFT with the 'concept' of a reference system which consists of non-interacting electrons. In this

system, each electron experiences the average external potential resulting from the other electrons and nuclei in the system rather than interactions between individual electron pairs. The purely n-electronic Hamiltonian is expressed as

$$\hat{H}\Psi_n = \left(-\frac{\eta^2}{2m}\nabla^2 + \hat{V}_{Ne} + \hat{V}_{e-e} \right)\Psi_n = E\Psi_n \qquad \text{(II-31)}$$

where the first term is kinetic energy operator, and V_{Ne} is external nuclei-electron potential, and $V_{e\text{-}e}$ is effective potential representing the average electron-electron interaction potential. The electron density is expressed in terms of n-electron wavefunctions,

$$\rho_0 = \sum_i^n \Psi_i^2 \qquad \text{(II-32)}$$

The energy of the reference system is the sum of 3 terms and is written as

$$E_r = T[\rho_0] + V_{Ne}[\rho_0] + V_{ee}[\rho_0] \qquad \text{(II-33)}$$

The electron density (ρ_0) of the reference system equals to the electron density (ρ_s) of system. When we know the electron density, we can calculate the ground state total energy of system from the electron density (ρ_0). The energy of the system is expressed as

$$E_0 = T[\rho_s] + V_{Ne}[\rho_s] + V_{ee}[\rho_s] \qquad \text{(II-34)}$$

The external potential $V_{Ne}[\rho_s]$ is determined from the electron-nuclei separation and is known from treatment of one-electron systems. However, $T[\rho_s]$ and $V_{ee}[\rho_s]$ are not known. The ground-state total energy of the system is determined by comparing the system with the reference system and is expressed as

$$E_0 = -\frac{1}{2}\sum_{i=1}^{n}\left\langle \Psi_i^{ks}(1)\middle|\nabla_1^2\middle|\Psi_i^{ks}(1)\right\rangle + \int \rho_0(r)V(r)dr + \frac{1}{2}\iint \frac{\rho(r_1)\rho(r_2)}{r_{12}}dr_1dr_2 + E_{xc}[\rho_0] \qquad \text{(II-35)}$$

where the first term in the right is the electronic kinetic-energy, the second is the nuclei-electron interaction potential-energy, the third term is the classical electrostatic electron-electron repulsion-energy, and the last is the exchange-correlation energy functional. This last term accounts for exchange antisymmetry and correlation energy of fermions as is purely quantum mechanical in origin. The ground-state total energy is determined by the variation of the Kohn-Sham wavefunctions from which the electron density is determined. The minimum energy is found for the Kohn-Sham wavefunctions using a self-consistent procedure applied to the variational theorem (eq. II-12) and satisfies the following equation

$$\left[-\frac{1}{2}\nabla_1^2 - \sum_{\alpha}\frac{Z_\alpha}{r_{1\alpha}} + \int \frac{\rho(r_2)}{r_{12}}dr_2 + V_{xc}(1)\right]\Psi_{ks}(1) = E_0\Psi_{ks}(1) \qquad \text{(II-36)}$$

where Greek letters refer to nuclei, Roman numbers refer to electrons and Ψ_{ks} are the Kohn-Sham wavefunctions. The exchange-correlation potential (Vxc) is defined as

$$v_{xc}(r) = \frac{dE_{xc}[\rho(r)]}{d\rho(r)} \qquad \text{(II-37)}$$

Although the Kohn-Sham equations are an exact solution of an interacting multi-electron system, the nature of the exchange-correlation energy (v_{xc}) is still an active area of research. Currently, the v_{xc} is defined by approximate functional as described below.

2.2. Exchange-Correlation Potential

The first approximation used to describe the v_{xc} was introduced by Hohenberg and Kohn and called the Local Density Approximation (LDA). [112, 119] This approximation

is based on the variation of electron density in a homogeneous electron gas and is defined as

$$E_{xc}^{LDA}[\rho] = \int \rho(r)\varepsilon_{xc}[\rho]dr \qquad \text{(II-38)}$$

where $\epsilon_{xc}[\rho]$ is the exchange-correlation energy per electron in a system with the electron density ρ. The exchange-correlation potential (Vxc) is defined by taking the derivative of functional with respect to electron density ρ.

$$V_{xc}^{LDA} = \frac{dE_{xc}^{LDA}}{d\rho} \qquad \text{(II-39)}$$

Within the LDA framework, the electron gas is represented as electrons uniformly surrounded in a continuous and uniformly positive charge composed of the nuclei and the remainder of the electrons.

The LDA method requires that the electron density varies slowly and the variation of electron density is described as a slightly perturbed electron gas. Because of this requirement, the LDA has a drawback in that it cannot model realistic systems that are not homogeneous or do not have only slowly varying electron density. This shortcoming is partially overcome by adding a density gradient. This more accurate Vxc expression is the called the Generalized-Gradient Approximation (GGA). The E_{xc} in the GGA is expressed as

$$E_{xc}^{GGA}[\rho^{\alpha}, \rho^{\beta}] = \int \rho(r)\varepsilon_{xc}^{LDA} f(\rho^{\alpha}(r), \rho^{\beta}(r), \nabla\rho^{\alpha}(r), \nabla\rho^{\beta}(r))dr \qquad \text{(II-40)}$$

where ρ^{α}, ρ^{β}, $\nabla\rho^{\alpha}$, and $\nabla\rho^{\beta}$ are densities and gradients of α and β spins, respectively and f is a function of both densities and gradients of spins. The GGA have been improved since its introduction in the 1980s. The form of the GGA used in this project

is from Perdew and Wang (PW-91), [120, 121] and Perdew, Burke and Ernzerhof (PBE).[122] Kohan and Sham proposed that the second-order gradient expansion approximation (GEA), in which the density gradient is expanded to higher order terms, offers some improvement to the LDA.[123] However, the GEA has the drawback that its exchange-correlation is a truncated expansion, so exchange-correlation is not exactly obtained. To overcome this, the exchange-correlation of GGA-PW 91 was written with a sharp cutoff which terminates the exchange-correlation of the GEA at a particular energy.

2.3. Plane Wave Basis Set and Pseudopotentials

The infinite number of electrons in the crystal is treated by expanding plane wave basis set in the k-space of unit cell as described in equations II-9 and II-10. The electrons are highly localized in closed atomic (core) shells near the nuclei and exhibit the strong wave oscillations in the core region. The core electrons are not sensitive to the chemical reactivity and so the core region is simplified by the treatment of wavefunction by replacing the strong ionic potential in the core region by the weak pseudopotential. As shown in the Fig. 18, the wavefunctions and their potentials are illustrated. The use of pseudopotentials to treat the core electron shell offers a considerable reduction in complexity since the sharply varying electronic density, which would require a large number of basis set wavefunctions to adequately represent, is replaced by a more smoothly varying pseudopotential. The available pseudopotentials are described by the degree of "softness" referring to the smoothness of the density variation. The pseudopotentials used in this work was the ultrasoft pseudopotential (USP) introduced by Vanderbilt.[124, 125]

2.4. Geometry Optimization

Geometry optimization or, equivalently, energy minimization is a method used to find the atomic or crystal configurations that represent equilibrium states on the potential energy surface (PES). The optimization finds a minimum energy in the PES by systematically varying the atomic coordinates and unit cell parameters until the forces on each atom are minimized. There are several parameters used to determine when the system has reached equilibrium. These convergence criteria include total energy, maximum displacement in successive optimization steps and total force on the atoms. The system reaches convergence by defining a maximum allowable value for each of the convergence criteria. To prevent a "runaway" calculation, a maximum number of optimization steps is also defined. In general, the number of parameters that must be satisfied for an N atom system increases as $N^2/2 - N$. This relation results from their being N^2 pair interactions of which half are repeats of the other half. In addition, N of the interactions are self interactions and are excluded from the total. This large number of parameters can lead to large computational times for large systems. Many algorithms have been developed which offer an alternative to conventional matrix diagonalization that improve the efficiency of the optimization. One of the methods that reduces computing time without lowering the accuracy of the optimization is the quasi-Newton-Raphson method. A key difficulty in optimization is the generation and manipulation of a Hessian matrix which contains the second derivatives of the forces. The Hessian must be repeatedly manipulated such that the terms in the matrix approach zero. An approximation used to simplify the manipulation of the Hessian is the Broyden-

Fletcher-Goldfarb-Shanno (BFGS) algorithm.[126] In the BGFS methods, the Hessian is initially approximated using Hessians from previous iterations and then updated from the current iteration, thus avoiding the requirement to generate a new Hessian for each iteration. This method significantly reduces the time required for the Hessian to reach zero. The updating method can also reduce the data storage size to store the Kohn-Sham Hamilitonian.

2.5. Computational Methods (CASTEP and Dmol^3) for Optimization

The geometry optimization was performed using the ab initio quantum mechanical packages CASTEP (Cambridge Sequential Total Energy Package) and Dmol^3 (Densityfunctional theory applied to MOLecules), [127, 128] both available commercially from Accelrys™ [129]. CASTEP is based on the pesudopotential plane wave basis set in the either internal or Cartesian coordinates and can calculate the total electronic energy of system with respect to geometry and the exchange-correlation in the electron-electron system with respect to geometry and the exchange-correlation in the interaction with LDA and GGA. The geometry optimization is obtained using the BFGS optimizer on both the internal atomic coordinates and the unit cell so that each can be optimized.

The Dmol^3 package is based on the linear combination of localized atomic orbitals. Dmol^3 was originally designed for optimizing molecules and has been extended to calculate crystalline materials. In Dmol^3, the basis set is obtained by using localized numerical atomic orbitals with an improved minimal basis. This method effectively doubles the basis set, similar to that used in Gaussian double-zeta (DZ) sets. The set parameterizes the variation of the atomic size and electronic polarization so that

distortion in the shape and the charge density of the atomic orbital is redistributed between atomic orbitals. The ion core is treated by two ways; the all-electron DFT method, and the pseudopotential approximation. The all-electron treatment has a high computational cost and complexity in treating the core region. Therefore, the pseudopotential method is commonly used and provides well-validated results. The combination of the expanded atomic orbital basis sets and use of a pseudopotential reduces the matrix size, so that geometry optimization by using this combination in the Dmol^3 package is faster than the plane-wave based methods in CASTEP. In this work, both the CASTEP and Dmol^3 methods were used for optimizations of crystals and molecular systems, depending on the properties sought and the system complexity.

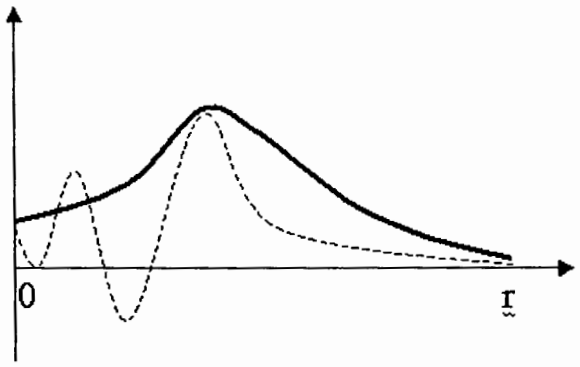

(a)

(b)

Fig. 18. Representations of pseudo (solid line) and true electron (dotted line) (a) wavefunctions and (b) potentials.

III. Methodology

A. Experimental

1. STM Studies of Bulk LTMCs

The basal planes of bulk LTMCs at atomic resolution were probed by using a commercial instrument supplied by Park Scientific Instruments STM. The STM was operated at ambient condition (room temperature and 1 atm air pressure). The LTMC samples were mounted on a conductive disk with Ag epoxy glue and clean surfaces were obtained by cleaving the topmost layers using adhesive tape. Large protrusions and fragments on the surface of the LTMCs are also removed to prevent the mechanical contact with tip that would result in tip crashes or in low-resolution STM images. Probing tip was prepared by mechanically cutting a Pt/Ir (80/20) wire with a pair of sharp scissors. Each tip wire was about 2.5 cm in length. The apex roughness of sharpened tips was checked by scanning a highly oriented pyrolytic graphite (HOPG) surface and checking for atomic resolution. Graphite was used as a calibration standard. Whiskers on the apex of the tip can cause multi-tip effects on the STM image which appear as "ghost" images. Such features are difficult to prevent but often do not interfere with image interpretation.

The STM images of LTMCs were recorded in constant current mode with the bias applied to provide either sample-to-tip or tip-to-sample tunneling. In principle, constant current imaging mode has an advantage over constant height mode in that it provides higher resolution but takes longer scanning times than constant height mode. Moreover, constant height mode provides better vertical resolution since the tip height is not changed during scanning. A common difficulty in atomic resolution imaging results

from thermal drift of the sample and piezocreep. These problems result in distortions of the crystal lattice in the image data. Thermal drift occurs when the sample temperature is changing over time and can be minimized by waiting for the instrument and sample to achieve thermal equilibrium. Piezocreep results from the piezoscanner drifting position over time until it reaches an equilibrium state at a particular applied voltage. This effect is also reduced by allowing the scanner to stabilize. The surface of the LTMC samples were probed at least 30 min to minimize the thermal drift and piezocreep while probing the surface. As with any microscopic measurement, a single image may not be representative of the surface. Consequently, a large number of images were collected for each sample and then averaged to find reliable lattice constants. STM images were filtered by using the 2-dimensional Fast Fourier Transform (2DFFT) method to reduce noise artifacts.

2. STM Studies of LTMC Step Edges

Defects such as point defects, and step edges were found to exist on the LTMC crystal surfaces. Defects are of greater interest than perfect crystal lattices since these are assumed to be catalytically active. The catalytic activity is enhanced by redistributing the electronic states near the Fermi level and introducing extra states that function as chemical binging sites for reactants. The surfaces of the LTMCs were initially probed over a large scan area (1-3 μm^2) at a slow scan rate to find defects. It was difficult to find defects on the surface since defects are positioned on the surface randomly.

In order to improve the likelihood of finding a defect state, we applied two methods to deliberately create defects; ultrasonication and gap resistance control. In

principle, ultrasound is a mechanical wave with frequency above 20 kHz and can disrupt the crystal surface by causing shock waves that break apart the crystal surface.[130-133] The shock waves are produced by the implosion of a micelle generated in a polar solvent. To implement this procedure for the probe materials, a small LTMC crystal was cleaved by adhesive tape and placed in acetonitrile or N-methylformamide (NMF) solvent. A series of samples were prepared by ultrasonicating the solvent and crystal by increasing the sonication time 10 second per sample. Sonicated samples were then dried in air. Another method is to decrease the tunneling gap resistance between the tip and sample. In so doing, the electric field below the tip is increased until the surface is disrupted thus forming defects in the surface.[134, 135] The gap resistance can be changed by increasing the tunneling current set-point which drives the tip closer to the surface.

3. STM Studies of Nanostructured LTMCs

3.1. Substrates

STM provides an opportunity to probe the basal plane of bulk materials and also nanostructured materials. STM studies of nanostructured LTMCs require that the nanoparticles lay on a suitable substrate that is easy to clean and has an atomically flat surface. If substrate contains irregular surface features, it is difficulty to find the deposited nanostructured sample on the substrate surface. In addition, it is even possible that the presence of gases such as H_2, O_2, H_2O and hydrocarbons on the substrate surface under ambient conditions can influence the interaction between the tip and the sample.[136, 137]

The graphite basal plane is chemically inert and conductive making it well suited

as a substrate for imaging nanostructured particles.[138-140] Graphite crystallizes in the hexagonal $P6_3/mmc$ space group in which the basal planes, like LTMCs, are separated by van der Waals layers. LTMCs are also suitable substrates since these satisfy the requirement for STM study that the surface must be chemically inert, atomically flat and conductive.

Despite graphite and LTMCs providing a flat conductive surface, surface defects such as irregular, rough holes, step edges, and crystal fragments can occur.[141] It is possible that the local structural properties of these defects may affect the tip-sample interaction while imaging nanoparticles if such substrate defects are nearby even though the bulk basal plane of the substrates are chemically inert. The main problem with the presence of these local defects in the substrate are that they can be difficult to distinguish from the nanostructured LTMCs. This problem is overcome by averaging over large sample sets and eliminating those images which are suspect by virtue of their low representation in the set.

3.2. Nanostructured Sample Preparation

Nanostructured LTMCs were prepared by fragmentation of bulk LTMC crystals in a ultrasonic bath containing either acetonitrile or NMF (similar to the method described above for deliberatively roughening the surface). The process was believed to work by the action of the energy released accompanying the implosion of a solvent cavity in the ultrasonic bath.[142] To prepare nanostructured materials, the sonication time was increased to hours – days. Impurities on the surface of the solid crystal was removed by ultrasonicating for 10 min and decanting the colloid dispersion. The sonicated crystal was rinsed several times with solvent and then was resonicated for 2-3 days until a

stable colloid dispersion was formed. The fractions of particles that are not dissociated were centrifuged out. The nanostructured particles formed using this method are stable colloidal suspensions as they remain in suspension for several months following preparation.

In an extension of the studies of clean, as-prepared nanoparticle edges, we also investigated the effects of edge association with sulfur containing molecules. The goal of this portion of the study is to see if methods could be developed to passivate the edge states of the nanoparticle. Nanostructured LTMCs were prepared by ultrasonication (as above) while adding 5, 10, and 20 μl of dodecanethiol, $C_{12}H_{25}SH$ and octanethiol $C_8H_{17}SH$ into the each of test tubes, which contained 0.01g of LTMC crystals with solvents. The nanoparticles prepared using this method were also stable suspensions but over a shorter period of time, indicating that the edges may be passivated but that the materials are less stable in polar solvents because of the presence of the organic moiety on the edge instead of the more polar MS_x edge states. The effect of thiol chain length on passivation was also studied using tetrahydrothiol and octanethiol, prepared in the same way.

3.3. STM studies

The suspended nanoparticle LTMCs in solvent were deposited onto graphite or bulk LTMC substrates. Control samples were prepared by depositing cleansolvent on the substrates and imaged. The colloidal samples were mounted on a substrate by placing 5-10 μl of colloid and allowing the solvent to evaporate. STM images were collected under ambient conditions at room temperature. Since the LTMCs studied range in conductivity from semi-metallic to semiconducting, a range of bias voltages

was used for the group of LTMC nanoparticles. Negative bias voltages were applied to the sample with respect to the tip and tunneling currents were typically 2-5 nA with the STM operating in constant current mode. A large area (3 μm x 3μm) was scanned to find nanoparticles and then was reduced gradually to a smaller area sufficient to measure the atomic corrugation.

B. Computational

1. Bulk LTMCs

Bulk LTMC crystal models were constructed by using the known crystal structures and their parameters in table 2. The model structures were built on bulk unit cell structures. For example, the bulk unit cell of MoS_2 consists of two S-Mo-S trilayers and crystallizes in the P63/mmc spacing group. The fractional coordinates of the atomic positions in the unit cell are; one Mo atom positioned with fractional coordinates (0.3333, 0.6667, 0.7500) and one Sulfur atom positioned with fractional coordinates (0.6667, 0.3333, 0.6210). The other atoms in the unit cell are replicated by symmetry. This crystal system is represented by a Mo atom placed at the center of a right trigonal prism. In NbS_2, the coordination of the atomic positions is different from the coordination of MoS_2. The Nb atom is positioned with coordinates (0. 0000, 0.0000, 0.75) and the sulfur atom is coordinated at (0.3333, 0.6667, 0.621). For ReS_2, which crystallizes in the low symmetry P-1 space group has more unique atoms in the unit cell and is described in Table 2. In this structure, the Re atoms occupy the center of a distorted octahedron. The unit cell of the LTMCSs investigated in this study are illustrated in Fig. 2 and 3b.

Geometry optimization of the TMCs was performed with the CASTEP density

functional code, which can relax both the unit cell and internal atomic coordinates. We used the GGA-PW91 and GGA-PBE functionals for exchange and correlation and USP for electron-ion interactions. The energy cutoff used was from 290 eV to 500 eV.

Electronic band structures and their corresponding DOS were obtained using the CAESAR EHTB code with the CASTEP-optimized structures. The band structure dispersion curves for the LTMCs in the first Brillouin zone (BZ) of the hexagonal lattice are shown in Fig.17. We considered the energy band structures along directions $\Gamma \rightarrow K \rightarrow M \rightarrow \Gamma$ corresponding to k points (0.0.0) → (0.5, 0, 0) → (0.333, 0.333, 0) → (0, 0, 0).

STM images of bulk LTMC were simulated by using Tersoff and Hamann theory. The electronic structures were calculated on a given crystal structure by applying a double-zeta basis set. We calculated the local electron density for negative bias voltage STM images in the energy range near the Fermi level.

2. Step Edges and Nanoparticle $LTMC_S$

STM data of LTMC edge focuses on the step edge of bulk materials, and edge effects associated with nanoparticle LTMCs. The approach taken here is to model these edges as 'ribbon' structures. This approach has been successfully used in investigating the edge properties of graphite.[143] Based on the experimental STM results that indicate that different edge patterns may exist, we also modeled several edge terminations in the ribbon structures. For example, the STM images of nanostructured MoS_2 on graphite exhibit a novel superstructure near the edge termination and a normal lattice pattern at distances greater that 2 – 3 nm from the edge.[144] This superstructure might be caused

relaxation of the surface energy resulting from cleavage. However, the surface termination is not clearly defined, consequently we proposed 3 types of edges defined as a sulfur edge ($\bar{1}010$), metal edge ($10\bar{1}0$), and sulfur-metal mixed edge ($11\bar{2}0$). By comparing simulated STM images generated for each of these structures with experimental data, the chemical and geometrical composition of the edge can be investigated.

In addition, the edge structure of NbS_2 was investigated for step edges on the bulk material. As in the case of MoS_2 nanoparticles, the chemical and geometrical composition of the NbS_2 edge is also not clearly understood.

In both cases of MoS_2 and NbS_2, model edge structures were prepared which were composed of "ribbons" such that a layer of each material was prepared having a defined width and infinite length. The width of the ribbons was determined on that required to accommodate the edge layer effects observed in the experimental data but not so wide as to be unfeasible in terms of computational demand. The ribbon models were constructed by first reorienting the hexagonal unit cell to a $(1x\sqrt{3})$R 30 orthorhombic unit cell in Fig. 19. The ribbons were then constructed by expanding the reoriented cell along the a or b vector depending on the type of edge termination desired (Fig. 20). The formation of a ribbon was accomplished by removing several unit cells at the ends of the expanded cell to approximate the vacuum region at the ends of the ribbon (Fig. 20 b). The ribbon models used in this study had 1.2 nm vacuum regions between adjacent ribbons. In these models, there exist two edges instead of one as in actual step edges. To approximate one of the edges as the bulk structure, simulations were run in

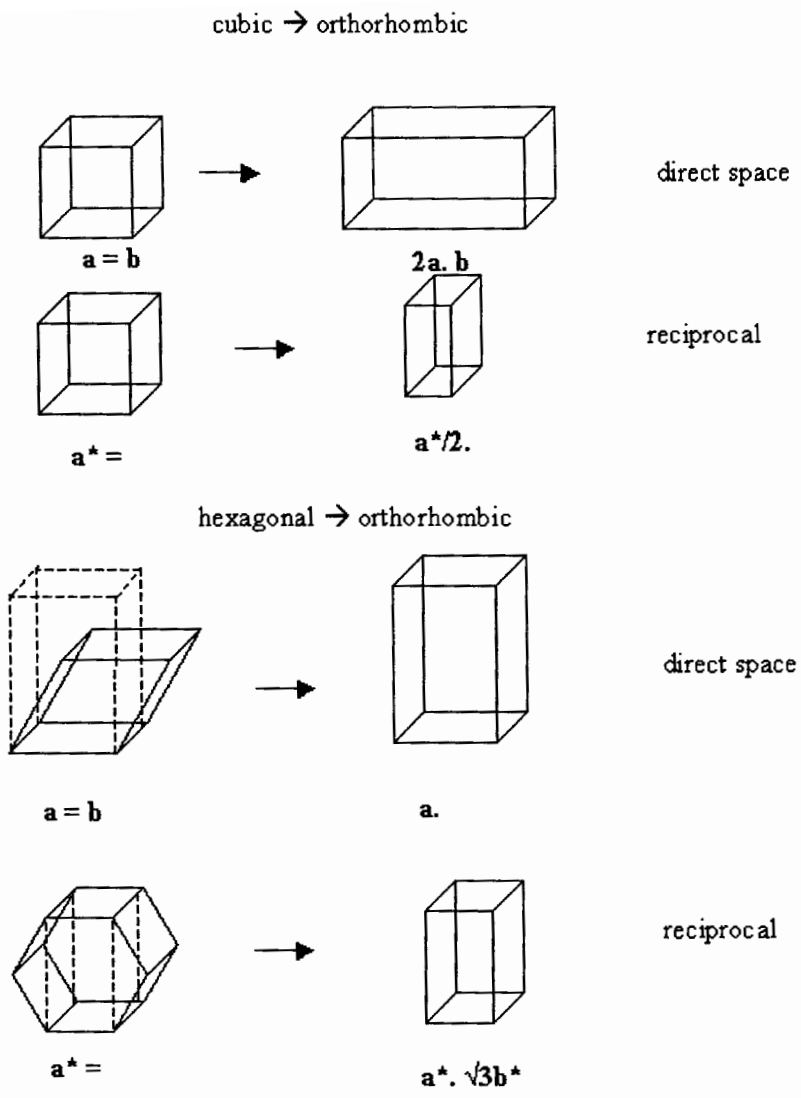

Fig.19. Brillouin Zone folding scheme.

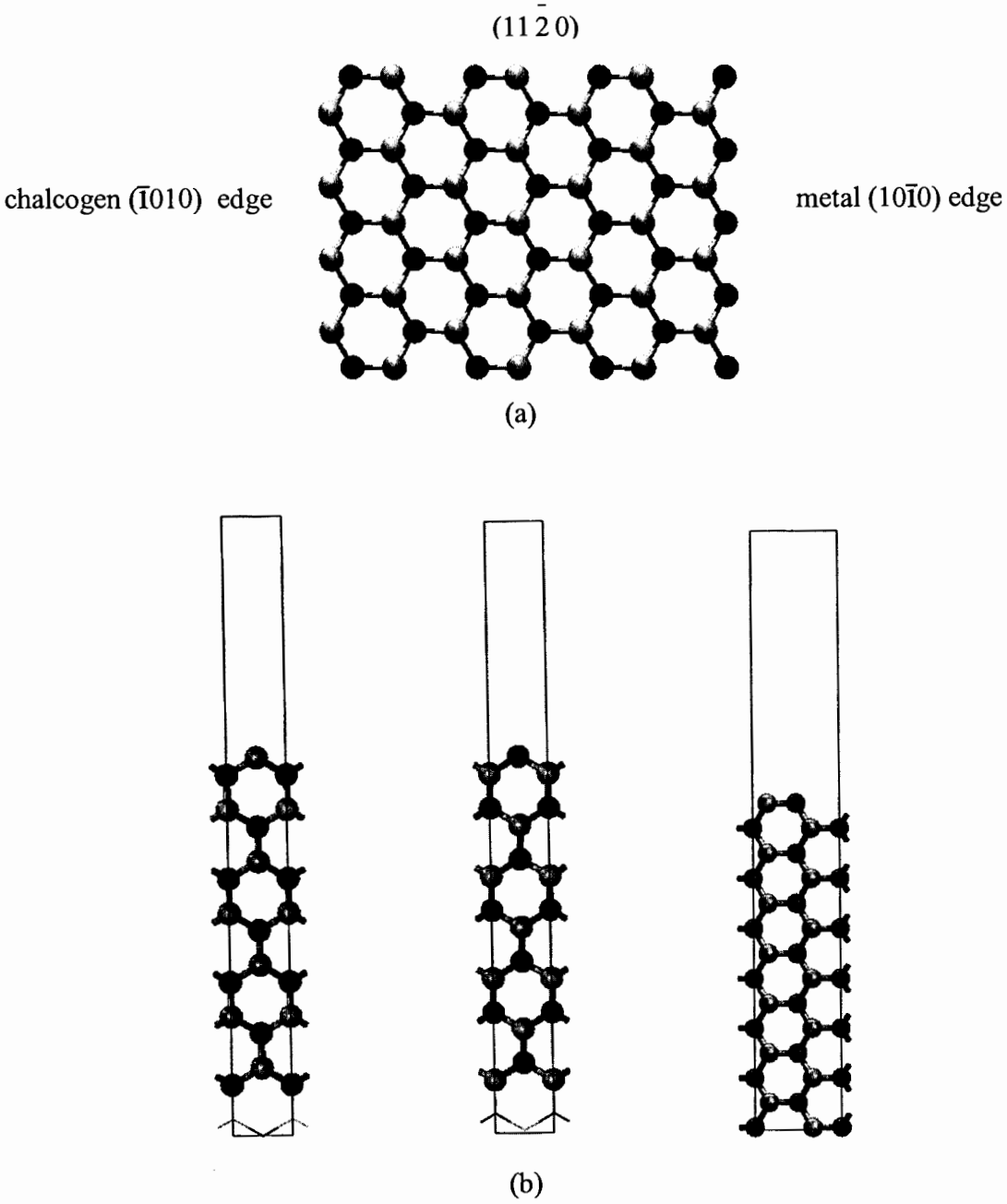

Fig. 20. (a) Representations of creation of edges cutting planes and of edges: the metal [10$\bar{1}$0] edge, the chalcogen [$\bar{1}$010] edge and metal-chalcogen mixing [11$\bar{2}$0] edge. The formation of a ribbon was accomplished by removing several unit cells at the ends of the expanded cell to approximate the vacuum region at the ends of the ribbon. (b) The ribbon models used in this study had had 1.2 nm vacuum regions between adjacent ribbons.

which the unit cells at one of the ribbon ends were constrained from relaxing from the bulk coordination geometry. The fractional coordinates of the atomic structure on which the ribbons were constructed were based on previously optimized bulk structures using CASTEP. Unless the stresses in the bulk unit cell are relaxed prior to ribbon construction, the reliability of constraining the "bulk" side of the ribbon would be compromised.

The chemical composition of the ribbon edges were also varied by removing particular atoms at each edge type. The edge-most metal atom on the $(\bar{1}\,010)$ sulfur edges were constructed with 0-fold (Fig. 21 a) and 1-fold (Fig. 21b) coordinative unsaturation. The edge-most metal atom on the $(10\bar{1}\,0)$ metal edge were constructed with 4 to 6 coordinatively sulfur saturated coverages (Fig 21a, b, and c, respectively). These terminations represent the most likely configurations for the low Miller index edges as observed in the experimental data. Since we did not observe higher Miller index edges (e.g., $(23\,\bar{5}\,0)$), we did not include these in our study. We did include sulfur-transition metal mixed edge $(11\,\bar{2}\,0)$. In this case, both edges of this ribbon structure are the same type (neither can be referred to as "metal" or "sulfur") in Fig. 22. The optimizations of both MoS_2 and NbS_2 LTMCs ribbons were performed with CASTEP. We used the GGA-PW91 pseudopotential for the exchange and correlation and the USP for electron-ion interactions. The BFGS updating algorithm was used for all geometry optimizations.

The electronic properties were investigated by calculating the band dispersion

chalcogen [$\bar{1}$010] edge 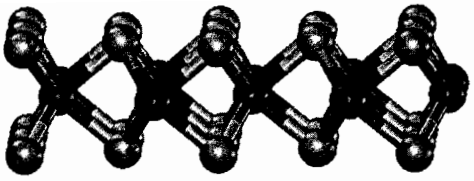 metal [10$\bar{1}$0] edge

(a)

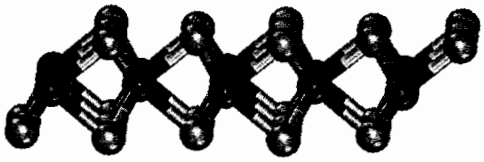

(b)

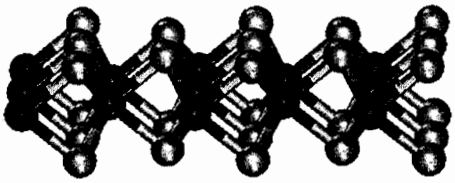

(c)

Fig.21. Representations of metal [10$\bar{1}$0] edge and the chalcogen [$\bar{1}$010] edge configurations. On the metal [10$\bar{1}$0] edge, (a) zero sulfur atom, (b) one sulfur atom, and (c) two sulfur atoms are coordinated on metal atom in one unit cell. These sulfur coverages are represented as (a) 4-fold, (b) 5-fold, and (c) 6-fold sulfur saturated edges. On the sulfur ($\bar{1}$ 010) edge, the sulfur coverages at edges are represented as (a) 6-fold, (b) 5 fold, and (c) 4-fold sulfur saturated edges.

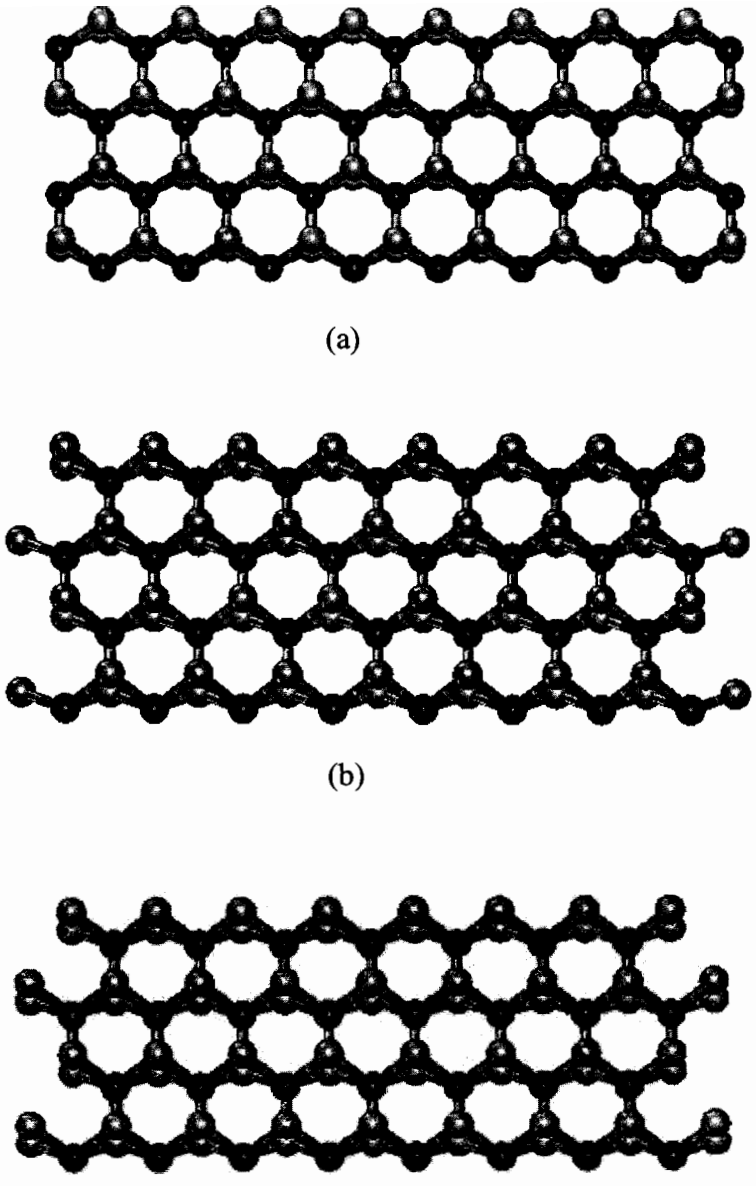

Fig. 22. Representation of [11$\bar{2}$0] edge configurations. Edge terminations are leveled as (a) 4-fold, (b) 5-fold, and (c) 6-fold sulfur saturated edges.

curves, DOS, and PDOS for each system. As in the case of bulk materials, the band structure of the ribbons is represented in a reciprocal space Brillouin Zone (BZ). For ribbon structures, the effects of zone folding can be used to simplify the analysis. Zone-folding can be viewed as a reduction in the reciprocal space cell caused by the corresponding expansion of the direct space unit cell. For example, if one extends a cubic unit cell by doubling the lattice vector along **a**, the reciprocal space unit cell is reduced by 1/2 along **a***. Likewise, reorienting a hexagonal unit cell to $(1x\sqrt{3})$ causes the BZ to "fold" along the (a*,b*) direction to form an orthorhombic BZ. The zone folding scheme is depicted in Fig. 19 for the cubic and hexagonal systems. Any band structure in the folded part of the original BZ is also folded into the resulting BZ. By extension, the ribbon BZs can be viewed as folded by X x $\sqrt{3}$ where X is the number of extension cells along the width of the ribbon. Since the band structure is likewise folded, this makes the resulting band structures exceedingly complicated. Moreover, the band structure corresponding to the width dimension no longer has the symmetry of the original unit cell. The inherent loss of symmetry results in each band in the original BZ to split into a series of new bands, one for each cell expansion in direct space. Fig. 23 depicts the BZ for the ribbon structures in this study. In these BZ structures, the Γ → a or Γ → b direction corresponds to dispersion along the ribbon width depending on the type of ribbon construction. STM images for the ribbon edge structures were simulated using the same method as described under the section above for bulk LTMCs. The V_{bias} energy ranges were selected to match those used in the experiment STM image data.

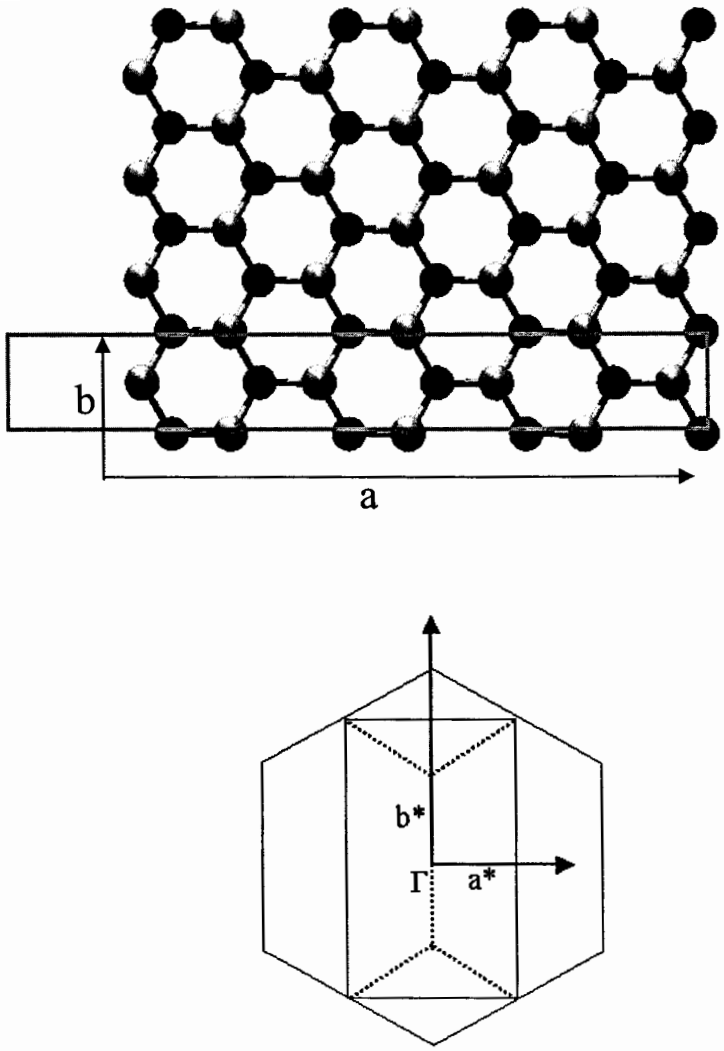

Fig. 23. The BZ for the ribbon structures: (a) Unit cell in real space indicated by rectangle (b) in reciprocal space. The rectangle in Fig. b. represents the BZ folding. The $\Gamma \rightarrow$ a or $\Gamma \rightarrow$ b direction corresponds to dispersion along the ribbon width depending on the type of ribbon construction.

3. Simulating Studies of HDS on Edge Surface

The adsorption of thiophene on the MoS_2 cluster was investigated in order to better understand to the mechanism of the HDS reaction. We first used the optimized edge structures with the sulfur-vacancies on the $(10\bar{1}0)$ Mo edges and on the mixed Mo-sulfur edge. The models for the catalytically active surfaces with thiophene are shown in Fig 24 and 25.

All total energy calculations were performed with Dmol[3]. The GGA-PW91 pseudopotential was used for the exchange correlation. The doubled numerical d-polarizations (DND) and semilocal pseupotential were used as basis set. We restricted each basis function to the 5.4 Å of cuoff radius (R_{cut}) to reduce the computational cost. The optimized structures were then analyzed for optimum geometry of the adsorbate, adsorption site specificity, and adsorption energy using the total energy of adsorption. The energy of adsorption was calculated using the following relation.

$$E_{ads} = E_{LTMC} - (E_{clean} + E_{RS}) \qquad \text{(III-1)}$$

where E_{LTMC} is the total energy of the LTMC with thiophene adsorbate, E_{clean} is the total energy of the clean LTMC ribbon, and E_{RS} is the total energy of the thiophene molecule. This approach has been used successfully for a number of adsorption studies of molecular species on surfaces.

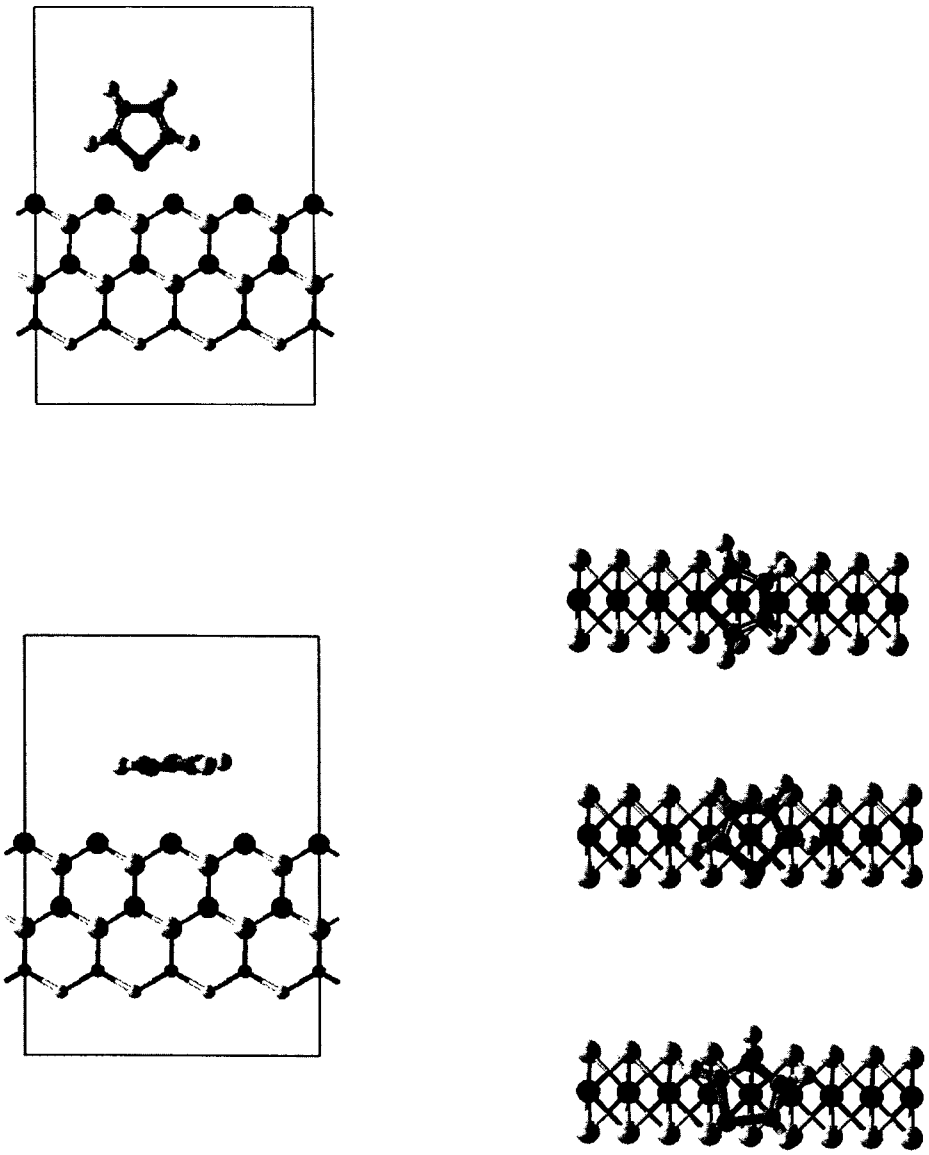

Fig. 24. The adsorption geometries of thiophene on the $(10\bar{1}\,0)$ edge of MoS_2.

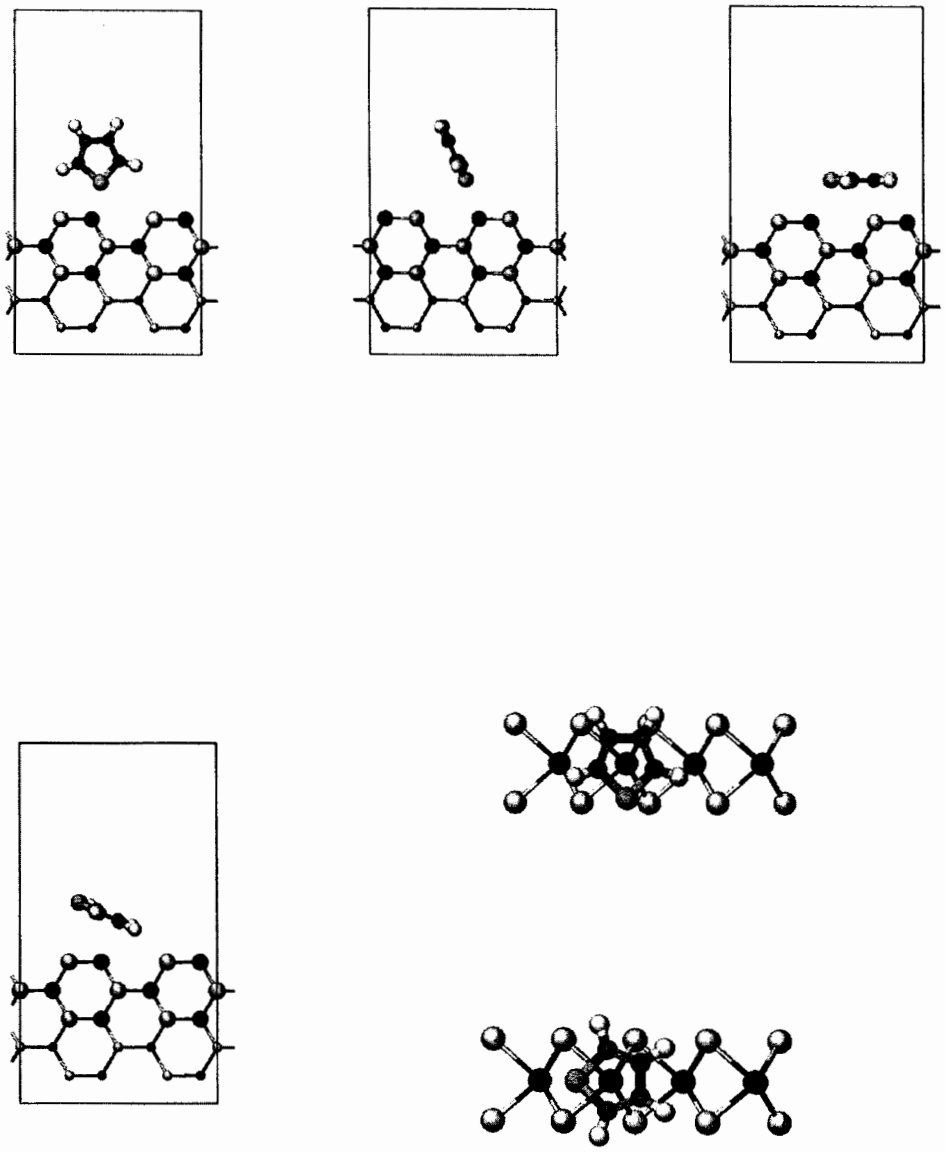

Fig. 25. The adsorption geometries of thiophene on the $(11\bar{2}0)$ edge of MoS_2.

IV. Results and Discussion

A. Experimental

1. STM Studies of Bulk LTMCs

STM studies of the bulk surface of LTMCs provide a basis to validate the results of further investigations of edge and defect states of these materials. Consequently, in this section are discussed the results of defect-free basal plane STM investigations. NbX_2, TaX_2 and MoX_2, where x = S, or Se, were imaged on the top (0001) basal plane. All of these materials have hexagonal symmetry in the basal plane and crystallize in the $P6_3/mmc$. Fig. 26 shows STM images of the NbS_2 and MoS_2 (0001) basal plane respectively and are typical of several dozen atomic resolution images of these materials recorded for this project. The expected hexagonal symmetry of the high-electron density (HED) spot pattern is clearly evident in these images. Moreover the observed basal-plane lattice constants (a = b) are consistent with X-ray diffraction (XRD) refinements for these materials (Table I). In Table II, the observed lattice constants of $NbSe_2$, TaS_2, $TaSe_2$, and $MoSe_2$, which are consistent with published XRD data are also listed.

The HED pattern in LTMCs has been shown to correspond to the top chalcogen atomic layer rather than the metallic layer despite the Fermi level crystal orbitals being comprised mainly of metal d character.[8, 9] This phenomenon is due to the closer proximity of the chalcogen atoms to the STM tip compared to the metal atoms. This interpretation is supported by the probing the ReS_2 basal plane in which the sulfur layers are not coplanar.[145, 146] Fig. 27 shows an STM image of the ReS_2 (0001) basal plane. ReS_2 crystallizes in the $P\bar{1}$ space group and although the overall lattice symmetry is nearly hexagonal (gamma = 119.06°), the unit cell motif exhibits

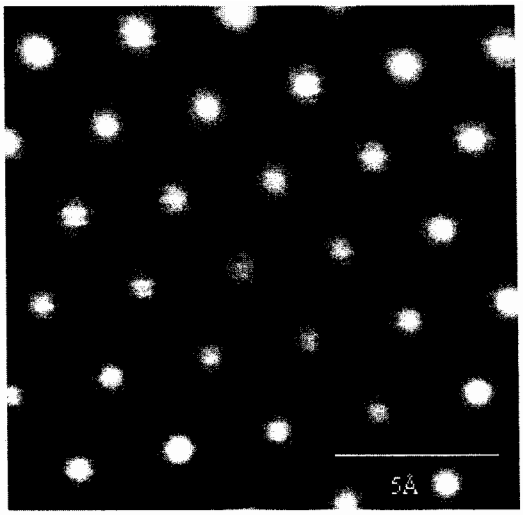

(a)

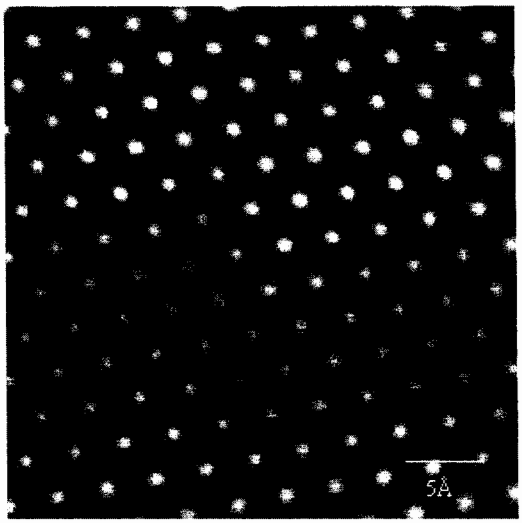

(b)

Fig. 26. STM images of (a) bulk NbS_2 with I_{tun} = 2.5 nA and V_{bias} = 0.025 V and (b) bulk MoS_2 with I_{tun} = 3 nA and V_{bias} = 0.7 V

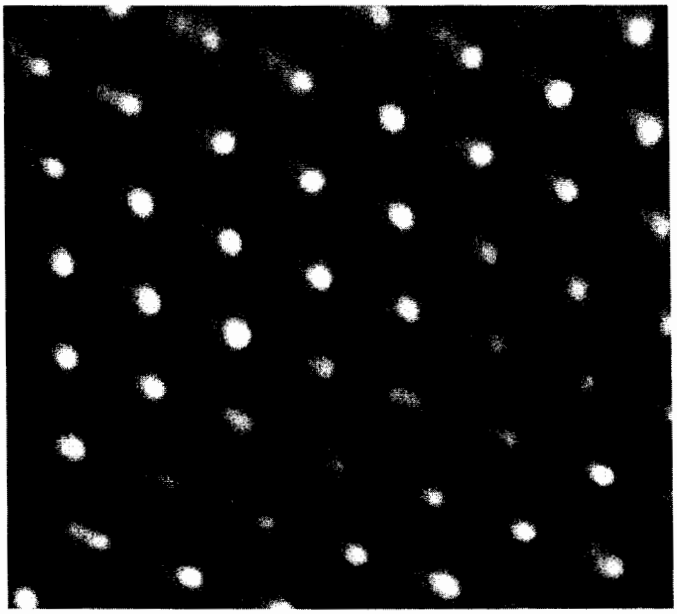

(a)

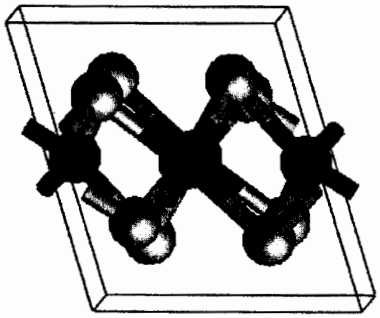

(b)

Fig. 27. STM image of bulk ReS_2 with I_{tun} = 3 nA and V_{bias} = 0.7 V and Schemtic representation of ReS_2.

four distinct sulfur atom coordination sites per layer as represented in Fig. 27. The four distinct sulfur atomic sites make up a diamond pattern having the different intensity of HED spots. By including the electronic structure in the interpretation of the STM images of ReS_2, it has been shown that the electronic topography dominates and that the image cannot be interpreted as a direct topography map of the crystal structure. In interpreting STM image data of nanoparticles and layer step edges, each material will be referenced to the bulk basal plane investigations.

2. STM Studies of LTMC Step Edges

A major focus of this project is to determine the electronic and structural properties of LTMC edges and defects. It is at these features that the chemical reactivity and many of the physical properties of the materials are most important. Fig.28. shows an atomically resolved STM image of a step edge on the (0001) plane of NbS_2. The step edge was found by first scanning a 50 x 50 nm^2 surface area and then increasing the image resolution and focus on the step edge. Images of NbS_2 step edges could be obtained at bias voltages in the range from 0.025 to 0.2 V while holding the tunneling current setpoint at 3nA. At bias voltages higher than 0.1 V, images of the step edge was not stable. This result indicates that the step edge is metallic in character, as is the bulk material, and that imaging at higher voltages leads to decomposition of the edge.

The lattice constant on the bulk terrace of the NbS_2 step edge was 3.31 Å while the lattice constant near the step edge varied less than 1% of bulk lattice constant. While imaging this material, edge-like artifact were frequently observed. Such artifacts can be discerned by changing image scan direction and noting if the feature remains stable. True material features, in contrast to imaging artifacts, are stable and

repeatable while varying scan direction. Since images can be obtained while scanning either right-to-left or left-to-right, this can provide a good test of reliable image data. The step edge in Fig. 29 was stable while scanning in both directions unlike artifact that is disappeared if scanning direction is changed.

Images of NbS_2 are frequently complicated by the presence of site defects, particularly missing atom defects. In particular, the observed edges were generally found to exhibit long range disorder but are found to preferentially cleave at $[10\bar{1}0]$or $[\bar{1}010]$ edges. The two-dimensional metallic state in trigonal prismatic NbS_2 is primarily derived from Nb dz^2 orbitals while the sulfur p-derived electronic states are found in bands below the Fermi level. However, because of the proximity of the sulfur atoms to the STM tip, the observed tunneling current density preferentially results from sulfur electronic state density despite the comparatively lower contribution to the Fermi level band from these atoms.[95] It has been shown that this phenomenon occurs in all LTMCs investigated to date, including bulk NbS_2.[147-149] Based on this, it can be seen that the edge termination forms alternating 60° and -60° angles with the bulk hexagonal sulfur lattice and so the termination edge is either $[10\bar{1}0]$ or $[\bar{1}010]$. Other low Miller index edges such as $[11\bar{2}0]$ were not observed in our data set indicating that typical cleavage edges for these other terminations are likely to be considerably higher in energy and unstable. This result is in contrast to graphite, which has been found to cleave at both $[10\bar{1}0]$ and $[11\bar{2}0]$ edges. The image data for NbS_2 edge states does not indicate the presence of any superstructure in the near-edge region. Measurements of the bulk lattice constant and topographical height of the high intensity spot pattern indicate that the lattice is bulk-like up to the terminal edge atoms. Our results do not indicate the presence of a

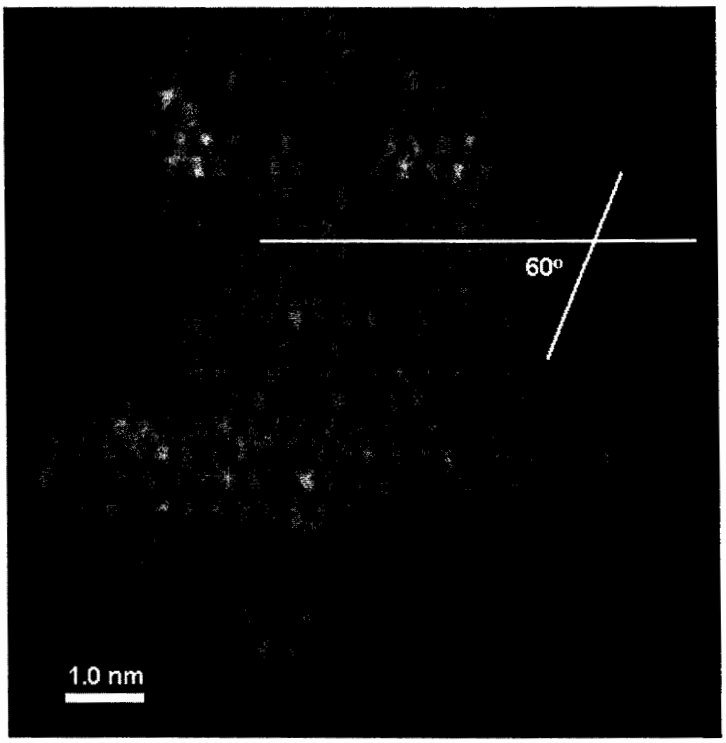

Fig. 28. STM image of (a) bulk NbS_2 with I_{tun} = 3 nA and V_{bias} = 0.08 V.

pronounced high electron density state at the edge, which is also in contrast to graphite $[10\bar{1}0]$ edge states. In fact, by averaging the height data of the terminal atoms, we find that the edge-most atomic site is slightly lower in height or electronic state density than that of the bulk lattice. It is apparent that NbS_2 edge states have a capacity to self-anneal dangling bond edge states without creating unique edge-localized electronic states. From the STM image data, it is not possible to distinguish between the $[10\bar{1}0]$ or $[\bar{1}010]$ edge types although statistically, one should observe each type with equal probability. In fact, data obtained in our study only includes step edge features typical of Fig. 28. This might result from the one or the other edge type being unstable and therefore unable to be imaged.

Although step edges can, in principle, be observed on the other LTMCs, stable images suitable for subsequent analysis could not be obtained. It is possible that step edges in the other materials were too reactive under imaging conditions or that the large variation in electron density at the edge of semiconducting materials prevents stable imaging. In either case, the focus of the next section deals with investigation of nanostructured LTMCs which are, in a sense, "all-edge". This approach has yielded a wealth of new information as to the nature of the edge properties of LTMCs.

3. STM Studies of Nanostructured LTMCs

3.1. Substrates

In order to image nanostructured LTMCs by STM, the nanoparticles must be placed on a suitable substrate which is atomically flat (in order to avoid confusing substrate and nanoparticle features), inert (so as not to alter the nanoparticle structural and electronic properties), and be metallic.

Highly Oriented Pyrolytic Graphite (HOPG) offers a good combination of these properties. HOPG is highly ordered in the c-axis stacking dimension and has large crystals in the basal-plane dimension on the order of 1-5 microns. The (0001) basal plane of HOPG has long been investigated by STM in which images of graphite show one HED spot per surface unit cell. The lattice spacing of the HED spots is 2.46 Å and are hexagonally arranged which is consistent with the crystal structure of graphite. The implications of the observation of one HED spot per unit cell has been extensively investigated.[100, 150, 151]

Single layer flakes such as shown in Fig. 29 has been observed many times near the step edges during probing the basal plane of graphite. Since such features could easily be confused with adsorbed LTMC particles, is it important to note that particles found near substrate step edges are suspect and should not be used for nanoparticle analysis. In this project, only unique particles distinct from substrate step edges were used for analysis.

Another defect state on the basal plane of graphite has been also observed in rare cases. Fig.29b shows a depressed region or pit likely formed by a large defect in the layer below. The various reports have been published and demonstrated that the pit seems to be formed during the crystallization naturally rather than the pit formed during the STM scanning and the pit is initiated with a triangular shape.[152] NbS_2, $NbSe_2$, TaS_2, and $TaSe_2$ also exhibit the triangular pits on the basal plane.[153-155]

TaS_2 is semimetallic and flat, making it a viable candidate for use as a substrate. Fig. 30 is a series of STM images obtained by scanning a 1 μm x 1 μm area of TaS_2 showing nucleation and lateral growth of pits in the surface. At the initial scanning time, the number of pits is distributed randomly over the basal plane

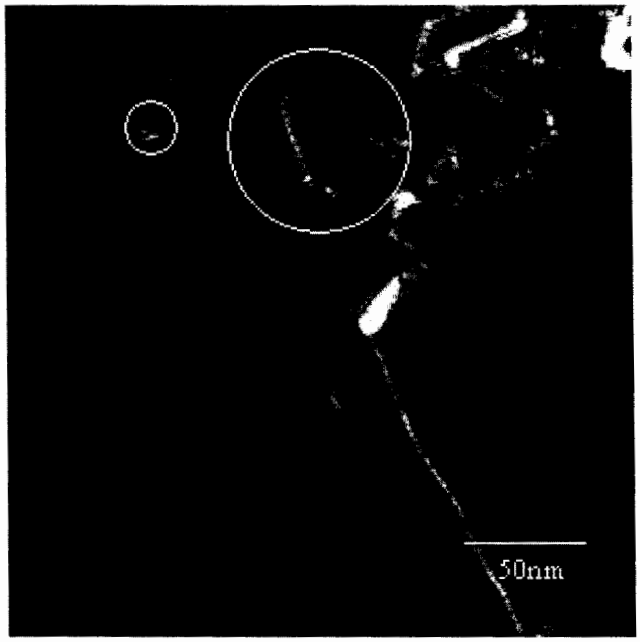

(a)

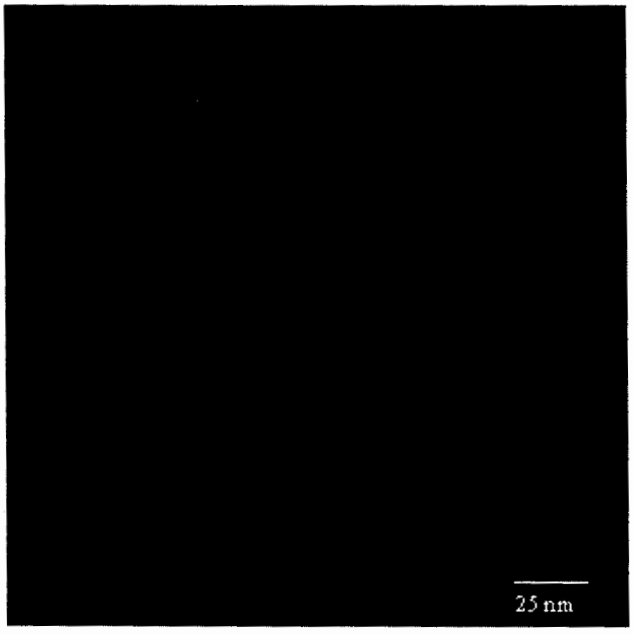

(b)

Fig. 29. (a) STM image of a step ribbon at the corner of step edge and a small flake indicated by the small and large circles, respectively. (b) STM image of an etch pit on graphite substrate surface.

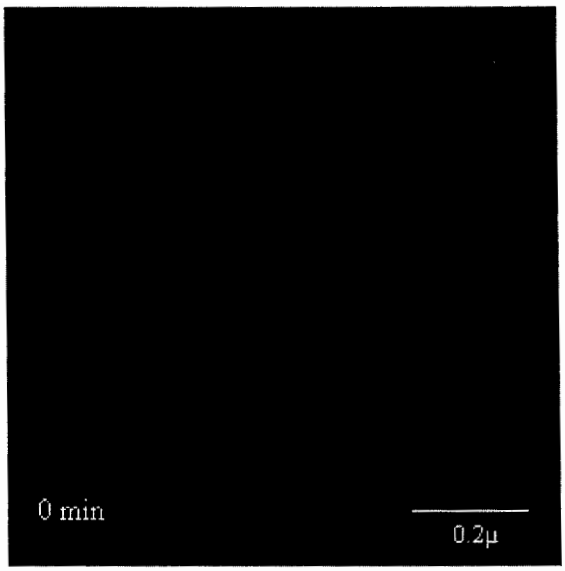

(a)

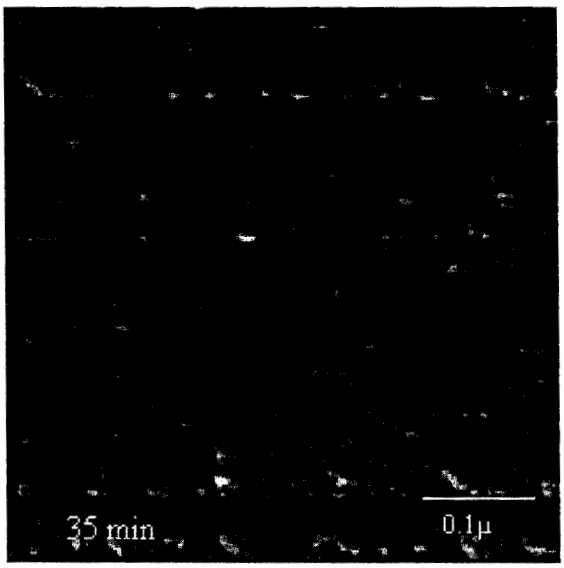

(b)

Fig. 30. A squence of STM images of pit growing and nucleation of TaS_2 with I_{tun} = 3 nA and V_{bias} = 0.025 V.

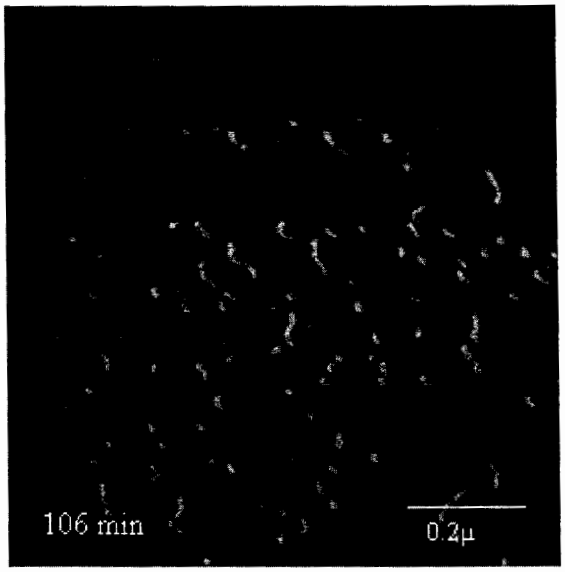

(c)

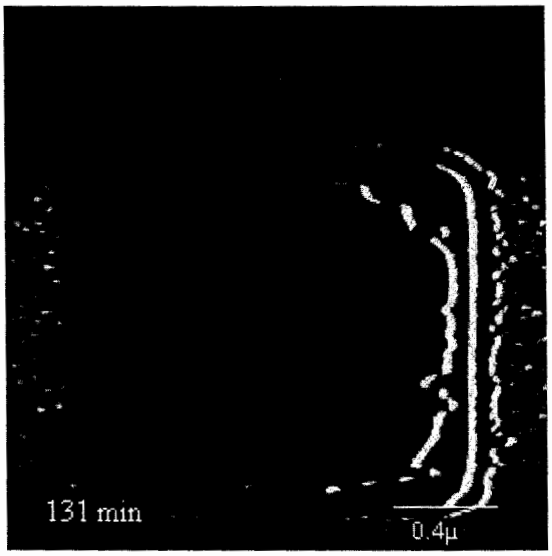

(d)

Fig. 30. A squence of STM images of pit growing and nucleation of TaS_2.

and increased with continuous scanning. The pit growth and nucleation on TaS_2 have been explained as the tip and substrate surface interaction via the adsorption of H_2O.[154,155] The rate increase is attributed to the increase of the exposed defect state hence the amount of exposed edge "reactant" increases with time. Such instability in the basal plane of TaS_2 during STM imaging renders this material unsuitable for use as a substrate.

Other materials, including NbS_2, $NbSe_2$, TaS_2, $TaSe_2$, MoS_2, and $MoSe_2$ were similarly investigated for use as a substrate. Images were recorded over extended periods of time keeping the bias voltages and tunneling current set points the same as for normal basal plane imaging. Results showed that pits and defects also formed in all of these materials and that the growth rate decreased in the order $TaSe_2$, >TaS_2, >$NbSe_2$, >NbS_2, >MoS_2, >$MoSe_2$. $TaSe_2$ appeared to have the fastest rate while MoS_2 and $MoSe_2$ did not show pit formation over the time range of 2 hours. The formation of pits and defects in all of the materials except MoS_2 and $MoSe_2$ also render them unsuitable for use as a substrate.

Graphite, MoS_2 and $MoSe_2$ are sufficiently stable under STM conditions for suitable use as substrates. In this project, only these materials were used for nanoparticle investigations.

3.2. STM Studies of Nanostructured LTMCs

3.2.1. STM Image of Nanostructured NbS_2 and $NbSe_2$

Fig. 31 presents a low resolution STM image of $NbSe_2$ nanocluster on a graphite (0001) surface. The observed lattice of this particle is 3.15 ± 0.15 Å which is less than the NbSe2 bulk lattice constant of 3.45 Å. The particle is clearly not a graphite particle since graphite's lattice constant of 2.45 Å is significantly smaller

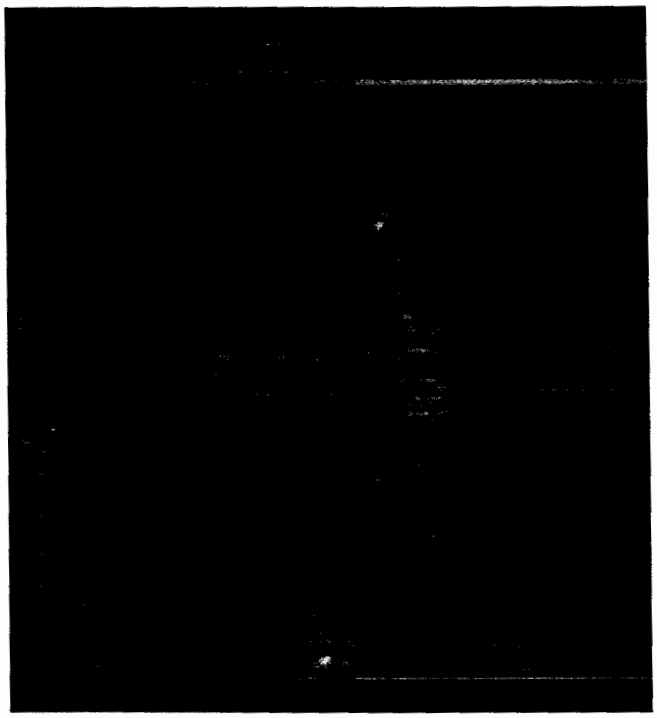

Fig. 31. STM image of $NbSe_2$ nanocluster deposited on graphite substrate. The image was taken with tunneling parameters; I_{tun} = 3nA and V_{bias} = 0.12 V.

than that observed for this particle. The reduction of atomic lattice constant for the $NbSe_2$ particle may result from the lattice mismatch between the graphite substrate and the particle. In such cases, either the substrate, the particle or both will adjust the lattice spacing in order to passivate the interfacial energy. Since the graphite substrate is not visible beneath the particle, it is not clear if the substrate has undergone lattice expansion. However, it is clear that the $NbSe_2$ particle has undergone lattice constriction by about 10%. In part, the lattice constriction of the nanoparticle may be caused by the presence of the STM tip. It has been recognized that the force of the tip on the surface can be significant, even under low current/bias conditions.[156] The attractive force can contribute to the lattice mismatch interfacial energy by increasing the contact between the substrate and nanoparticle. .

The $NbSe_2$ nanocluster in Fig. 31 indicates a hexagonal pattern as expected from the bulk basal plane lattice. It can also be seen that the $NbSe_2$ lattice is oriented parallel to the graphite substrate lattice. In cases of adsorbates on surfaces having different lattice spacing - and/or symmetries, it is often the case that the adsorbate or substrate will undergo reconstruction to passivate the interfacial energy. Because of the parallel orientation of the adsorbate with respect to substrate surface, superstructures such as Moiré patterns, which result from a relative rotation of toplayer with respect layer below [157 - 159], are not observed in this case. In addition, the $NbSe_2$ nanostructure does not exhibit the presence of a superstructure, which could result from electronic or structural reconstruction at the substrate surface near the edge of the cluster, is observed. No observation of superstructure on substrate near the $NbSe_2$ nanocluster indicates that the adsorption strength is not considerably strong.

The STM image data depends on several factors including, mechanical tip-nanocluster interactions, substrate-nanocluster interaction, and on the intrinsic properties of the materials such as the edge-induced electronic structure modification and coordinate variation at the edge. The mechanical interactions among the $NbSe_2$ nanocluster, tip and substrate are often not negligible. However, these effects are not dominant factors in STM image of the $NbSe_2$ nanoclusters since the edge region and bulk lattices are bulk-like and do not exhibit unique features that might otherwise be `due to mechanical interaction effects. It is apparent that the STM image data represents intrinsic properties of $NbSe_2$ edge.

At low bias, the STM tip is in closer proximity to the nanocluster and therefore exerts a higher repulsive force on the nanocluster. Under such conditions, the nanocluster may slide on the graphite basal plane making it difficult to obtain stable image data. Changing the bias voltage from 0.025 to 0.12 V at constant current increases the tip-sample separation with a corresponding increase in the gap resistance, in relation to Ohm's Law V/I = R, thereby reducing the tip-sample interaction. Therefore, stable STM images for nanocluster on substrates could only be obtained at higher bias voltage or lower tunneling current.

The observed the bias voltage dependency of STM images of nanoclusters showed that below bias voltages of 0.070 V, STM imaging of the nanoclusters was not possible because of tip-induced nanocluster sliding. Conversely, above bias voltages of 0.15 V, it became difficult to observe atomic resolution since noise in the tunneling current increases at larger tip-sample separations. Atomic resolution STM images were observed within the range from 0.070 to 0.15 V.

3.2.2. STM Images of Nanostructured MoS_2 and WS_2

Stable STM images of nanocluster MoS_2 and WS_2 could be obtained as shown in Fig. 32 and 34. These materials are both semiconducting with bulk band gaps of 1.30 eV and 1.45 eV for MoS_2 and WS_2 respectively. Fig. 32 shows a typical STM image of a MoS_2 nanocluster adsorbed on a graphite substrate. In this material, a novel superstructure appears near the edge while a bulk like lattice exists toward the center of nanocluster. The superstructure is localized near the edge and extends 2-3 nm toward the center of the nanocluster and is oriented at 30° with respect to normal lattice. The superstructure has a repeat distance of $\sqrt{3}$ times the basis lattice, hence the superstructure has a Woods notation of $(\sqrt{3} \times \sqrt{3})R30°$.

Atomic basal plane lattice constants in the center region of the nanocluster ranged from 2.65 to 2.8 Å that are less than atomic bulk lattice constant of 3.16 Å. The hexagonal lattice pattern is the same as that of the bulk. The reduced interatomic distance indicates that the nanocluster is compressed relative to bulk. There are several possibilities that might result in the observed compression. First, the compression might be due to relaxation of interfacial energy at the nanoparticle. Graphite has a lattice constant of 0.246 nm leading to successive next-nearest neighbor distances of 0.426 ($\sqrt{3}$a direction), 0.492 (2a direction), 0.651 nm ($\sqrt{7}$a direction) as shown in Fig. 33. The lattice mismatch between the nanocluster and the substrate can be mitigated if rotating the relative angles of the lattice constants leads to a better match. In the case of MoS_2, the most favorable short range mismatch occurs if the nanocluster lattice constant is oriented parallel to the $[3\bar{1}40]$ ($\sqrt{7}$) substrate direction such that two time the MoS_2 lattice constant (2 x 0.316 nm = 0.632 nm) varies from this substrate axis ($\sqrt{7}$ x 0.246 = .65 nm) by about 3%. The lattice compression observed in the nanocluster is on the order of 14% and so it is

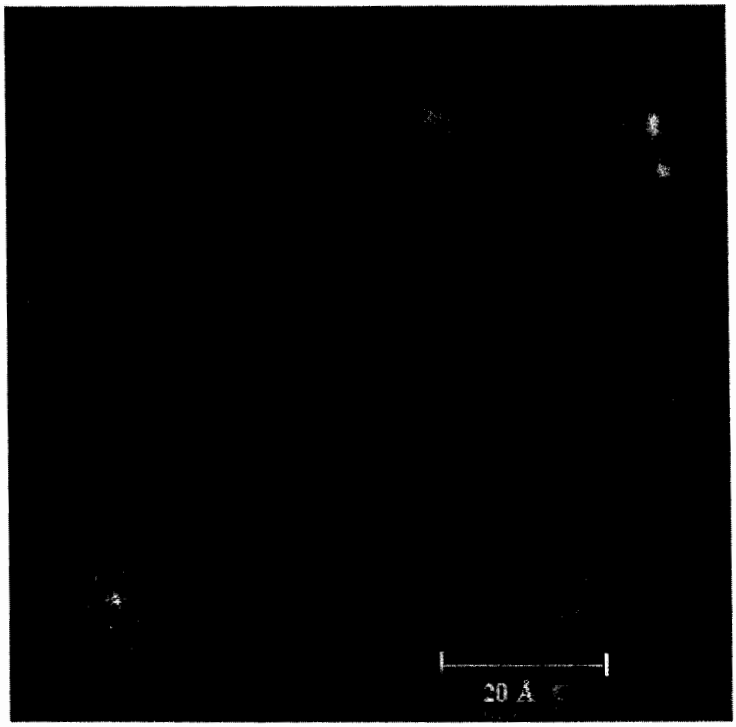

Fig. 32. STM image of MoS_2 nanocluster deposited on graphite substrate with I_{tun} = 7 nA and V_{bias} = 0.55 V. Inset is the 2DFFT of image. The outside hexagon presents the bulk lattice. The inside hexagon represents ($\sqrt{3}$ x $\sqrt{3}$) superstructure rotating with respect to bulk lattice.

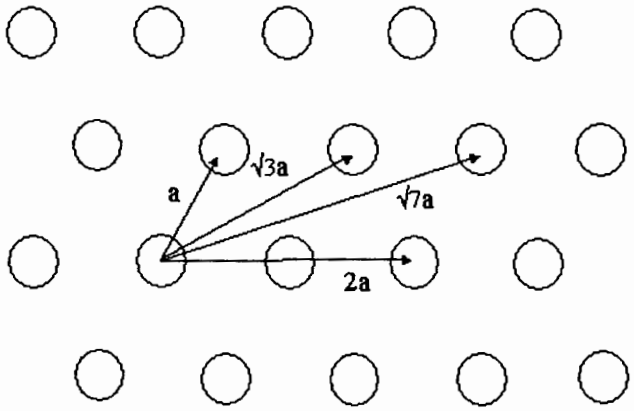

Fig. 33. Diagram depicting relative lattice vector lengths for next-nearest neighbors in a hexagonal lattice.

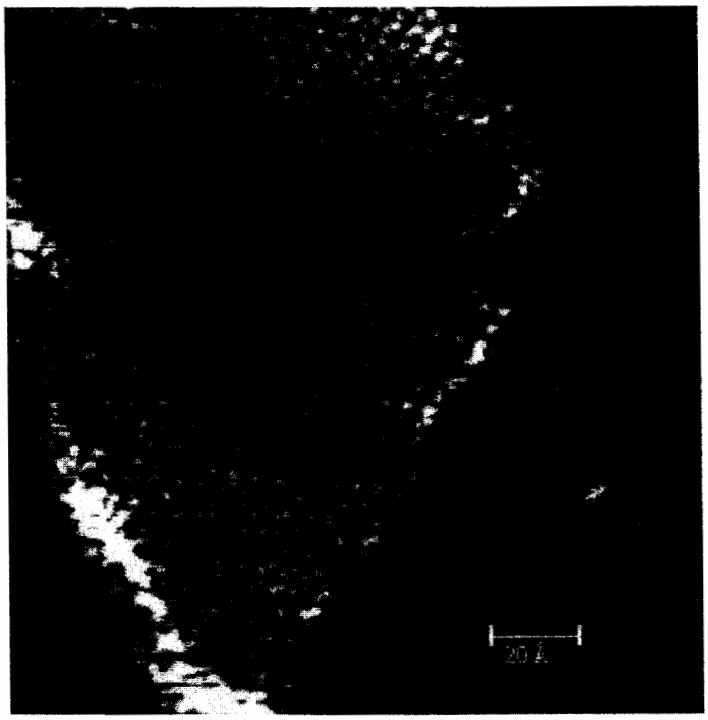

Fig. 34. STM image of WS_2 nanocluster deposited on graphite substrate with I_{tun} = 3 nA and V_{bias} = 0.15 V. Inset is the 2DFFT of image showing ($\sqrt{3}$ x $\sqrt{3}$) R 30° superstructure.

unlikely that lattice mismatch alone is responsible for the observed compression. A more likely cause of the observed lattice contraction is that the electronic state density of the substrate, since it is metallic, is much higher than that of the semiconducting nanoparticle. The contribution of electronic density from the graphite to the particles might be causing the metal-sulfur bonds to lengthen (approximately normal to the surface) and the sulfur-sulfur distances to compress.

Thirdly, the surface (or edge) tension of the nanoparticle would be expected to cause contraction of the edge length around the particle. This is the same reason that liquid mercury tends to minimize its surface area. The consequence of this for the nanoparticle would be to minimize the amount of edge area by reducing the size of the particle such that the increase in lattice energy caused by the contraction would be offset by the reduction in surface tension. Although it is not possible to definitively assign the effect that is responsible for the lattice contraction, it is likely to be a combination of the above.

We now turn to a discussion of the observed superstructure near the nanoparticle edge. Since MoS_2 is isostructural with NbS_2, differing only by the lattice constant, it is unlikely that the superstructure observed in MoS_2 results from external effects such as the interaction with the substrate. The origin of the superstructure must result from some intrinsic property of the geometric or electronic edge structure. This is supported by the observation of the superstructure also appearing in WS_2 nanoclusters. WS_2 nanoclusters adsorbed on the graphite substrate also exhibits the localized $(\sqrt{3} \times \sqrt{3})$ R30° superstructure extending 2 or 3 nm from edge into the bulk region. The inset in Fig. 34 is a 2-dimensional Fast Fourier Transform (2DFFT) of the image of the WS_2 nanocluster. The 2DFFT plot is a

reciprocal plot (power spectrum) of the image and shows bright features at frequencies for which there exists a high degree of periodicity in the image. The outer set of six features arraigned in an approximately hexagonal pattern represent the periodicity of the bulk nanoparticle lattice. The inner set of six features rotated at 30° from the outer set represents the ($\sqrt{3}$ x $\sqrt{3}$) R30° superstructure. For both MoS_2 and WS_2 nanoclusters, the 2DFFT patterns are the same showing superstructures with 30° rotation. This 2DFFT indicates that the physical structures at edge for MoS_2 and WS_2 nanoclusters are similar. This similarity is consistent with both materials being semiconducting. In the case of semiconductors, surface cleavage always results in the formation of broken dangling bonds which undergo reconstruction to minimize the surface energy. For example, Si (111) surface can undergo a reconstruction resulting in a rearrangement of the top three or four layers of atoms. In contrast, metals are able to relieve the electronic stress at a surface much more effectively and do not generally exhibit significant reconstruction except at the top-most layer. This is contestant with the bulk-like lattice observed at the layer edge of NbS_2 step edges and at $NbSe_2$ nanoparticle edges. In the case of layered semiconductors, the stress caused by the broken bonds at the edge can only be relaxed by reconstructing in a single layer since no chemical bonding (other than van der Waals) occurs between layers. Thus, all of the reconstruction must occur within the atomic layer near the layer edge. Given this, it is not particularly surprising that the reconstruction would extend 2-3 nm into the bulk.

In order for the above hypothesis to be viable, the edges of the bulk metallic LTMC nanoparticles (NbS_2 and $NbSe_2$) must be metallic. This point can be shown from the fact that stable images of the metallic LTMCs can be imaged at

comparatively low bias voltages. The bias range for metallic NbS_2 and $NbSe_2$ are from 0.025 to 0.15 V. This range suggests that metallic LTMC nanoclusters are metallic at the edge and thus exhibit a HED near the Fermi level. For semiconducting LTMCs, the bias voltage required for imaging was comparatively larger. For example, the atomic resolution images were acquired with the negative bias voltage ranges between 0.3 and 0.7 V for MoS_2 and between 0.1 and 0.3 V for WS_2. Since somewhat lower bias voltages were needed for the MoS_2 nanoclusters than for bulk MoS_2 (typically 0.75 – 1.50 eV) there may be a slightly higher electronic density at the Fermi level for the semiconducting nanoparticles, suggesting that some new electronic bands may arise at the layer edge. Moreover, the bias voltage used for the atomic resolution imaging of the WS_2 nanocluster was only slightly higher than that required for the $NbSe_2$ nanoclusters. Consequently the WS_2 nanocluster may be semimetallic having a very narrow band gap. We pursue these issues using computational methods as described below.

3.2.3. STM Images of Nanostructured ReS_2

ReS_2 has considerable less symmetry than the other LTMCs investigated in this project. The sulfur in the outer layers of the S-Re-S trilayer are not coplanar and lie in four distinct crystal geometries as determined from X-Ray and prior STM investigations. Nanostructured particles of these materials were also investigated in order to help establish the nature of the superstructure observed in MoS_2 and WS_2 nanoparticle layer edges. Fig. 35 shows an STM image of a ReS_2 nanocluster. In the bulk area of nanocluster, a 2.6Å periodic hexagonal pattern was observed which again represents a compression of the bulk lattice on the order of 18 %. At edge region toward the left, a planar localized superstructure having $(\sqrt{3} \times \sqrt{3})R30^\circ$ is

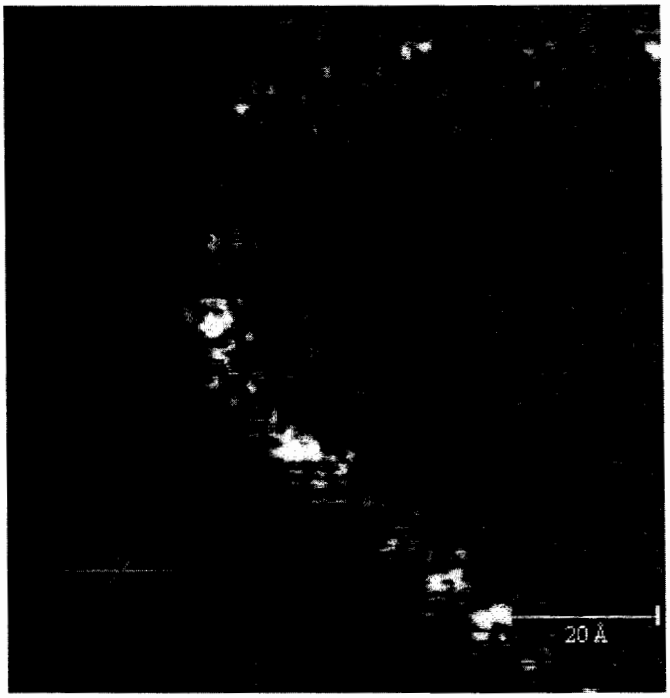

Fig. 35. STM image of ReS_2 nanocluster deposited on graphite substrate with I_{tun} = 4 nA and V_{bias} = 0.3 V. Inset is the 2DFFT of image showing ($\sqrt{3}$ x $\sqrt{3}$) R 30° superstructure.

observed. The bulk lattice of nanocluster is very different from that of the other LTMCs such that the S layer is puckered but still has an overall hexagonal pattern (see Fig. 27).

3.2.4 Passivation of the Edge Structure in Nanostructured MoS_2

We also attempted to modify the edge structure of MoS_2 by creating nanoclusters in the presence of RSH mercaptans. This approach was intended to provide a variation of the edge structure through passivation of the edge states. The solubility of the nanoclusters was markedly different that unmodified nanostructured MoS2 in that the solution was far less stable in polar solvents. The reduction of stability of the colloid in polar solvents indicates that the R group on the mercaptan (hexyl and octyl) made the particles less polar. These RSH modified materials were also imaged by STM, however, we observed that there was no difference in between the STM images of pure solvent prepared nanoclusters and those prepared in the presence of the RSH moiety. Both materials showed the same near-edge superstructure. In the lack of any solid evidence that the modification effected any change in the edge structure, we must allow for the possibility that if the modification was successful, as indicated by the solubility changes, that this modification did not affect the electronic structure of the edge. It is also possible that the edge was not modified at all and that the solubility changes were caused by association of the RSH molecules on the basal planes. The latter possibility, however, is not consistent with the known inert properties of the basal plane.

From these results, the nature of edge is rather complicated by several factors, namely, the unknown chemical composition and geometrical structures and the electronic properties. Therefore, STM images cannot be unambiguously interpreted

without a fundamental understanding of the complex interrelationship between the local electronic and geometric structure. In order to shed further light on these systems and provide a means to interpret the experimental data, we have undertaken computational studies which are described below.

B. Computational Investigations of LTMCs

1. Properties of Bulk LTMCs

The properties of the LTMCs investigated in this project were investigated using the density functional method. To begin, it is exceedingly important to build ribbon models of the materials based on relaxed structures. This is because the calculated structures must be obtained using approximations as part of the calculations. If ribbon models were built entirely from experimentally reported structures, stresses would exist in these structures that might compromise the validity of the results. Moreover, it would have to be inherently assumed that the experimental structures are correct and valid which may not be the case. Optimizing the structure of the bulk materials allows a validation of the computational techniques. Validating the computational technique is essential if the computed results are to be believable.

The geometry of the bulk unit cell of 2H-MoS_2 was optimized and compared with experimental values. . The lattice constants varied by less than 0.1 % compared with experimental values. This result was obtained using a cutoff energy of 320 eV for the pseudopotantial. Using a lower energy cutoff resulted in a smaller computational time but with correspondingly higher variation in lattice constant. Larger cutoff energies did not significantly improve the calculated results to justify the increase in computational time required. The pseudopotential used for all DFT

calculations was GGA-PW91. This pseudopotential was selected after surveying other available pseudopotentials, including GGA-PBE and LDA, to find the one which provides the best validation for the LTMCs studied.

The calculated and experimental lattice constants are listed in Table II. The optimized lattice parameters of MoS_2 (a, b = 3.183 Å,) are well validated with experimental parameters. However, the c axis lattice parameter (c = 12.71 Å) was underestimated compared with the experimental value by 9.5%. This contraction in the c-axis occurs mostly in the interlayer separation rather than in the intralayer bond distances. Consequently, since we are focusing on the properties a single layers, this effect is less important.

The calculated band structure and DOS of MoS_2 are shown in Fig.36. The calculated indirect band gap is 0.52 eV, considerably lower than the experimental optical gap of 1.45 eV. The low band gap value arises from a computational limitation such that the optimization is performed in the ground state, and so the excited states are underestimated.[160] This limitation has been recognized in DFT calculations and a post-calculation adjustment is made to correct the band gap for properties calculations which are sensitive to the band gap. The projected DOS provide an assignment of the orbital contribution to the band states. For MoS_2, the top of the valence band consists of mainly of metal d_z^2 orbitals This result is consistent with experimentally measured dispersion curves for MoS_2.

Isostructural LTMCs are expected to have similar band structures. As shown in Fig. 37, the overall band structure of NbS_2 is similar to MoS_2, but the Fermi level falls in the dz2 band making it metallic. The difference in Fermi level for MoS_2 and NbS_2 results from there being an extra electron in the Nb d manifold compared to Mo d.

Table II. Optimized Lattice Constants of Bulk LTMCs

	GGA PW 91			GGA PBE			LDA		
Compound	a (Å)	b (Å)	c (Å)	a (Å)	b (Å)	c (Å)	a (Å)	b (Å)	c (Å)
NbS2	3.342	3.342	13.699	3.340	3.340	13.718	3.269	3.269	13.537
NbSe2	3.459	3.459	12.678	3.465	3.465	12.721	3.389	3.389	12.611
MoS2	3.183	3.183	12.708	3.179	3.179	12.710	3.135	3.135	12.271
WS2	3.155	3.155	12.360	3.190	3.190	12.700	3.148	3.148	12.102
ReS2	6.482	6.544	13.299						

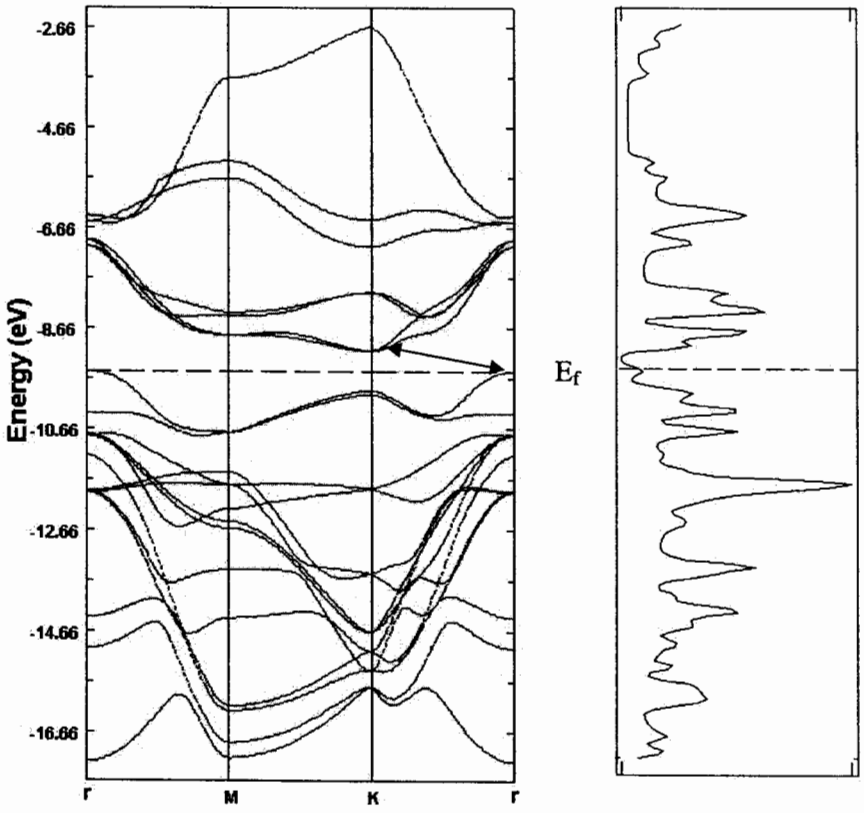

Fig. 36. Calculated (a) band structure of bulk MoS_2 with DOS. The arrow indicates the indirect band gap. The Fermi level is marked by the broken line.

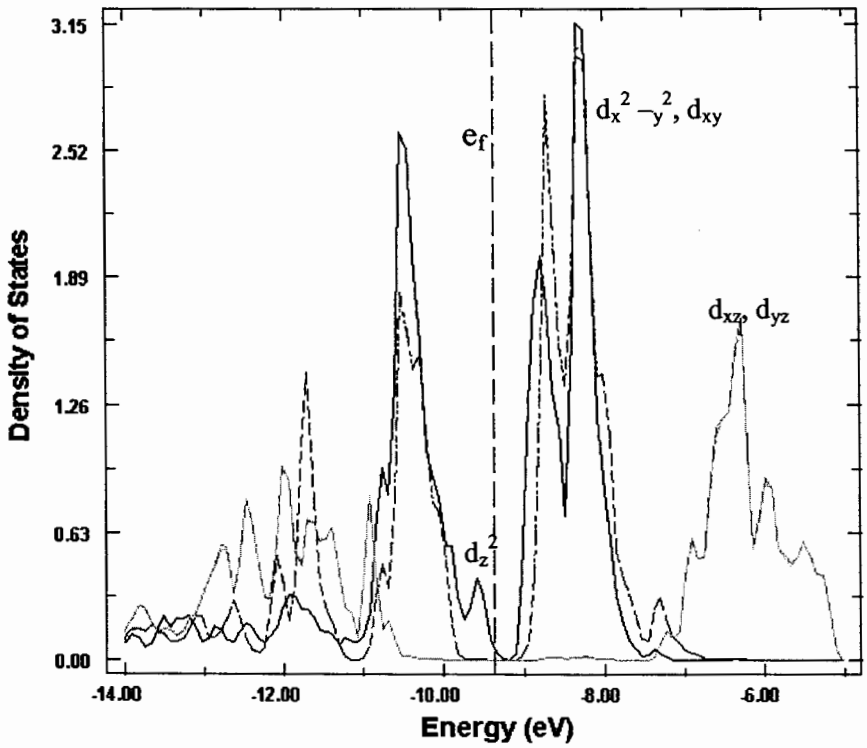

Fig. 36b. PDOS of bulk MoS_2. The Fermi level (e_f) is marked by the broken line.

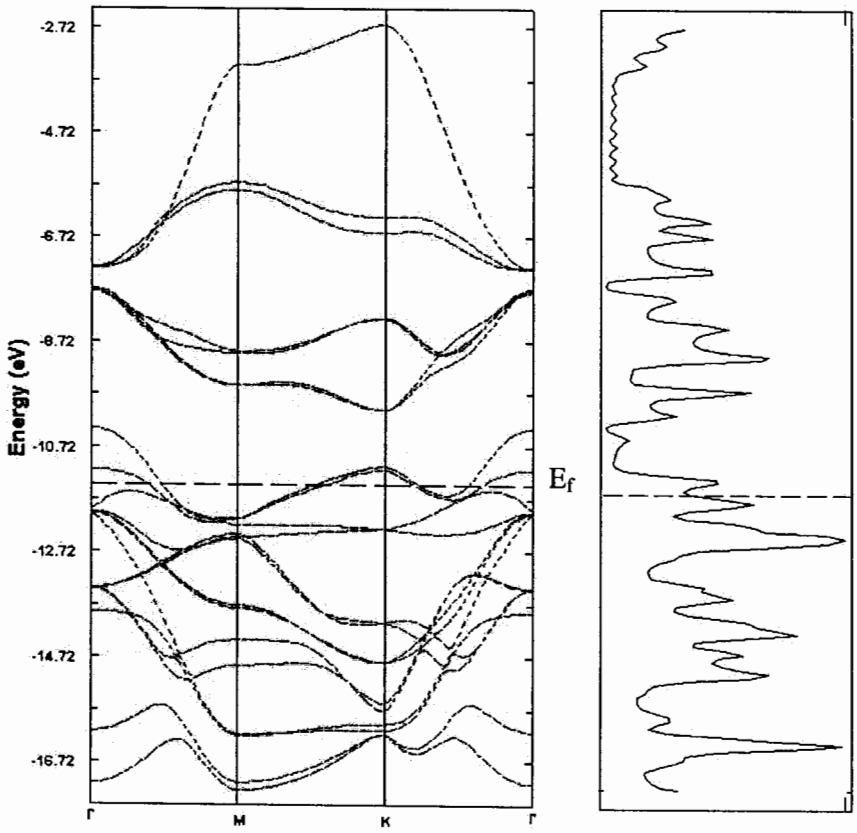

Fig.37. Calculated band structure of bulk NbS_2 with DOS.

Simulated STM images representing the surface projected DOS were calculated for bulk LTMCs. In these simulated images, both tip-to-sample and sample-to-tip tunneling was calculated representing the conduction and valance bands respectively. For MoS_2, the simulated STM images for the valence and conduction bands shown in Fig. 38 are different. These images show that the high intensity spots for the conduction band are derived from the sulfur p_x and p_y orbitals and are directed more toward other atoms in the basal plane making them appear triangular. In contrast, the calculated image for the valence band shows more circular high intensity spots reflecting the fact that these bands are derived mainly from the sulfur p_z orbitals and are directed normal to the basal plane. It must be kept in mind that the observed crystal orbitals which dominate the image are projected from the surface and reflect the electronic state density at a particular distance from the surface. Thus, even though the main components of the bulk conduction and valance bands are derived from the Nb atomic d-electron states, the tip is nearer to the sulfur atoms and so atomic crystal orbitals derived from these atoms dominate the image. Moreover, the particular shape of the high electron density spots also reflects the fact that the calculations do not include the effects of vibrational motion of the atoms and so effectively represent a $0^{o}K$ calculation. We conclude that the images of MoS_2, as well as all the other LTMCs, represent DOS topographies of the top sulfur layers, and not the metal layers. .

The argument that the STM images represent topographies of the sulfur layer is particularly clear from a comparison of simulated images of ReS_2 which has a puckered sulfur layer. [11] Calculated STM images of ReS_2 shown in Fig. 39 display the electron density variation with respect to the crystal geometry. Kelty et al

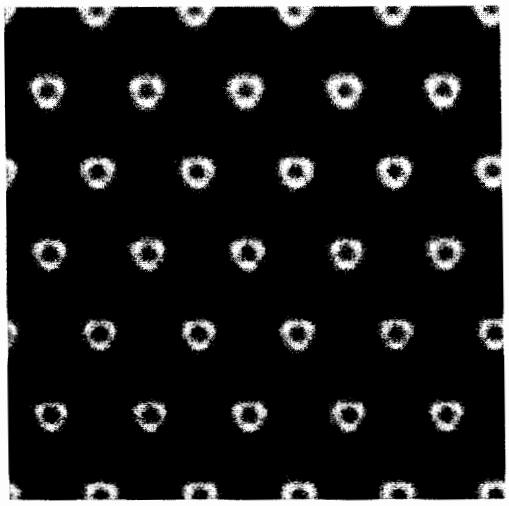

(a)

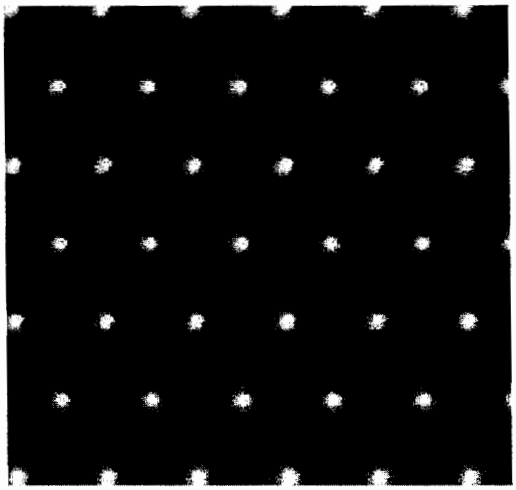

(b)

Fig. 38. Calculated STM images of (a) conduction band and (b) valence band of bulk MoS_2.

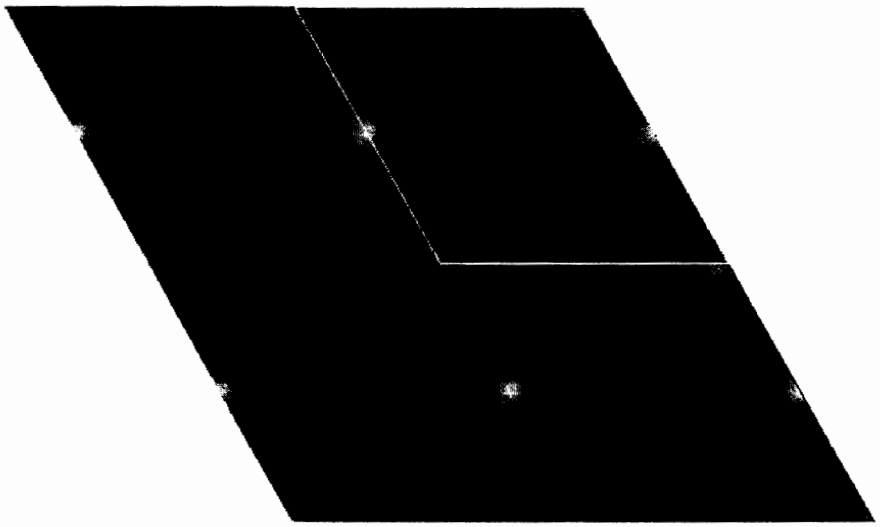

Fig. 39. Calculated STM images of bulk ReS_2. Lines show a unit cell.

calculated the STM image of ReS_2 based on the crystal structure determined from XRD measurements. From the calculated STM results, it should be pointed out that different electron density patterns may result from variation in scanning parameters, particularly the resistance gap. The electronic DOS topographies may vary as a function of distance from the surface. By changing the tip-sample gap resistance, the tip height can be changed and thus result in variation of the image pattern. In the LTMCS investigated in this project, the sulfur layers are coplanar and so these effects are not expected. Consequently, we did not undertake STM image simulation studies that included height-dependence on the calculated images.

2. Edge Structures of LTMCs

2.1. NbS_2

2.1.1. Geometry Optimization

We have performed geometry optimization and STM image simulation studies on NbS_2 step edges using ribbon structure models based on relaxed bulk structures. Relaxation of the bulk structure resulted in-plane lattice constants a = b = 0.334 nm which compares well with the experimentally reported 0.331 nm. The sulfur-sulfur z-axis separation in the relaxed structure was found to be 0.3103 nm compared with the experimental value of 0.3067 nm. For the edge termination investigated, ribbon models were constructed from the relaxed bulk structure which was reoriented as $(1x\sqrt{3})R0°,30°$ and $(2x\sqrt{3})R0°,30°$ repeat units. This approach allows construction of ribbon model structures with varying width and length so as to accommodate the possibility of reconstruction normal and parallel to the layer edge. Several repeat units on one side of each ribbon unit cell were geometrically constrained to simulate the bulk lattice. For the $[10\bar{1}0]$ and $[\bar{1}010]$ edges, the chemical composition of the

terminal edge was investigated using models terminating in NbS_x- with x = 0, 1, or 2. The $[\bar{1}010]$ "S" edge with 0% sulfur was excluded from the studies since this edge termination results in a structurally and energetically unstable bare Nb edge. Geometry optimization of the five remaining ribbon types showed moderate relaxation of the metal and sulfur atoms toward the bulk. Table III lists the equilibrium S-S pair distances for the optimized ribbon structures. S_{ij} refers to the distance between adjacent S atoms within the same sulfur layer, while S_{ij}* indicates the distance between S-S nearest neighbors for the two sulfur layers. It should be noted that the equilibrium position of the terminal sulfur atom in the $[10\bar{1}0]$ and $[\bar{1}010]$ NbS_x- structures is approximately coplanar with the Nb layer and so the S_{12} distance these structures appears unusually large. Likewise, the values of S_{99}* for the fully sulfided $[10\bar{1}0]$ edge is much smaller than bulk due to the relaxation of these atoms toward each other. This bond shortening results in the terminal sulfur atoms lying 0.058 nm below the sulfur atom plane. Thus, the equilibrium atomic positions for the S layers are found to undergo only slight modification from bulk values except at the terminal positions. We note that simulations of $(2x\sqrt{3})R0°,30°$ of the $[10\bar{1}0]$ "Nb" edge with one terminal sulfur showed that the sulfur atom migrated to a position coplanar with the Nb atoms and bridging two terminal Nb atoms. For all other edge and termination types, optimized ribbon structures of these wider ribbons did not indicate the presence of significant restructuring beyond the results found for ribbons based on $(1x\sqrt{3})R0°,30°$ basis cells. Consequently, the simulations of the ribbon structures do not predict significant restructuring parallel or normal to the layer edge which is consistent with our observed STM image data except for the $[10\bar{1}0]$ "Nb" edge with one terminal sulfur atom.

Table III.

Atomic Pair Distances (nm) for Optimized NbS_2 Ribbon Structures

Atomic pair S_{ij}[a]	$[10\bar{1}0]$ Nb(0%)	$[10\bar{1}0]$ Nb(50%)	$[10\bar{1}0]$ Nb (100%)	$[\bar{1}010]$ S (50%)	$[\bar{1}010]$ S (100%)	bulk (calc.)	bulk (exp.)
1-2	0.3342[b]	0.3342[b]	0.3342[b]	0.3977	0.3318	0.3342	0.3310
2-3	0.3342	0.3342	0.3342	0.3272	0.3366		
3-4	0.3322	0.3342	0.3341	0.3294	0.3345		
4-5	0.3317	0.3387	0.3375	0.3332	0.3342		
5-6	0.3334	0.3357	0.3351	0.3343	0.3342		
7-8	0.3371	0.3330	0.3350	0.3342[b]	0.3342[b]		
8-9	-	0.374	0.354	-	-		
1-1*	0.3103[b]	0.3103[b]	0.3103[b]	-	0.3080	0.3103	0.3067
2-2*	0.3103	0.3103	0.3103	0.3186	0.3049		
3-3*	0.3103	0.3103	0.3103	0.3122	0.3100		
4-4*	0.3103	0.3112	0.3103	0.3099	0.3103		
5-5*	0.3117	0.3094	0.3061	0.3098	0.3103		
6-6*	0.3088	0.3117	0.3094	0.3103	0.3103		
7-7*	0.3117	0.3155	0.3150	0.3103	0.3103		
8-8*	0.3125	0.3174	0.3151	0.3103[b]	0.3103[b]		
9-9*	-	-	0.2010	-	-		

a) Refer to below figure for label designations
b) Indicates constrained (bulk) ribbon edge

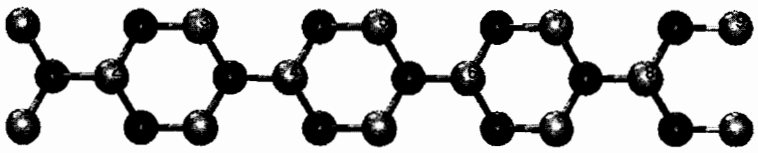

Fig. 40. Leveling scheme for table III.

2.1.2. Electronic structure and image simulation

The metallic character of bulk NbS_2 results from a partially filled band primarily derived from the Nb dz^2 orbitals. Shown in Fig. 37 is a calculated band diagram for bulk NbS_2 showing the metallic state at the Fermi level. The bulk band structure at the surface of an isotropic material undergoes significant splitting due to the inherent loss of symmetry caused by the surface. In low dimensional materials the same splitting occurs although it is limited to splitting along the **a** and **b** reciprocal wavevectors. Wavevectors normal to the layer planes remain nondispersive due to the nondispersive van der Waals interlayer interaction. Moreover, ribbon structures produce flat dispersion curves normal to the layer edge due to the vacuum gap between adjacent layers. Consequently, only symmetry directions parallel to the layer edge ($\Gamma \rightarrow Y$) show dispersive bands. Fig. 41 shows the band structures for the $\Gamma \rightarrow Y$ symmetry axis (parallel to edge) for relaxed $[10\bar{1}0]$ and $[\bar{1}010]$ NbS_x-terminated edges for x = 0, 1, and 2. It is clear that in all cases, the ribbon is highly metallic with bands crossing the Fermi level throughout the symmetry axis. These Fermi level bands are also derived primarily from Nb dz^2 crystal orbitals. However, the proximity of the sulfur atoms to the STM tip is expected to significantly affect the tunneling current density. Below we describe STM image simulation using the calculated equilibrium geometry and electronic band structure calculations.

We have simulated STM image topographies based on the relaxed structures of the $[10\bar{1}0]$ and $[\bar{1}010]$ edges. Although topographies of the Fermi-level crystal orbitals can be generated from the band structure calculations, these can often be misleading for STM image interpretation since these topographies depict the LDOS only at a particular energy irrespective of the distance from the tip. Simulated STM

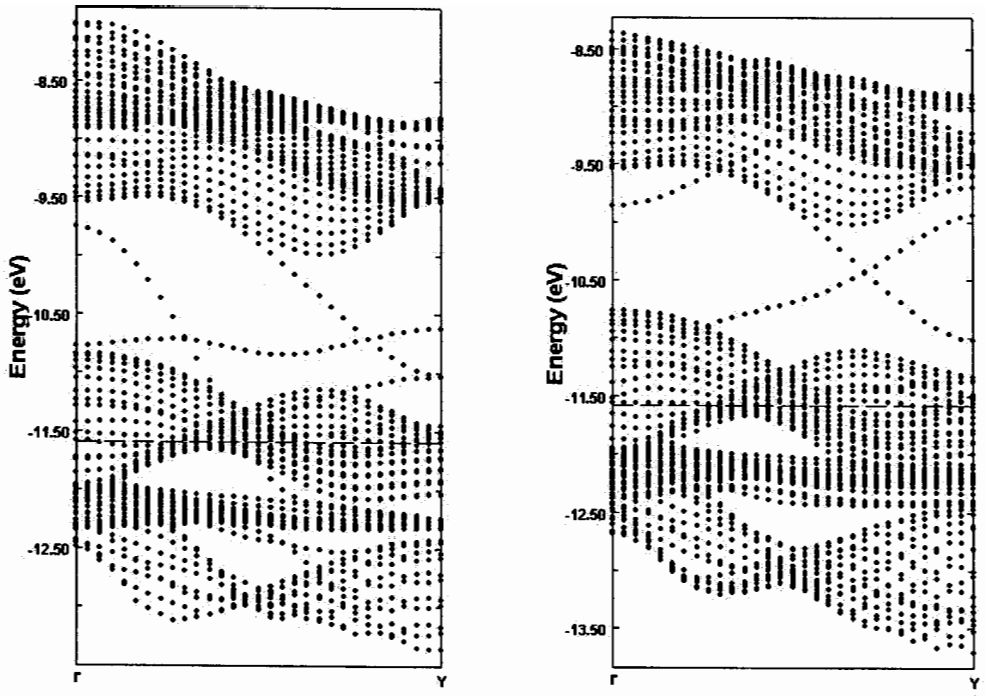

(a) (b)

Fig. 41. Calculated dispersion curves for edge structures for $[10\bar{1}0]$ NbS_x- edge with a), x = 2, b) x = 1.

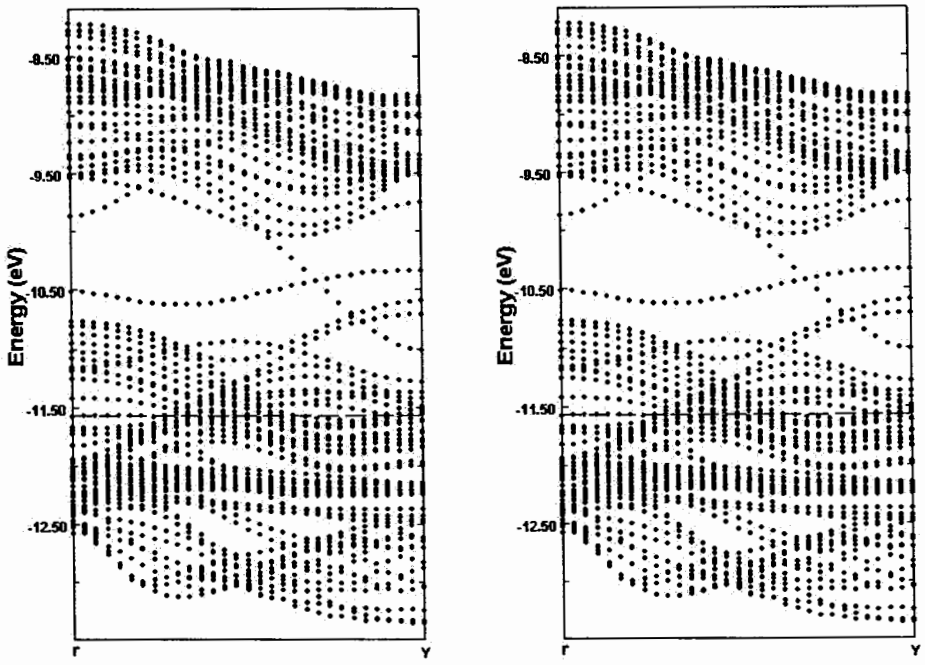

Fig. 41. Calculated dispersion curves for edge structures for $[10\bar{1}0]$ NbS_x- edge with c) x = 0; and for $[\bar{1}010]$ NbS_x- with d) x = 2.

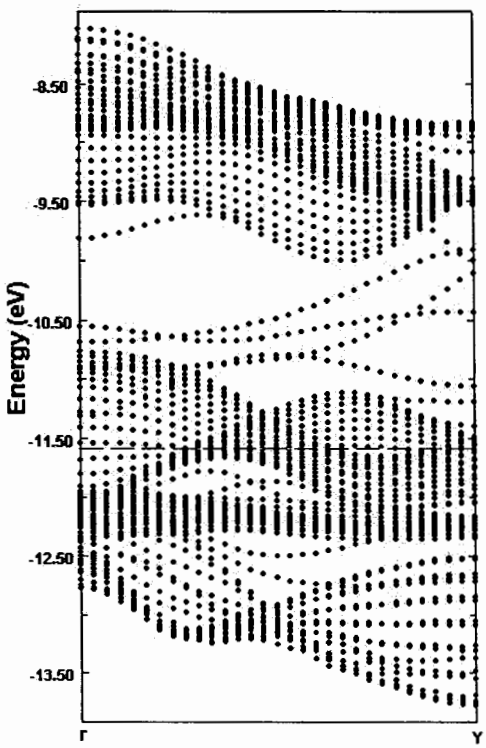

(e)

Fig. 41. (e)Calculated dispersion curve for edge structures for $[\bar{1}010]$ NbS_x- with x = 1.

Simulated STM images of the five ribbon terminated types as described in Fig. 41 are shown in Fig. 42. These images are based on ribbons constructed from a $(1x\sqrt{3})R0^{\circ},30^{\circ}$ basis cell. For each simulated image, a schematic of the ribbon is shown as seen edge-on. Fig. 42 a, b, and c depict simulated images of the $[10\bar{1}0]$ "Nb" edge with 2, 1 and 0 terminal sulfur atoms. The simulated image shown in fig. 42b was based on the $(2x\sqrt{3})R0^{\circ},30^{\circ}$ in which the terminal sulfur atom reconstructs to form a bridging atom between two terminal Nb atoms. This simulated image is not consistent with our experimental image data and so we can conclude that it is not representative of the edge termination in our observed image data. For the x = 2 and 0 simulated images in Fig. 42a and c respectively, the best match with experiment is for x = 2. For Fig. 42d and e, showing the $[\bar{1}010]$ "S" edge with 2 and 1 terminal sulfur atoms respectively, indicates a significant dependence on the number of sulfur atoms on the electronic density. It can be seen that Fig. 42e with one terminal sulfur atom that the electron density increases markedly toward the ribbon edge but that the terminal sulfur atom exhibits significantly lower electron density and is not clearly visible. In contrast, Fig. 42d depicting the $[\bar{1}010]$ "S" edge with two terminal sulfur atoms shows a high electron density on sulfur atom at the outermost edge. None of the $[\bar{1}010]$ "S" edge models resemble the experimentally observed STM images as closely as do the $[10\bar{1}0]$ "Nb" edge models with 0 or 2 terminal sulfur atoms. Thus, our data indicates that the observed edges are most likely to be the $[10\bar{1}0]$ "Nb" edge with zero or two terminal sulfur atoms. From our investigation we conclude that the sulfur edges may not be sufficiently stable to be observed under typical ambient STM conditions.

2.2. MoS_2

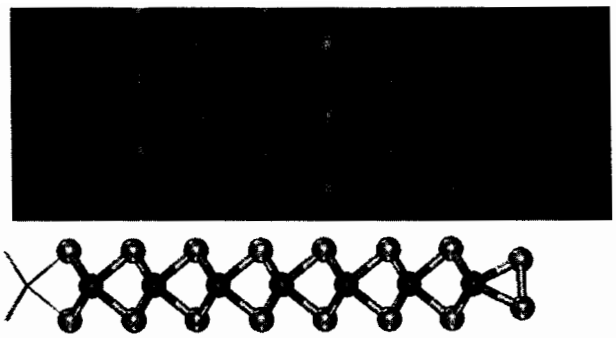

(a)

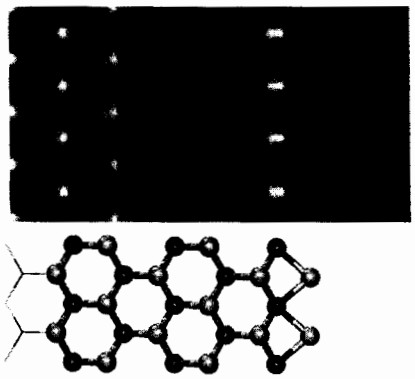

(b)

Fig. 42. Simulated STM images for edge structures for $[10\bar{1}0]$ NbS_x- edge with a), x = 2, b) x = 1, c) x = 0; and for $[\bar{1}010]$ NbS_x- with d) x = 2, and e) x = 1. All simulated images are based ribbon structures constructed from $(1x\sqrt{3})R0°,30°$ basis cells except b) which was constructed from a $(2x\sqrt{3})R0°,30°$ basis cell.

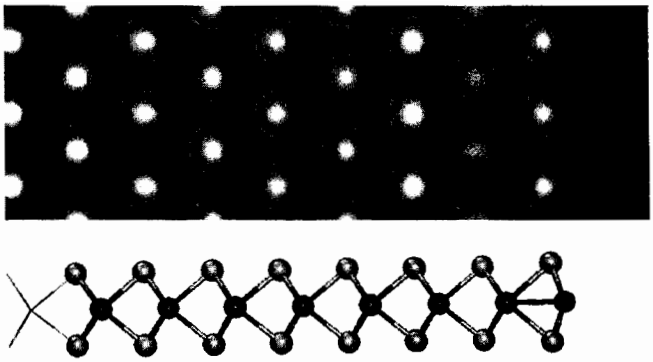

(c)

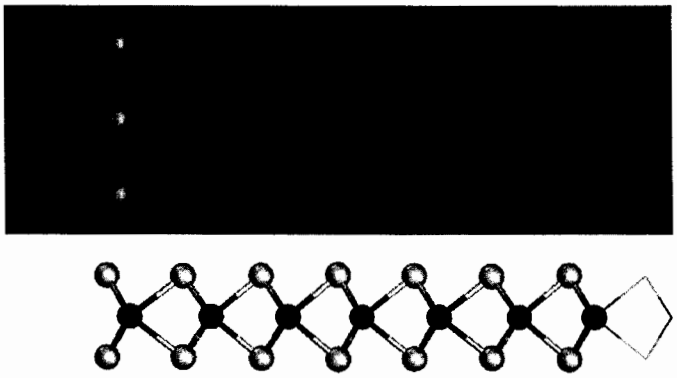

(d)

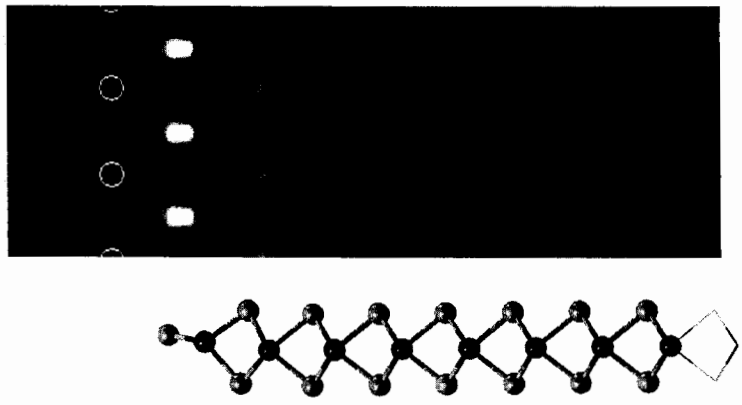

(e)

2.2.1. Optimized Geometries of MoS_2 edges

Structural Properties Edges of MoS_2 were constructed by redefining the hexagonal bulk structure to an orthorhombic 1 x $\sqrt{3}$ structure. This was accomplished by multiplying the bulk lattice vectors $\begin{pmatrix} 1 & 0 & 0 \\ 1 & 2 & 0 \\ 0 & 0 & 1 \end{pmatrix} \cdot \begin{pmatrix} a \\ b \\ c \end{pmatrix}$. The chemical composition of the resulting edges was varied for the "Mo" $[10\bar{1}0]$ and "sulfur" $[\bar{1}010]$ edges. Each edge types with sulfur coverage were optimized and then analyzed.

The "sulfur" $[\bar{1}010]$ edges for NbS_2 were not observed in STM study. Therefore, only the "Mo" $[10\bar{1}0]$ for MoS_2 was studied. Structures for the various MoS_2 edges studied are illustrated in Fig. 21. The sulfur atoms on the 4-fold sulfur saturated Mo $[10\bar{1}0]$ edge tend to displace inward in the basal plane (a,b) dimension by 0.01 Å and toward each other by 0.03 Å in the stacking (c) dimension. Relaxations for sulfur atoms next to and further from the edge-most atoms are comparatively smaller than the edge-most sulfur atoms. Thus, most of the relaxation occurs at the edge-most atoms.

More pronounced relaxations of were observed on 5-fold and 6-fold sulfur saturated metal edges (Fig. 21 b and c). On these edge types, the outermost sulfur atoms relax toward the metal surface with Mo-S bond distance of 2.111 Å. In the case of the 6-fold sulfur saturated metal edge, the sulfur atoms at the outermost edge are dimerized leading to a contraction of the S-Mo distance by 0.115 Å. The displacement of metal atoms in the metal layer is significantly smaller than those of

the sulfur atoms and we conclude that the important relaxations in these systems are those of the edge-most sulfur atoms.

In the case of the [11 $\bar{2}$ 0] terminated edge, only one type of surface termination is found (in contrast to the "Mo" [10$\bar{1}$0] and "sulfur" [$\bar{1}$010] edges above). The optimized edge configurations are shown in Fig. 43. The sulfur atoms on the sulfur -free edge relax outward by 0.05 Å. This expansion causes to displace edge metal atoms inward into the bulk by 0.07 Å. The number of sulfur atoms on the sulfur-free edge reduces the atom displacements. In 5-fold sulfur saturated edge (in Fig. 41b), this sulfur atom shifts to the coplanar position of metal keeping Mo-S bond distance of 2.408 Å compared to 2.405 Å for bulk. By this sulfur atom shift to coplanar, the displacement of edge-most metal is small by 0.03 Å into the bulk. In the case of 6-fold sulfur saturated edge, two sulfur atoms are dimerized with the small relaxation of outmost metal atom. The outmost Mo atom is relaxed by 0.01 Å. The second-most edge metal on three types of terminations is replaced by less than 0.001 Å. The optimized bond distances of S-S atoms are shown in Fig. 41.

2.2.2. Electronic Structure and Image Simulation

The band structures for the "Mo" [10$\bar{1}$0] and "sulfur" [$\bar{1}$010] edges are shown in Fig. 44 a and b. The band structures shown in Fig. 44 are complicated compared to the bulk band structures due to Brillouin Zone folding. The bands between 10 and 10.75 eV represent Mo d-electron crystal orbitals. Below this energy range are found bands derived from metal d orbital and sulfur p orbital mixing. It is interesting that new energy states are distributed in the (bulk) band gap. This results in a significant reduction in the band gap leading to a correspondingly higher conductivity as

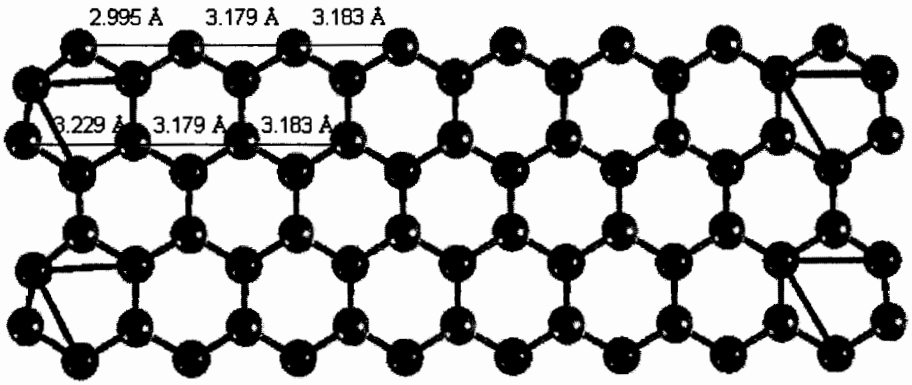

(a)

Fig.43. (a) Optimized structure of 4-fold sulfur staurated $(11\bar{2}0)$ edge.

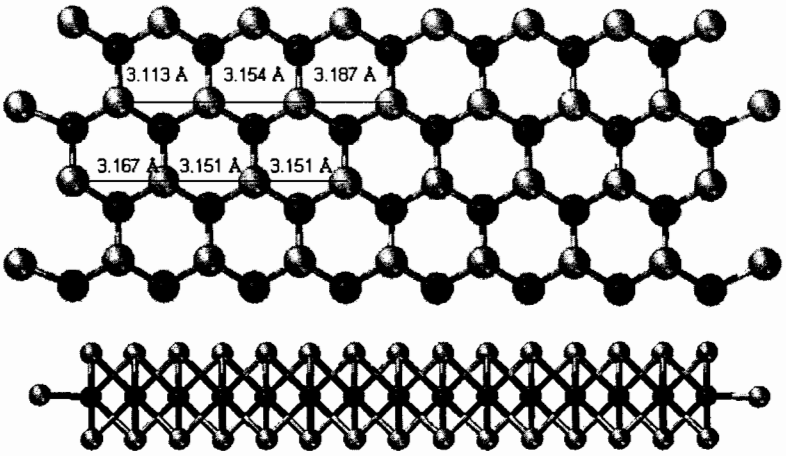

(b)

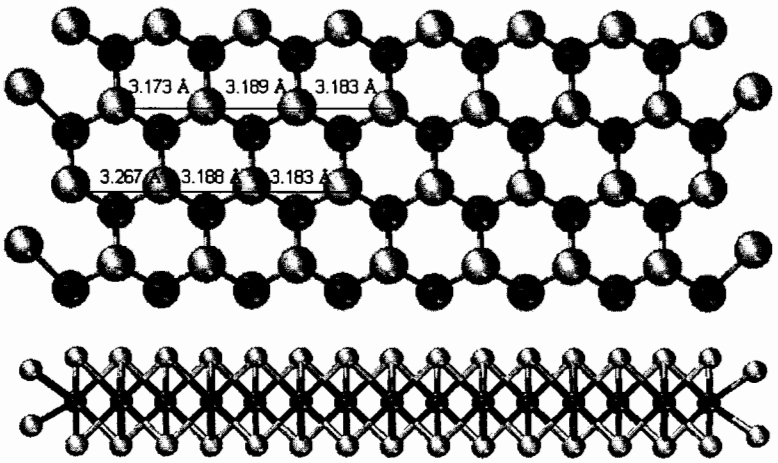

(c)

Fig.43. Optimized structures of (b) 5- and (c)6-fold sulfur staurated $(11\bar{2}0)$ edge. Top view and side views of (b) 5-fold and 6-fold sulfur staurated $(11\bar{2}0)$ edges.

evidenced by the lower bias voltages required for stable STM imaging.

In Fig. 44a, four edge states are labeled as E1, E2, E3, and E4. Two different edges which exist on the ribbon model exhibit distinct edge states. Therefore, it is difficult to distinguish the edge states resulting from the metal and sulfur edges. As an aid in distinguishing these states, we undertook studies in which the sulfur edges were "capped" with hydrogen. In this way bands which indicate changes derived from the addition of hydrogen would signify sulfur edge states The edge states, E1 and E2 shown in Fig. 44 a are redistributed to a lower state in the band gap. In contrast, E3 and E4 local states are not changed, consequently we assign E1 and E2 as sulfur edge states. New local states also appear in the energy region from 10.50 to 11.50 eV for the metal and sulfur edges and are labeled as E5 and E6 for the 'Mo" $[10\bar{1}0]$ and "sulfur" $[\bar{1}010]$ edges, respectively. Fig. 44 b and c represents the "sulfur" $[\bar{1}010]$ edge with 5- fold and 6-fold sulfur saturation. The E3 state has disappeared whereas the E4 state is lowered and crosses the Fermi level. The E1 and E2 states are redistributed in the band gap. However, energy states of bulk are dominant at the Fermi level. These results indicate that the "Mo" $[10\bar{1}0]$ and "sulfur" $[\bar{1}010]$ edge termination, irrespective of the chemical composition, exhibit the highest electron density at the outermost edge and are metallic.

In contrast to the "Mo" $[10\bar{1}0]$ and "sulfur" $[\bar{1}010]$ edges, the MoS_2 $[11\bar{2}0]$ edge band structures exhibit a band gap and so remain semiconducting. Interestingly, the band gap varies as a function of the number of coordinated sulfur atoms on the metal. The band gaps for the sulfur-free edge (corresponding to Fig. 41a) and for the 6-fold sulfur saturated edge (corresponding to Fig. 45c) are 0.15 and

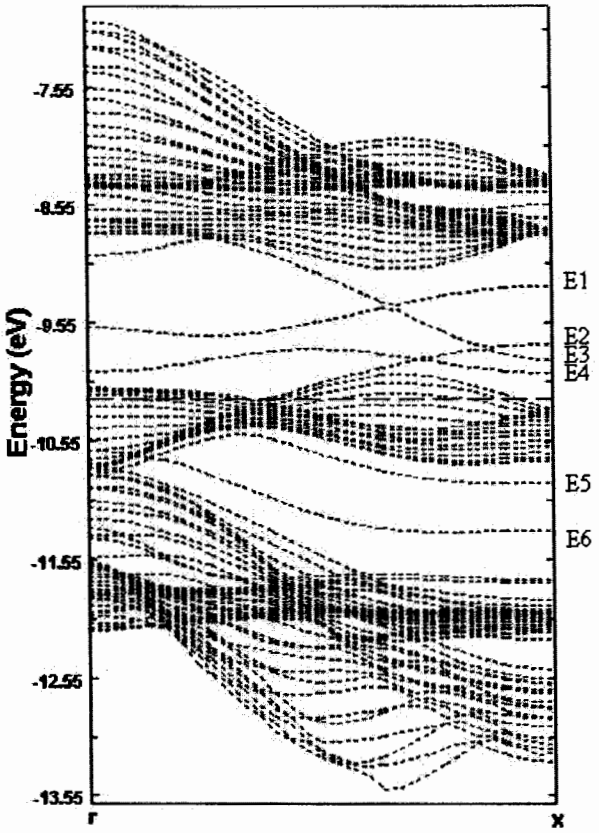

(a)

Fig. 44. (a) Calculated band structure of 4-fold sulfur saturated metal $(10\bar{1}0)$ edges of MoS_2 ribbons.

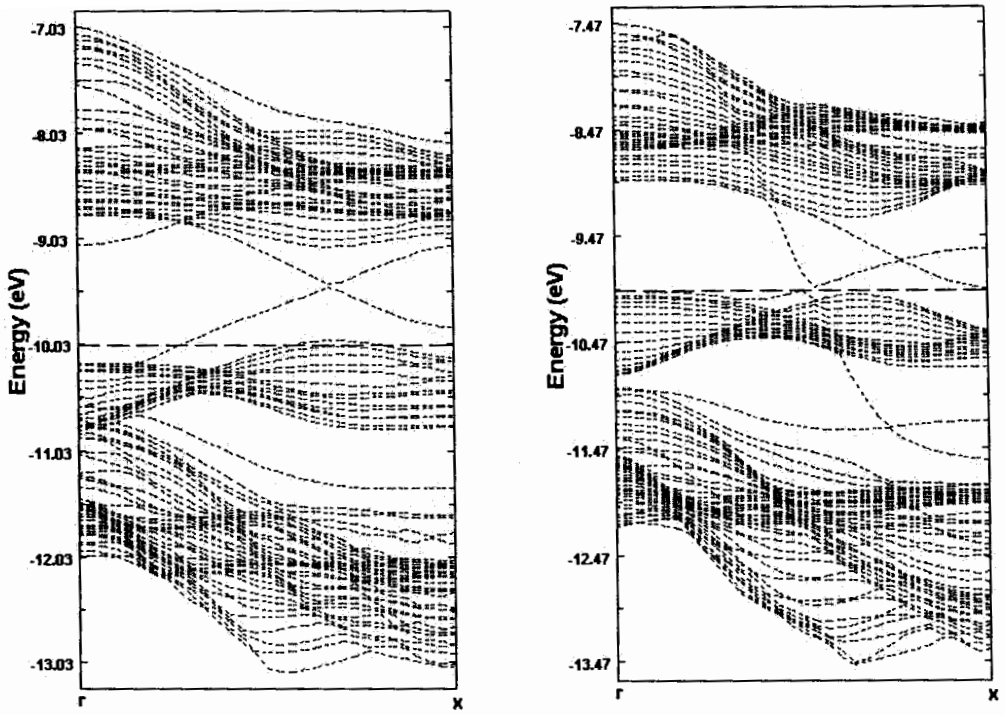

(b) (c)

Fig. 44. Calculated band structures of (b) 5-fold and (C) 6-fold sulfur saturated metal $(10\bar{1}0)$ edges of MoS_2 ribbons.

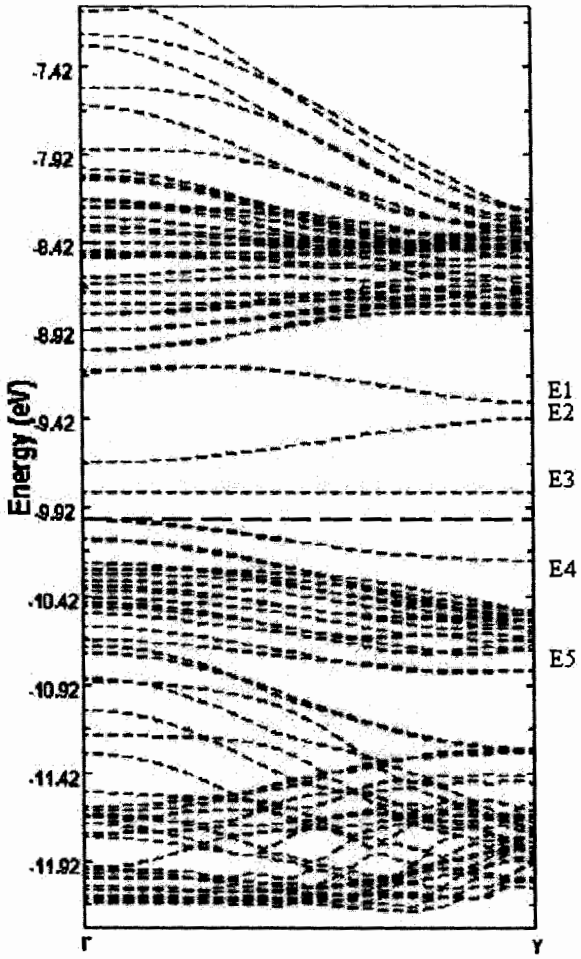

(a)

Fig. 45. Calculated band structure of (a) 4-fold sulfur saturated $(11\bar{2}0)$ edges of MoS_2 ribbons.

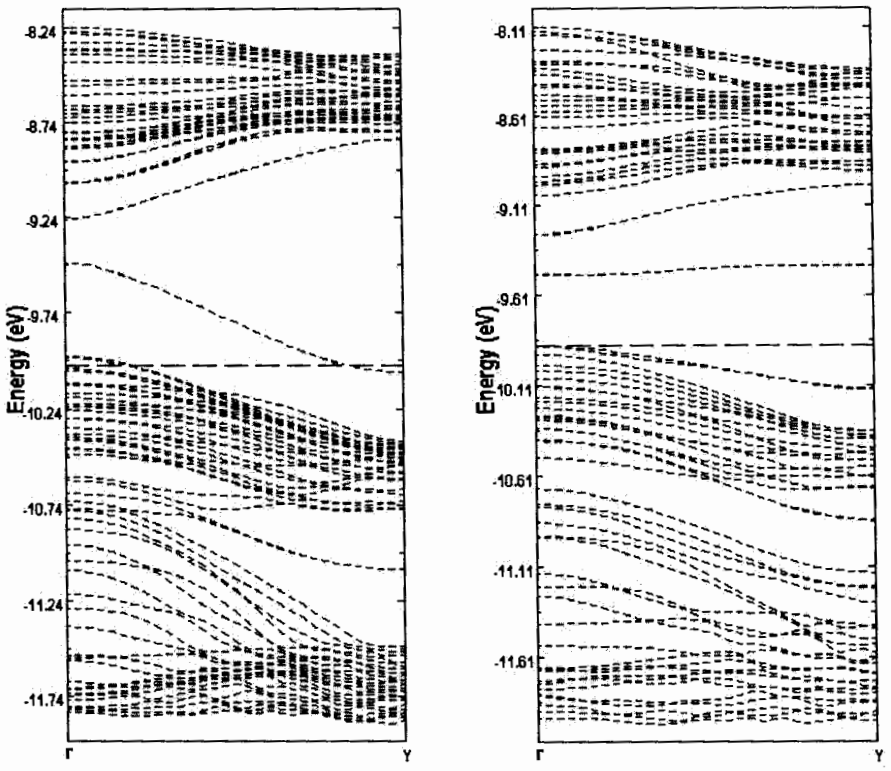

(b) (c)

Fig. 45. Calculated band structures of (b) 5-fold and (c) 6-fold sulfur saturated $(11\bar{2}0)$ edges of MoS_2 ribbons.

0.52 eV, respectively. these are indirect: the top of the valence band occurs at Γ and the bottom of conduction band occurs between Γ and X. Whereas, 5-fold sulfur saturated edge (corresponding to Fig. 45b) does not have the band gap. The local energy state E3 (bottom of conduction band) shows downward dispersion passing through the Fermi energy level.

These new states in the [11$\bar{2}$0] edge might be related to the superstructures in the STM images since these states cross the Fermi level at k-vectors having frequencies similar to those observed experimentally. It is not simple to interpret these new energy states which might be related to supuerstructure since the variation in tunneling current in STM image is dependant on the tip-sample separation (geometry) and topography of the local density of states (LDOS). The closest layer to tip is sulfur layer. Sulfur orbital distributions are small at the Fermi level. This existence of band gap causes the d-states to redistribute sulfur orbitals near the Fermi level. As described below, the metallic LTMCs do not exhibit the superstructure pattern and remain metallic when restructured as truncated edges. Consequently, no new states appear that would lead to a superstructure in metallic LTMCs, consistent with experimental STM result.

The band structures of MoS_2 ribbons show that new Fermi level energy states appear at different k-vector frequencies depending on the types of edges and on the chemical composition. These localized Fermi level energy states may be observed by STM provided that these states have prominent surface projected electron density. It is possible that the observed superstructure patterns observed in the STM experiment are caused by the presence of these new Fermi level states. In order to investigate this possibility we prepared simulated STM images of the MoS_2 ribbon

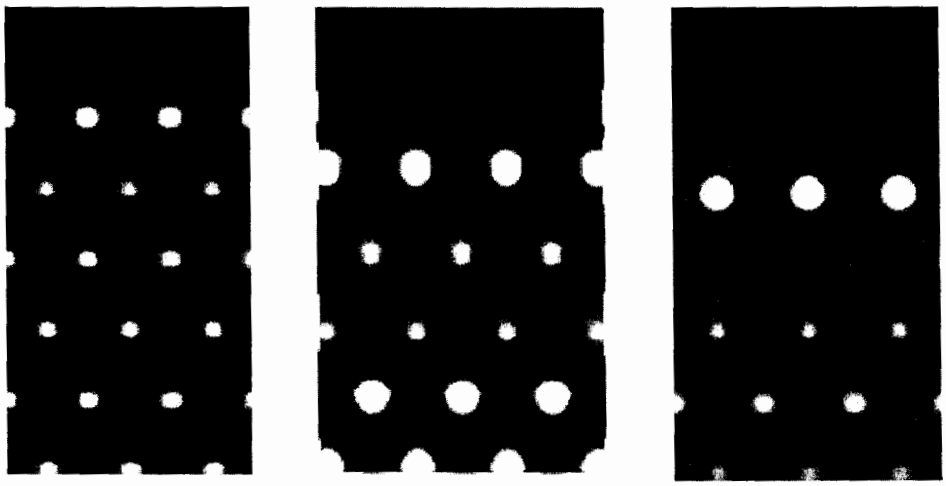

(a) (b) (c)

Fig. 46. Simulated STM images for edge structures for the "Mo" [$10\bar{1}0$] edge: (a) 4-fold, (b) 5-fold, and (C) 6-fold sulfur saturated edges.

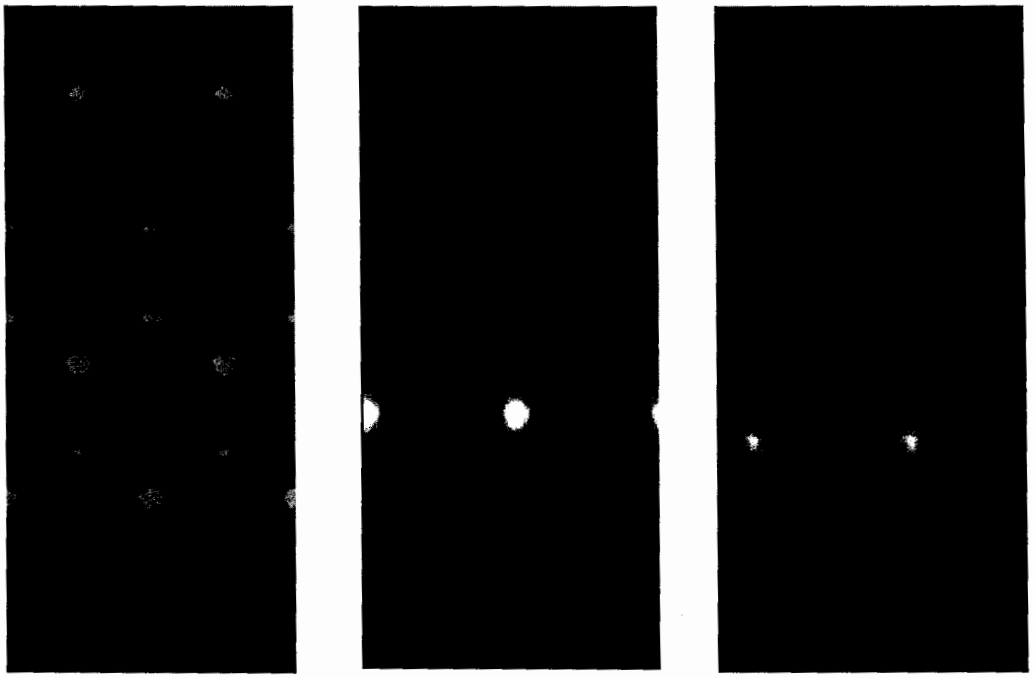

Fig. 47. Simulated STM images for edge structures for the $[11\bar{2}0]$ edge: (a) 4-fold, (b) 5-fold, and 6-fold sulfur saturated edges.

structures.

The calculated STM images of the "Mo" [10$\bar{1}$0] for MoS_2 are similar to the NbS_2. Fig. 46 show simulated STM images for MoS_2 with varying sulfur coverages on the [$\bar{1}$010] and [10$\bar{1}$0] edges. To explore the possibility of reconstruction parallel to the edge, we also investigated ribbon structures based on a 2 x $\sqrt{3}$ unit cell. The sulfur atom on the 5-fold sulfur saturated edge is found to dimerize with an adjacent sulfur atom. This dimerized structure results in a change in the hexagonal periodicity at the edge-most atoms. In contrast, similar dimerizations fior the saturated 6-fold sulfur saturated edge retains the hexagonal periodicity with respect to bulk lattice.

As discussed above, the 4-fold and the 6-fold sulfur terminated [11$\bar{2}$0] edges are semiconducting whereas the 5-fold termination produces metallic character. Fig. 47 b is the PDOS for 5-fold termination. All p-states are distributed near the Fermi level and so would be expected to dominate the STM image data. Based on band structure calculations, mixing of p-states is enhanced for the 4-fold termination. The px and py states are more pronounced than the pz states near the Fermi energy. This suggests that this redistribution of p-states might be related to the formation of the observed superstructures in the STM images of MoS_2.

It is apparent that the origin of superstructure arises from the nature of the edge termination. In particular, the [11$\bar{2}$0] edge appears to be related to the appearance of superstructure. Simulation results indicate that it is structurally unfavorable to have the edge coordination with the 5-fold and 6-fold sulfur saturated edges since the high electron density is localized on the second-most sulfur aoms. In contrast, the 4-fold sulfur saturated edge does not have the localized HED at the edge. From the STM

results the possible edge terminations must have semiconducting characteristic. 4-fold and 6-fold sulfur saturated edge terminations satisfy the semiconductinng characteristic. It suggests that 4-fold sulfur saturated edge termination might be related to the superstructure observed by STM.

3. Simulation Studies of Edge Adsorption

Our experimental and theoretical studies reveal that the most stable edge terminations on MoS_2 are the $[10\bar{1}0]$ and $[11\bar{2}0]$ edges. Based on these findings, the next step is to determine the nature of binding of a sulfur containing molecule on the proposed edge terminations. It is important to characterize the details of active site binding, particularly as pertains to any differences in these two edge types. As an initial investigation into this, we undertook a simulation study for the fully unsaturated metal edges.

These studies involved placing a thiophene molecule near the probe edge and allowing the system to equilibrate to lowest energy. Table IV presents the structural parameters and the corresponding adsorption energies for the systems studied. There are several possible orientations that the starting structure can have typified by the relative bonding arrangement of the thiophene ring relative to the edge metal atom. The η^5 orientation refers to the thiophene ring plane normal being placed perpendicular to and along the edge surface and η^1 with the ring normal parallel to the edge surface. In all cases, the η^5 geometry is significantly more stable than the edge-on η^1 geometry and so only the latter is considered. One of the key aspects to probe in thiophene binding is ring weakening (as indicated by bond length increases) that would lead to ring rupture and subsequent C-S bond dissociation.

From the calculated structural parameters the greatest ring weakening in

thiophene is for the 45° η^5 binding geometry on the $(10\bar{1}0)$ edge shown in Fig. 48a. The bond lengths between S-C_1 and C_2-C_3 are 1.825Å and 1.423Å, compared to 1.729Å and 1.375Å for the unbound thiophene, respectively. In the case of 45° -η^5 geometry on the $(10\bar{1}0)$ edge, the thiophene rotates with respect to the metal atom during the optimization and equilibrates at a position between the sulfur and metal atoms. In all the other cases, the rotation of thiophene is slightly less than that of the 45° η^5 geometry on the $(10\bar{1}0)$ edge. The rotation may also induce greater activation of the S-C_2 bond with a concomitant increase in adsorption energy of 0.261 eV. This absorption energy is higher than that of the parallel η^5 geometry shown in Fig.48b.

The η^5 geometries on $(10\bar{1}0)$ edge is the most stable adsorption geometry and is well explained with the η^5 geometries on the $(11\bar{2}0)$ edge. The calculated adsorption energies of the perpendicular and parallel η^5 geometries on the $(11\bar{2}0)$ edge were 1.186 and 1.001 eV, respectively. The highest destabilization of thiophene on the $(11\bar{2}0)$ edge occurs for parallel η^5 binding geometry shown in Fig. 48c. The bond lengths between S-C_2 and C_3-C_4 are 1.796 and 1.418 Å. These adsorption energies are considerably weaker than that of the η^5 geometry on the $(10\bar{1}0)$ edge. However, these weaker interactions manifest a strong interaction between the thiophene sulfur atom and the metal edge surface sites leading to greater activation of the thiophene C-S bonds.

Compared to unbound thiophene, All η^5 binding geometries lead to significant activation on both the $(10\bar{1}0)$ edge and $(11\bar{2}0)$ edges. This indicates that the HDS reaction may be more active in these adsorption geometries. Clearly, the η^5

geometries on both edge types could lead to HDS pathways with different activation energies. These results could represent significant consequences for subsequent bond dissociation and hydrogenation. In order to formulate a consistent picture of the actual HDS pathway(s), kinetic investigations of several proposed mechanisms would need to be initiated.

Table IV. Geometrical parameters and adsorption energies of the thiophene adsorbed on different edge configurations.

Edge Surface	Orientation of thiophene	Bond Length (Å)			Adsorption Energy (eV)
		S_{thio}-Mo	S-C	C-C	
Experimental			1.714	1.427	
Free thiophene			1.729	1.375	
$(10\bar{1}0)$	parallel η^1	2.361	1.743	1.360	0.871
$(10\bar{1}0)$	perpendicular η^1	2.372	1.743	1.360	0.880
$(10\bar{1}0)$	parallel η^5	2.586	1.825	1.423	2.456
$(10\bar{1}0)$	45 ° η^5	2.502	1.820	1.476	2.717
$(10\bar{1}0)$	perpendicular η^5	2.586	1.769	1.399	1.877
$(11\bar{2}0)$	parallel η^1	2.537	1.753	1.362	0.825
$(11\bar{2}0)$	perpendicular η^1	2.537	1.753	1.362	0.830
$(11\bar{2}0)$	parallel η^5	2.556	1.796	1.418	1.186
$(11\bar{2}0)$	perpendicular η^5	2.560	1.769	1.382	1.001

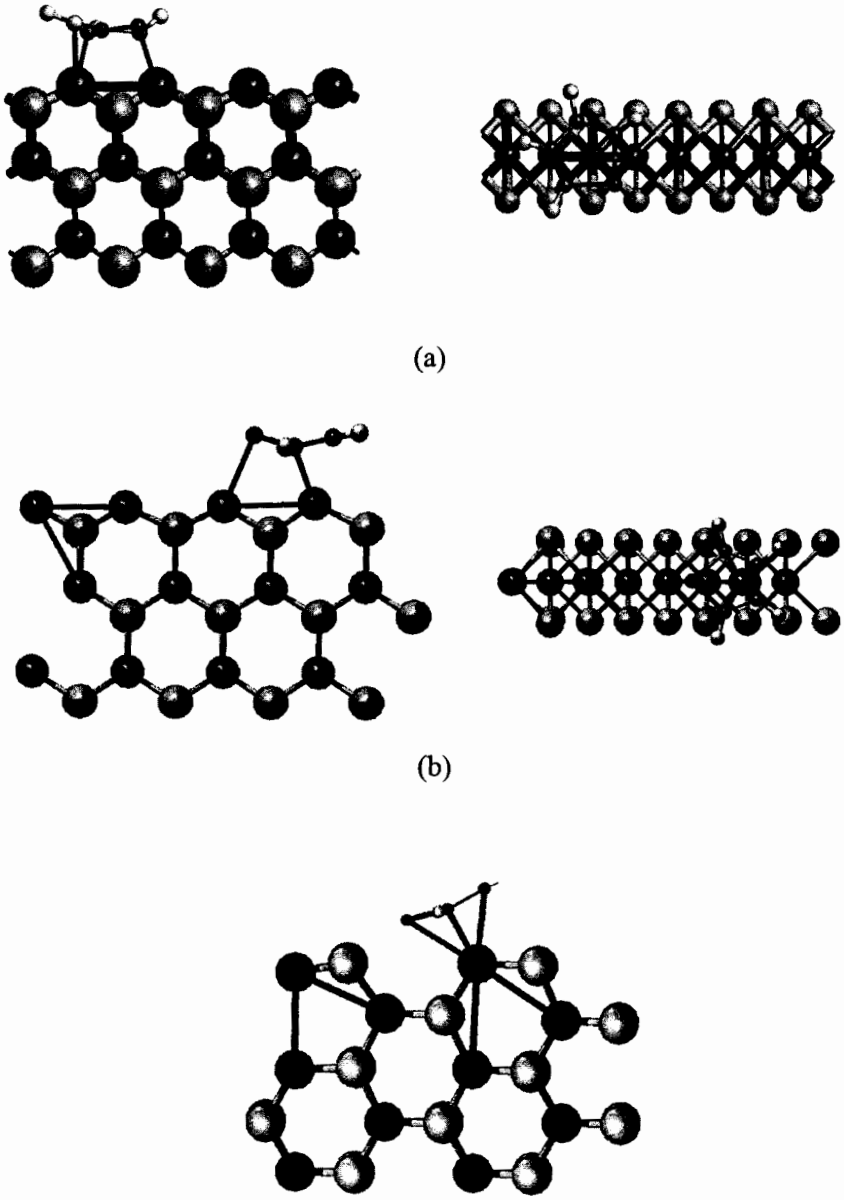

Fig. 48. Most stable adsorption geometries on (a) and (b) the $[10\bar{1}0]$ and (c) $[11\bar{2}0]$ edges.

Conclusions

We have conducted the research in order to clarify unsolved nature edge of LTMCs and to characterize the novel electronic and crystal structure near the edge and at edge.

First, we tried to probe the step edges on the bulk basal plane. In most case, the step edges are randomly distributed on the basal plane and the high variation in the density of states resulting from the edge is high. To obviate these problems, the nanoclusters were prepared since the active surface is increased relative to the step edge. The monolayered nanoclusters on the flat and conductive substrates are suitable for STM measurement. Therefore, HOPG was selected for substrate instead of LTMCs and Au (111). The LTMCs which have the high conductivity resulted in the etching process forming a nucleation and a pit growth. Moreover, the Au substrate had an interface interaction between Au surface and nanocluster; the calculated STM image of MoS_2 depending on the lattice commensuration is similar to the published STM result.

Second, we investigated mostly MoS_2 that only exist in nature and the most stable industrial catalyst and then extended to its iso-structured LTMCs, NbS_2, WS_2, $NbSe_2$ and ReS_2. We observed that the nanoparticles of semiconducting MoS_2, ReS_2, WS_2, and metallic $NbSe_2$ exhibit a superstructure in the near-edge region whereas the metallic $NbSe_2$ show only bulk-like structures. Two types of edge terminations, $(11\bar{2}0)$ and $(10\bar{1}0)$ exist. The $(11\bar{2}0)$ edge termination shows a localized electron density as the $(\sqrt{3} \times \sqrt{3})\ 30^{\circ}$ superstructure and extended 2-3 nm to the bulk lattice. whereas the $(10\bar{1}0)$ edge termination has a localized electron density at the

outermost edge.

Third, the edges were modified by the chemical treatment of alkane thiols. The primary thiols were expected to attach to the edge surface forming a thiolate such as HDS reaction. We assumed that the presence of thiolates quenches the electronic states at edges. However STM images were not obtained since the thiol adsorption does not occur at room temperature. This is a crucial result of the edge termination. This indicated that the only sulfur-coordinated edges exist.

To interpret the material characteristics that are responsible for the image data features, it was crucial to include modeling studies. The electronic and structural properties were interpreted by DF and EHTB methods. The edge structures of MoS_2 and NbS_2 were compared to distinguish the electronic edge structures depending on the types of conductivity. The electron band dispersion calculations revealed that the electronic structures are varied as a function of the different types of LTMCs as well as the number of edge crystal coordinates. For all edge terminations for metallic NbS_2 and $(10\bar{1}0)$ edge termination for MoS_2 the edge states have metallic character. In contrast, for the $(11\bar{2}0)$ edge for MoS_2 the localized edge states are distributed at the Fermi level with the existence of band gap state.

We found that the only $(11\bar{2}0)$ edge for MoS_2 exhibit semiconducting behavior. The electronic structures $(11\bar{2}0)$ edge of as a function of edge coordinates shows a transition of conductivity as a function of number of sulfur coverage at the edge surface. The semiconducting properties are kept only in the case of the 4-fold and 6-fold sulfur saturated edge terminations. The 5-fold edge is metallic behavior. This indicates that the catalytic activity can be controlled by the changing the number

of edge coordinates.

The adsorption geometry of thiophene on edges was studied to interpret the initial HDS reactions. The geometry effects causes the adsorption energy; the $(11\bar{2}0)$ edge which has a steric interference between thiophene molecule and metal atoms at edges has lower adsorption energies than adsorption energies for $(10\bar{1}0)$ edge, but in both edges, the thiophene molecule is activated with a disturbed aromaticity. Calculations for thiophene adsorptions on the observed edge terminations show that the η^5 adsorption geometry is the most stable on the both edges.

References

(1) Pecoraro, T. A.; Chianelli, R. R. *J. Catal.* **1981**, *67*, 430.

(2) Harris, S.; Chianelli, R. R. *J. Catal.* **1984**, *86*, 400.

(3) Topsøe.; Clausen, B. S.; Massoth, F. E. "*Hydrotreating Catalysis-Science and Technology*", Springer, Berlin, **1996**.

(4) Wyckoff, R. W. G. "*Crystal Structures*", Wiley, New York, **1963**, Vol.1.

(5) Topsøe, N. Y.; Topøe, H. *J. Catal.* **1983**, *84*, 386.

(6) Lacroix, M.; Boutarfa, N.; Guillard, C.; Vrinat, M.; Breysse, M. *J. Catal.* **1989**, *120*, 473.

(7) Kelty, S. P.; J.Li; Chen, J. G.; Chianelli, R. R.; Ren, J.; Whangbo, M. H. *J. Phys. Chem. B* **1999**, *103*, 4649.

(8) Tributsch, H.; Jaegermann, W. *Surf. Sci.* **1988**, *29*, 1.

(9) Wilson, J. A.; Yoffe, A. D. *Adv. Phys.* **1969**, *18*, 193.

(10) Jellinek, F. *Nature* **1960**, 10, 376.

(11) Kelty, S. P.; Ruppert, A. F.; Chianelli, R. R.; Ren, J. *J. Am. Chem. Soc.* **1994**, *116*, 7857.

(12) Murray, H. H.; Kelty, S. P.; Chianelli, R. R.; Day, C. S. *Inorg. Chem.* **1994**, *3*, 4418.

(13) Kelty, S. P.; Ruppert, A.F.; Chianelli, R.R.; and Ren, J. *Chem. Ind.* **1996**, *67*, 71.

(14) Marcilly, C. *J. Catal.* **2003**, *216*, 45.

(15) Landau, M. V. *Catalysis Today* **1997**, *36*, 393.

(16) Caldwell, T. E.; Land, D. P. *Polyhedron* **1997**, *16*, 3197.

(17) Qian, W.; Yoda, Y.; Hirai, Y.; Ishihara, A.; Kabe, T. *Appl. Catal. A* **1999**, *184*, 81.

(18) Brenner, J. R.; Marshall, C. L.; Nieman, G. C.; Parks, E. K.; Riley, S. J.; Ellis, L.; Tomczyk, N. A.; Winans, R. E. *J. Catal.* **1997**, *166*, 294.

(19) Eijsbouts; Gestel, J. N. M. v.; Oers, E. M. v.; Prins, R.; Veen, J. A. R. v.; Beer, V. H. J. d. *Appl. Catal. A* **1994**, *119*, 293.

(20) Dunn, J. P.; StengerJr, H. G.; Wachs, I. E. *Catal. Today* **1999**, *53*, 543.

(21) Pasel, J.; Kassner, P.; Montanari, B.; Gazzano, M.; Vaccari, A.; Makowski, W.; Lojewski, T.; Dziembaj, R.; Papp, H. *Appl. Catal. B: Environ* **1998**, *18*, 199.

(22) Voorheoeve, R. I. H. *J. Catal.* **1971**, *23*, 243.

(23) Chianelli, R. R. *Catal. Rev. Sci. Eng.* **1984**, *26*, 361.

(24) Daage, M.; Chianelli, R. R. *J. Catal.* **1994**, *149*, 414.

(25) Raybaud, P.; Kresse, G.; Hafner, J.; Toulhoat, H. *J. Phys.: Condens. Matter* **1997**, *9*, 11107.

(26) Toulhoat, H.; Raybaud, P.; Kasztelan, S.; Kresse, G.; Hafner, J. *Catal. Today.* **1999**, *50*, 629.

(27) Ohdaira, T.; Suzuki, R.; Mikado, T.; Ohgaki, H.; Chiwaki, M.; Yamazaki, T.; Hasegawa, M. *Appl. Surf. Sci.* **1996**, *100-101*, 73.

(28) Brown, N. M. D.; Cui, N.; McKinley, A. *Appl. Surf. Sci.* **1998**, *134*, 11.

(29) Kasztelan, S.; Grimblot, J.; Bonnelle, J. P.; Payen, E.; Toulhoat, H.; Jacquin, Y. *Appl. Catal. B: Environ* **1983**, *13*, 91.

(30) Baker, M. A.; Gilmore, R.; Lenardi, C.; Gissler, W. *Appl. Surf. Sci.* **1999**, *150*, 255.

(31) Belyakova, O. A.; Zubavichus, Y. V.; Neretin, I. S.; Golub, A. S.; Novikov, Y. N.; Mednikov, E. G.; Vargaftik, M. N.; Moiseev, I. I.; Slovokhotov, Y. L. *Journal of Alloys and Compounds* **2004**, *382*, 46.

(32) Wang, H.; Skeldon, P.; Thompson, G. *J. Mater. Sci.* **1996**, *32*, 497.

(33) Rueda, N.; Bacaud, R.; Vrinat, M. *J. Catal.* **1997**, *169*, 404.

(34) Payen, E.; Hubaut, R.; Kasztelan, S.; Poulet, O.; Grimblot, J. *J. Catal.* **1994**, *147*, 123.

(35) Hensen, E. J. M.; Kooyman, P. J.; van der Meer, Y.; van der Kraan, A. M.; de Beer, V. H. J.; van Veen, J. A. R.; Sante, R. A. v. *J. Catal.* **2001**, *199*, 224.

(36) Hoensen, P.; Crozier, E. D.; Alberding, N.; Frindt, R. F. *J. Phys. Chem. B* **1983**, *20*, 4043.

(37) Tang, S. L.; Kasowski, R. V.; Parkinson, B. A. *Phys. Rev. B* **1991**, *39*, 9987.

(38) Park, S.; Quate, C. F. *Appl. Phys. Lett.* **1986**, *48*, 112.

(39) Binnig, G.; Rohrer, H.; Gerber, C.; Weibel, E. *Appl. Phys. Lett.* **1982**,*40*, 178.

(40) Binnig, G.; Rohrer, H.; Gerber, C.; Weibel., E. **1982**, *4*, .57.

(41) Liu, R.; Tonjes, W. C.; Greanya, V. A. *Phys. Rev. B* **2000**, *61*, .5212.

(42) Kikuchi, A.; S, M. T. *Surf. Sci.* **1995**, *326*, 195.

(43) Han, W.; Hunt, E. R.; Pankratov, O.; Frindt, R. F. *Phys. Rev. B* **1994**, *50*, 14746.

(44) Kivuitu, F.; Kelty, S. P. *Mat. Res. Soc. Symp. Proc.* **1997**, *464*, 213.

(45) Benavente, E.; Ana, M. A. S.; Mendiza´bal, F.; Gonza´lez, G. *Coordination Chem. Rev. 224* **2002**, *224*, 87.

(46) Helveg, S.; Lauritsen, J. V; Lægsgaard, E., Stensgaard, I.; Clausen, B. S.; Topsøe, H.; Besenbacher, F. *Phys. Rev. Lett.* **2000**, *84*, 951.

(47) Barth, J. V.; Brune, H.; Ertl, G.; Behm, R. *Phys. Re.v B* **1990**,*42*, 9307.

(48) Topsøe, H.; Clausen, B. S.; Candia, R.; Wivel, C.; Morup, S. *J.Catal.* **1981**, *68*, 433.

(49) Farragher, A. L.; Cossee, P.; Hightower, J. W. In;.North-Holland, Amsterdam.**1973**, 1301.

(50) Chianelli, R. R.; Berhault, G.; Raybaud, P.; Kasztelan, S.; Hafner, J.; Toulhoat, H. *Appl. Catal. A* **2002**, *227*, 83.

(51) Lauritsen, J. V.; Helveg, S.; Laegsgaard, E.; Stensgaard, I.; Clausen, B. S.; Topsøe., H.; Besenbacher, F. *J. Catal.* **2001**, *197*, 1.

(52) Harris, S.; Chianelli, R. R. *J. Catal.* **1986**, *98*, 17.

(53) Raybaud, P.; Hafner, J.; Kresse, G.; Kasztelan, S.; Toulhoat, H. *J. Catal.* **2000**, *190*, 128.

(54) Nara, J.; Higai, S.i.; Morikawa, Y.; Ohno, T. *Appl. Surf. Sci.* **2004**, *237*, 434.

(55) Vericat, C.; Vela, M. E.; Gago, J.; Salvarezza, R. C. *Electrochimica Acta* **2004**. *49*, 3643.

(56) Noh , J.; Ito, E.; Araki, T.; Hara, M.; *Surf. Sci.* **2003**, *532-535*, 1116.

(57) Liu, P.; Rodriguez, J. A.; Muyckerman, J.; Hrbek, J. *Surf. Sci.* **2003**, *530*, L313.

(58) Benning, L. G.; Seward, T. M.. *Geochimica et Cosmochimica Acta* **1996**, *60*, 1849.

(59) Meyer, J. A.; Baikie, I. D.; Kopatzki, E.; Behm, R. J. *Surf. Sci.* **1996**, *365*, L647.

(60) Narasimhan, S.; Vanderbilt, D. *Phys. Rev. Lett.* **1992**, *69*, 1564.

(61) Shiraki, S.; Fujisawa, H.; Nantoh, M.; Kawai, M. *Appl. Surf. Sci.* **2004**, *237*, 284.

(62) Cullen, W. G.; First, N. *Surf. Sci.* **1999**, *420*, 53.

(63) Balasubramanian, K. *Chem. Phys. Lett.* **2002**, *365*, 413.

(64) Emsley, J. "*The Elements*." Oxford.Clarendon.**1990**.

(65) Rodriguez, J. A.; Kuhn, M. *Surf. Sci.* **1995**, *330*, L657.

(66) Rodriguez, J. A.; Dvorak, J.; Jirsal, T.; Hrbek, J. *Surf. Sci.* **2001**, *490*, 315.

(67) Santen, R. A. v.; Neurock, M. *Catal. Rev. Sci. Eng.* **1995**, *37*, 557.

(68) Mitchell, P. C. H.; Green, D. A.; Payen, E.; Tomkinson, J.; Parker, S. F. *Phys. Chem. Chem. Phys.* **1999**, *1*, 3357.

(69) M. Salmeron, G. A. S., A. Wold, R. R. Chianelli and Lang, S.K. *Chem. Phys. Lett* **1983**, *99*, 105.

(70) Startsev, A. N. *Catal. Rev. Sci. Eng.* **1995**, *37*, 353.

(71) Delmon, B.; Froment, G. F. *Catal. Rev. Sci. Eng.* **1996**, *38*, 69.

(72) Wilcoxon, J. P.; Martin, J. E.; Parsapour, F.; Wiedenman, B.; Kelley, D. F. *J. Chem. Phys.*. **1998**, *108*, 9137.

(73) Wilcoxon, J. P.; Newcomer, P. P.; Samara, G. A. *J. Appl. Phys.* **1997**, *81*, 7934.

(74) Wilcoxon, J. P.; Newcomer, P. P.; Samara, G. A. *Advances in Microcrystalline and Nanocrystalline Semiconductors* **1997**, *452*, 371.

(75) Wilcoxon, J. P.; Samara, G. A. *Phys. Rev. B* **1995**, *51*, 7299.

(76) Zonneyville, H. C.; Hoffmann, R.; Harris, S. *Surf. Sci.* **1988**, *199*, 320.

(77) Diez, R. P.; Jubert, A. H. *J. Mol. Catal.* **1993**, *83*, 219.

(78) Raybaud, P.; Hafner, J.; Kresse, G.; Toulhoat, H. *Phys. Rev.Lett.* **1998**, *80*, 1481.

(79) Raybaud, P.; Hafner, J.; Kresse, G.; Toulhoat, H. *J. Phys. (1997)* **1997**, *9*, 11107.

(80) Cristol, S.; Paul, J. F.; Payen, E.; Bougeard, D.; Hafner, J.; Hutschka, F. *Stud. Surf. Sci. Catal.* **1999**, *127*, 327.

(81) Byskov, L. S.; Bollinger, J. K. M.; N.skov; Clausen, B. S.; Topøe., H. *J. Mol. Catal. A: Chemical* **2000**, *163*, 117.

(82) Byskov, L. S.; Hammer, B.; N.skov, J. K.; Clausen, B. S.; Topøe., H. *Catal. Lett.* **1997**, *47*, 177.

(83) Byskov, L. S.; N.skov, J. K.; Clausen, B. S.; Topøe., H. *J. Catal.* **1999**, *187*, 109.

(84) Wang, D.; Qian, W.; Ishihara, A.; Kabe, T. *J. Catal.* **2002**, *209*, 266-270.

(85) Alexiev, V.; Prins, R.; Weber, T. *Phys. Chem. Chem. Phys.* **2001**, *3*, 5326.

(86) Cristol, S.; Paul, J. F.; Payen, E. *J. Phys. Chem. B* **2002**, *106*, 5659.

(87) Spirko, J. A.; Neiman, M. L.; Oelker, A. M.; Klier, K. *Surf. Sci.* **2004**,*572*, 191.

(88) Faye, P.; Payen, E.; Bougeard, D. *J.Mol.Model.* **1999**, *5*, 63.

(89) Paul, J. F.; Payen, E. *J. Phys. Chem. B* **2003**, *107*, 4057.

(90) Orita, H.; Uchida, K.; Itoh, N. *J. Mol. Catal. A: Chemical* **2002**, *195*, 173.

(91) Cristol, S.; Paul, J.-F.; Payen, E.; Bougeard, D.; Hutschka, F.; Clemendot, S. *J. Catal.* **2004**, *224*, 138.

(92) Lobos, S.; Sierraalta, A.; Ruette, F.; Rodriquez-Arias, E. N. *J. Mol. Catal. A: Chemical* **2003**, *192*, 203.

(93) Binnig, G.; Rohrer, H. *Surf. Sci.* **1985**, *152*, 17.

(94) Binnig, G.; Rohrer, H. *Agnew. Chem. Ed. Engl.* **1987**, *26*, 606.

(95) Magonov, S.; Whangbo, M-H. "*Surface Analysis with Scanning Tunneling and Atomic Force Microscopy*", VCH.Weinheim, Germany,**1996**.

(96) Kelty, S. P.; Lu, Z.; Lieber, C. M. *Phys. Rev. B* **1991**, *44*, 4064.

(97) Avouris, P. *J. Phys. Chem.* **1990**, *94*, 2246.

(98) Tersoff, J.; Hamann, D. R. *Phys. Rev. B* **1985**, *31*, 805.

(99) Bloch, F. Z. *Physik* **1928**, *52*, 555.

(100) Hansma, P. K.; Tersoff, J. *J. Appl. Phys.* **1987**, *61*, R1.

(101) Tersoff, J. *Phys. Rev. B* **1989**, *39*, 1052.

(102) Park, S. I.; Quate, C. F. *Rev. Sci. Instrum.* **1987**, *58*, 2010.

(103) Wiesendanger, R. "*Scanning Probe Microscopy and Spectroscopy: Methods and Applications*", Canmbridge Univ. Press, Cambridge **1994**.

(104) Kelty, S. P. "*Electronic and structural studies of intercalated graphite and buckminsterfullereney,* Harvard Univ, Cambridge MA, **1993**, Vol.54.204.

(105) Oliva, A. I.; Aguilar, M.; Sosa, V. *Meas. Sci. Technol.* **1998**, *9*, 383.

(106) Elliott, S. " *The Physics and Chemistry of Solids*", John Wiley & Sons, New York, **1998**.

(107) Kittel, C. "*Introduction to Solid State Physics*", 7th.ed., John Wiley & Sons, New York.**1996**.

(108) Ren, J.; Liang, W.; Whangbo, M. H. " *PrimeColor Software*", Cary, NC **1998**.

(109) Hoffmann, R. *J. Chem. Phys.* **1963**, *39*, 1397.

(110) Canadell, E.; Whangbo, M. W. *Chem. Rev.* **1991**, *91*, 965.

(111) Cox, P. A. "*The electronic structure and chemistry of solids*", Oxford Science Publications, Oxsford, **1987**.

(112) Payne, M. C.; Teter, M. P.; Allan, D. C.; Arias, T. A.; Joannopoulos, J. D. *Rev. Mod. Phys.* **1992**, *64*, 1045.

(113) Milman, V.; Winkler, B.; White, J. A.; Pickard, C. J.; Payne, M. C.; Akhmatskaya, E. V.; Nobes, R. H. *Int. J. Quant. Chem.* **2000**, *77*, 895.

(114) Segall, M. D.; Lindan, P. J. D.; Probert, M. J.; Pickard, C. J.; Hasnip, P. J.; Clark, S. J.; Payne, M. C. *J. Phys.: Cond. Matt.* **2002**, *14*, 2717.

(115) Hohenberg, P.; Kohn, W. *Phys. Rev.* **1964**, *136*, B864.

(116) Kohn, W.; Sham, L. J. *Phys. Rev.* **1965**, *140*, A1133.

(117) Kohn, W.; Sham, L. J. *Phys. Rev.* **1965**, *137*, A1697.

(118) Kohn, W. *J. Chem. Physics.* **2001**, *115*, 3441.

(119) Kohn, W.; Sham, L. J. *Phys. Rev.* **1965**, *140*, 1133.

(120) Perdew, P.; Chevary, J. A.; Vosko, S. H.; Jackson, K. A.; D.J.Pederson; Singh, M. R.; Fiolhais, C. *Phys. Rev. B* **1992**, *46*, 6671.

(121) Perdew, J. P.; Wang, Y. *Phys. Rev. B* **1992**, *45*, 13244.

(122) Perdew, P.; Burke, K.; Ernzerhof, M. *Phys. Rev. Lett.* **1996**, *77*, 3865.

(123) Ma, S.-K.; Brueckner., K. A. *Phys. Rev.* **1968**, *165*, 18.

(124) Kresse, G.; Hafner, J. *J. Phys.: Condensed Matter* **1994**, *6*, 8425.

(125) Vanderbilt, D. *Phys. Rev. B* **1990**, *41*, 7892.

(126) Fletcher, R. *Comp. J.* **1970**, *13*, 317.

(127) Delley, B. *J. Chem. Phys.* **1990**, *92*, 508.

(128) Delley, B. *J. Phys. Chem.* **1996**, *100*, 6107.

(129) Accelrys; http://www.accelrys.com.

(130) Ashokkumar, M.; Grieser, F. *Rev. Chem. Eng.* **1999**, *15*, 41.

(131) Peterson, M. W.; Nenadovic, M. T.; Rajh, T.; Herak, R.; Micic, O. I.; Goral, J. P.; Nozik, A. J. *J. Phys. Chem.* **1988**, *92*, 1400.

(132) Gutierrez, M.; Henglein, A. *J. Phys. Chem.* **1988**, *92*, 2978.

(133) Gutierrez, M.; Henglein, A. *Ultrasonics* **1989**, *27*, 259.

(134) Wilson, T. E.; Murray, M. N.; Ogletree, D. F.; Bednarski, M. D.; Cantor, C. R.; Salmeron, M. B. *J. Vac. Sci. Technol. B* **1991**.

(135) Roberts, C. J.; Wilkins, M. J.; Davies, M. C.; Jackson, D. E.; Tendler, S. J. B. *Surf. Sci.* **1992**, *261*, L29.

(136) Atamny, F.; Kollmann, H.; Bartl, H.; Schoegl, R. *Ultramicroscopy* **1993**, *48*, 1.

(137) Zhang, D. K.; Li, T.; Cotterill, G. F.; Oconnor, D. J.; Wall, T. F. *Fuel* **1993**, *72*, 1454.

(138) Kenny, D. J.; Parmer, R. E. *Surf. Sci.* **2000**, *447*, 126.

(139) Baro, A. M.; Miranda, R.; Alaman, J.; Garcia, N.; Binnig, G.; Rohrer, H.; Gerber, C.; Carrascosa, J. L. *Nature* **1985**, *315*, 253-254.

(140) Scheier, P.; Marsen, B.; M.Lonfat; Schneider, W.; Sattler, K. *Surf. Sci.* **2000**, *458*, 113.

(141) Atamny, F.; Baiker, A. *Appl. Catal. A* **1998**, *173*, 201.

(142) Henglein, A.; Herburger, D.; Gutierrez, M. *J. Phys. Chem.* **1992**, *96*, 1126.

(143) Giunta, P. L.; Kelty, S. P. *J. Chem. Phys.* **2001**, *114*, 1807.

(144) Kivuitu, F.; Kelty, S. P. *Mat. Res. Soc. Symp. Proc.* **1997**, *464*, 213.

(145) Kelty, S. P.; Ruppert, A. F.; Chianelli., R. R.; Ren, J.; Whangbo, M. H. *J. Am. Chem. Soc.* **1994**, *116*, 7857.

(146) Kelty, S.; Ruppert, A. F.; Chianelli, R. R.; Ren, J.; Whangbo, M. H. *Mater. Res. Soc. Symp. Proc.* **1994**.

(147) Remskar, M.; Prodan, A.; Marinkovic, V. *Surf. Sci.* **1993**. 287-288, pt, A, 409- 13.

(148) Dai, H.; Lieber, C. M. *Phys. Rev. Lett.* **1992**, 69, 1576.

(149) Coleman, R. V.; Drake, B.; Giambattista, A.; Johnson, B.; Hansma, P. K.; McNairy, W. W.; Slough, G. *Physica Scripta*. **1988**, 38, 235.

(150) Park, S.-I.; Quate, C. F. *Appl. Phys. Lett.* **1986**, *48*, 112.

(151) Tersoff, J. *Phys. Rev. Lett.* **1986**, *57*, 440.

(152) Chang, H.; Bard, A. J. *J. Am. Chem. Soc.* **1990**, *112*, 4598.

(153) Arnault, J. C.; Bubwendoff, J. L.; Pimpinelli, A.; Bucher, J. P. *Surf. Sci.* **1996**, *348*, 185.

(154) Parkinson, B. *J. Am. Chem. Soc.* **1990**, *112*, 7498.

(155) Delawski, E.; Parkinson, B. *J. Am. Chem Soc.* **1992**, *114*, 1661.

(156) Rapoport, L.; Billik, Y.; Feldman, Y.; Homyonfer, M.; S.R.Cohen; Tenne, R. *Nature* **1997**, *387*, 791.

(157) Kobayashi, K. *Phys. Rev. B* **1996**, *53*, 11091.

(158) Kobayashi, K. *Phys. Rev. B* **1994**, *50*, 4749.

(159) Whangbo, M. H.; Liang, W.; Ren, J.; Magonov, S. N.; Wawkuschewski, A. *J. Phys. Chem.* **1994**, *98*, 7602.

(160) Ness, H.; Fisher, A.J. *Phys. Rev. B.* **1997**, 55, 12469.